A multi-technique approach to study the microstructural properties of tin-based transparent conductive oxides

Thèse N° 9536

Federica LANDUCCI

2019

ÉCOLE POLYTECHNIQUE
FÉDÉRALE DE LAUSANNE

Abstract

Transparent conductive oxides (TCOs) are semiconductor-like materials that exhibit high electrical conductivity and high optical transparency combined. They are adopted in various applications ranging from gas sensors, to electrochromic windows or photovoltaic cells. Indium-based TCOs represent the industry standard. Nevertheless, indium is among the less abundant elements in the earth crust and forecasts based on its current consumption recommend an urgent need to replace it. Tin-based TCOs are a promising alternative, since their opto-electronic characteristics mimic the ones of indium-based materials. This thesis aims to investigate the link between opto-electronic and microstructural properties of tin dioxide and zinc tin oxide (ZTO) with a composition $Zn_{0.05}Sn_{0.30}O_{0.65}$ and their stability when submitted to thermal treatments. Indeed, lots of practical applications require the TCO to operate in high temperature conditions. To conduct this study, a combination of analytical techniques, such as transmission electron microscopy (TEM), energy dispersive X-ray spectroscopy (EDX), X-ray diffraction (XRD), electron paramagnetic resonance (EPR) and differential scanning calorimetry (DSC), as well as optoelectronic measurements were employed. Amorphous SnO_2 and ZTO were deposited by RF sputtering and annealed up to 1050 °C in different atmospheres. The influence of annealing temperature and atmosphere were decoupled and led us to an in-depth comprehension of the mechanisms governing the opto-electronic properties of both materials. When annealed in air, between room temperature and 300 °C, ZTO exhibits increased mobility and carrier concentration with respect to the as-deposited state. This increase, investigated with DSC, was ascribed to a structural relaxation that allows point defects to release electrons in conduction band. Between 300 °C and 500 °C atmospheric oxygen passivates oxygen vacancies, drastically decreasing the carrier concentration and therefore causing a large drop of the conductivity. EPR experiments allowed to ascribe the drop in conductivity to the decrease of

carrier concentration, which occurs slightly before the phase change. At $570\,°C$ (and $930\,°C$ for the case of vacuum annealing) the phase change occurs and the ZTO crystallizes in the rutile form of SnO_2 as proven by XRD and TEM. The material becomes completely insulating. When the temperature is increased to $1050\,°C$, evaporation of zinc is observed. In applications such as gas sensors, which have to work under hostile conditions (corrosive environments as well as during fire) or used as a recombination layer for mesoscopic perovskite/silicon monolithic tandem solar cells, TCOs are required to operate in and resist to high temperatures. In order to improve the electrical conductivity of ZTO at high temperature, a doping strategy was implemented starting from DFT calculations conducted by a partner group, who screened among the entire periodic table, which elements are the best candidates to act as n-dopants for ZTO. Bromine and iodine were retained, since they were found to be the most energetically favorable to become substitutional defects for a tin site. An exploratory doping route is therefore presented and the treated samples analyzed with TEM, EDX, UV-VIS-IR spectroscopy and Hall effect. Finally, the structural properties of an indium-based TCO (zirconium-doped indium oxide) were investigated and used as a benchmark to propose a crystallization model for the tin-based, as well as the indium-based materials. The influence of parameters such as the material thickness, annealing atmosphere and temperature and deposition pressure are discussed for both materials.

Riassunto

Gli ossidi trasparenti e conduttori (OTC) sono dei materiali che esibiscono un comportamento di tipo semiconduttore che devono possedere, contemporaneamente, alta conducibilitá elettrica e alta trasparenza alla radiazione elettromagnetica. Il loro principale utilizzo trova applicazione nei sensori di gas, nelle finestre elettrocromiche cosí come nelle celle fotovoltaiche. Gli OCT aventi come elemento base l'indio rappresentano lo standard industriale. Ciononostante, l'indio é compreso tra gli elementi meno abbondanti nella crosta terrestre e le previsioni basate sull'attual utilizzo di questo elemento suggeriscono un urgente bisogno di rimpiazzarlo. Gli OCT basati sull'utilizzo dello stagno rappresentano una valida alternativa, considerato che le loro proprietà ottiche ed elettriche sono simili a quelle esibite dai materiali a base di indio. Questa tesi ha come obiettivo quello di investigare sul legame tra le proprietà ottiche ed elettriche di questi materiali e quelle microstrutturali, basando gli esperimenti sull'ossido di zinco stagno (ZTO), la cui composizione chimica é $Zn_{0.05}Sn_{0.30}O_{0.65}$. Queste analisi vengono fatte quando il materiale viene sottoposto a trattamenti termici ad alta temperatura. Infatti, molte applicazioni tecniche richiedono che questi OCT sopportino il funzionamento in condizioni di alta temperatura, pur conservando le buone proprietà elettriche e ottiche. Per condurre questo studio, é stata usata una combinazione di differenti tecniche analitiche come la microscopia elettronica a trasmissione (TEM), la spettroscopia EDX, la diffrazione di raggi X, la risonanza paramagnetica elettronica (EPR) e la scansione differenziale calorimetrica (DSC). Fasi amorfe di SnO_2 e ZTO sono state depositate tramite polverizzazione catodica e ricotte fino a 1050 °C in varie atmosfere. L'influenza della temperatura e atmosfera di ricottura sulla microstruttura e sulle proprietà elettriche vengono separate, portando ad una profonda comprensione approfondita dei meccanismi che governano le proprietà di entrambi i materiali. Quando viene sottoposto a trattamenti termici fino a temperature di 300 °C, il ZTO esibisce

una crescita della mobilità e anche della concentrazione di portatori rispetto ai campioni non ricotti. Questo aumento, studiato con la DSC viene associato ad un rilassamento della struttura che permette ai difetti della stessa di rilasciare elettroni in banda di conduzione. Tra i $300\,°C$ e i $500\,°C$, l'ossigeno contenuto in atmosfera passiva le vacanze di ossigeno della struttura, generando una drastica diminuzione della concentrazione di portatori e quindi della conducibilità. Esperimenti EPR hanno confermato che questa diminuzione di portatori è effettivamente la causa della diminuzione di conducibilità, che avviene appena prima del cambiamento di fase. A $570\,°C$ (e $930\,°C$ nel caso di trattamento termico nel vuoto) avviene il cambiamento di fase e il ZTO cristallizza nella forma cristallina del SnO_2 rutilo (tetragonale). Il materiale diventa quindi completamente isolante. Quando la temperature raggiunge i $1050\,°C$, lo zinco é quasi completamente evaporato dal campione. In applicazioni tecnologiche come i sensori di gas o le celle perovskite/silicio monolitico, gli OCT devono essere in grado di sopportare ed operare ad alte temperature di funionamento. Con l'obiettivo di migliorare le proprietà elettriche del ZTO ad alta temperatura, una strategia di drogaggio è esplorata, partendo dalle simulazioni teoriche DFT condotte da un gruppo partner, il quale, dopo aver vagliato l'intera tavola periodica, ha concluso che il bromo e lo iodio sono i due elementi energeticamente piu favorevoli per agire come droganti di tipo n quando sostituiscono un atomo di stagno nel reticolo del ZTO. I risultati del drogaggio dei campioni ZTO sono analizzati tramite TEM, XRD e spettroscopia UV-VIS-IR. Infine, le proprietà strutturali di un OCT a base di indio (ossido di indio drogato con zirconio) sono state investigate ed usate come riferimento per proporre un modello di cristallizzazione per gli OCT a base di stagno e indio. In particolare, l'influenza di parametri come lo spessore del materiale, la temperatura e atmosfera durante i trattamenti termici e la pressione di deposizione vengono discussi rispetto alle proprietà strutturali di entrambi i materiali.

Résumé

Les oxydes transparents et conducteurs (TCOs) sont des matériaux appartenant à la classe des semiconducteurs et qui possèdent à la fois une conductivité électrique élevée et une haute transparence optique. Ils sont utilisés pour différentes applications telles que capteurs de gaz, fenêtres électrochromiques ou cellules photovoltaïques. Actuellement, le standard industriel utilise les TCOs à base d'indium. Néanmoins l'indium fait partie des éléments plus rares dans la croûte terrestre et les prévisions concernant son utilisation montrent le besoin de le remplacer par un élément plus abondant. Les TCOs à base d'étain sont une alternative prometteuse, car leur propriétés opto-éléctroniques sont similaires à celles des TCOs à base d'indium. En particulier, l'oxyde d'étain dopé au zinc (ZTO) est un bon candidat. L'objectif de cette thèse est d'étudier le lien entre les propriétés opto-éléctroniques et la micro-structure de l'oxyde d'étain SnO_2 et du ZTO, ce dernier ayant une composition $Zn_{0.05}Sn_{0.30}O_{0.65}$, ainsi que leur stabilité quand ils sont soumis à des traitement haute température. En effet, plusieurs applications techniques exigent que le TCO puisse résister et fonctionner à des températures supérieures à 400 °C. Pour mener à bien cette étude, une combinaison de différentes techniques d'analyses telles que la microscopie électronique à transmission (TEM), l'analyse dispersive en énergie (EDX), la diffraction des rayons X (XRD), la résonance paramagnetique des électrons (EPR) et la calorimétrie différentielle (DSC), ainsi que des mesures opto-électroniques classiques, ont été utilisées. Les film minces de SnO_2 et ZTO amorphes ont été déposés par pulvérisation cathodique et chauffés jusqu'à 1050 °C sous différentes atmosphères. L'influence de la température de chauffage et de l'atmosphère ont été découplées et cette information nous a permis de comprendre les mécanismes qui gouvernent les propriétés opto-électroniques des deux matériaux. Lors d'un recuit sous air, entre la température ambiante et 300 °C, le ZTO montre une croissance de sa mobilité et de la concentration des porteurs de

charge par rapport à l'état initial. Cette augmentation, étudiée par DSC, a été attribuée à une relaxation de la structure amorphe qui permet aux défauts du matériau de relâcher des électrons dans la bande de conduction. Entre 300 °C et 500 °C l'oxygène de l'atmosphère passive les lacunes d'oxygène et diminue ainsi la concentration de porteurs de charge, ce qui a pour conséquence une perte de conductivité électrique. Les expériences EPR ont permis d'associer la chute de conductivité à la décroissance de la concentration de porteurs. A 570 °C (et 930 °C dans le cas du chauffage sous vide) survient un changement de phase et le ZTO cristallise sous la forme rutile du SnO_2, comme vérifié par XRD et TEM. Le matériau devient alors complètement isolant. Lorsque la température augmente jusqu'à 1050 °C, une évaporation du zinc est également observée. Pour des applications comme le capteur de gaz ou les contacts passivants (HTPC), cette stabilité du TCO à haute température est particulièrement importante. Avec l'objectif d'améliorer les propriétés électriques du ZTO à haute température, une stratégie de dopage a été mise en place à partir de simulations théorique conduites par un groupe partenaire, qui a exploré tout le tableau périodique des éléments dans le but de trouver les éléments énergétiquement plus favorables comme candidats de dopage de type n pour le ZTO. Le brome et le iode ont été retenus en tant que dopants en substitutions d'un atome d'étain dans la structure du ZTO. Une méthode exploratoire de dopage a donc été testée et les échantillons analysés par TEM, EDX, spectroscopie UV-VIS-IR et effet Hall. Enfin, les propriétés de la structure d'un TCO à base d'indium (oxyde d'indium dopé au zirconium) ont été étudiés et utilisées comme comparaison pour proposer un modèle de cristallisation pour les TCOs à base d'étain et d'indium. L'influence des paramètres comme l'épaisseur du matériau, l'atmosphère, la température de chauffage et la pression de déposition sont discutés pour les deux types de matériaux.

Acknowledgement

Someone once said that we stand on the shoulders of giants that came before us and indeed no other sentence could better picture a summary of this work. If it wasn't for all the people around me, none of this would have been possible. I want to start my acknowledgment by thanking my two supervisors, Dr. Aïcha Hessler-Wyser and Prof. Cécile Hébert, who not only gave me unconditional scientific support but also and even more important they contributed greatly to my human development, always pushing me further and giving me the tools to overcome so many obstacles. This journey transformed me in a better version of myself and I want to thank you for always being by my side. I couldn't have ask for better mentors. In particular, thank you Aïcha for the countless advises, for always being there when I needed it and because I learned so much from you.

I also want to thank all the members that took part of the scientific jury for my final exam, that read this manuscript and took the time to improve its final version: Prof. Frank Nüesch, Prof. Julia Medvedeva, Dr. Sonya Calnan and Prof. Frédéric Courbin for chairing the committee of the examination.

A big thank you to the DisCo Project team, in particular Monica for being a great team leader, Esteban for sharing with me this journey, Miglė for the great efforts in explaining us the details of theoretical simulations and most importantly to Quentin for the countless discussions, for the invaluable scientific support, for the help with the data analysis, the microscopes and so many more, your way of working inspired me so much. A big thanks also goes to the institution that financed the project, the Swiss National Science Foundation (SNF).

To the CIME people, you have been my family this past four years, thank you Marco for always being there when I needed any explanation on random subjects...even if we know that we have 30 seconds to talk to you before your iPhone rings. Davide, Tom and Duncan, I cannot even count the amount of times you saved me at the microscope, gave me fundamental advises, corrected my grammar/pronunciation, provided me with crucial scientific facts and just gave me feedbacks, I grew up a lot thanks to you. A big thank you to my colleagues, Emad, Teresa, Brian, Farhang, Kaushik, Barbora, Stéphane, Lucie, Hui, Gulnaz, Ezra, we had so much fun together, you shared with me all the highs and lows of this journey, the sorties, fondues, barbecues, apéro, pizza (there is a current theme here...) and you really became part of my family. A special thank goes to Davide (also known as Dave) because I don't even need to talk with you, you just understand me, thank you for always be there for me, for no matter what. Thanks to Danièle and Colette, you are the master of sample preparation and of finding solutions when I couldn't even see the light. Thank you Fabienne for the best training I have ever received and thank you Greg for the overall help with IT related stuff.

Thanks to Prof. Ballif for always asking for nothing but the best and for organizing so many short talks that made me present properly in public. Thank you to my PVlab colleagues, Ele, Ana, Josua, Gizem....you are way too many to be listed here but I want to thank Florent in particular for the back and forth between Lausanne and Neuchâtel with TEM samples and Jean for all the fancy teas enjoyed together and for helping me out with several lateX bugs.

Ai miei amici e amiche più cari, siete lontani dagli occhi ma vicini al cuore, tornare a casa é ogni volta una gioia anche grazie a voi. A mia mamma e mio papà, non ci sono parole giuste per esprimervi la mia profonda gratitudine, ammirazione e amore, siete il mio porto sicuro quando fuori il mare é in tempesta, niente di tutto quello che ho fatto e in cui sono riuscita sarebbe mai stato possibile senza la vostra presenza, che fortuna enorme avervi con me! A Robi, compagna costante di avventura, grazie per esserci stata giorno per giorno in questo viaggio perché é come se non ci fosse alcuna distanza geografica tra di noi. Grazie a Mimmi e zio Anto, per le chiacchierate come per le vacanze in barca. Grazie Giada per i mille FaceTime a tre, in orari improponibili ma che mi hanno sempre alleggerito e rallegrato le giornate. E infine, ma non di certo per importanza, grazie ad Anto, compagno di strada, di squadra e di vita, grazie per il supporto passato e presente, se non fossi stato al mio fianco fin dal principio, questa esperienza sarebbe andata molto diversamente. La vita con te é enormemente più bella. Questo lavoro di tesi é dedicato a te.

+

Contents

CHAPTER 1

Introduction

A transparent conductive oxide (TCO) is a material that possesses simultaneously high optical transparency and high electrical conductivity. However, these two properties are antagonist in a way that if the former increases, the latter decreases. Indeed, materials that are usually highly conductive, tend to have dark colors and metallic appearance, whereas transparent materials, such as glass, do not have high electrical conductivity, but are rather insulating. TCOs are part of a particularly selected class of materials that show both high transparency in the visible range and high conductivity values. These materials find application in many different fields, from flat panel displays to electroluminescent devices, from flexible electronics to solar cells and thin film transistors, from energy efficient windows to gas sensors (Figure A.8) [1] [2] [3] [4] [5] [6] [7]. TCOs are generally employed as active materials in devices that need to let light enter in or exit from a device and to extract electric charges so that they can be collected. As an example, TCOs are used as front electrodes in heterojunction solar cells and perovskite-on-silicon tandem solar cells. When they are employed as front electrodes, due to their high optical transparency, they allow the photons into the active parts of the cell, where the photogenerated charges are created and then are able to transport the latter to the outside terminals. TCOs are constituted by one or more metallic elements linked to oxygen atoms. Optoelectronic properties of TCOs vary in a large range and the specific application depends on them. Nevertheless, their electrical conductivities can be inserted between the ones typical for metals and those of semiconductors. Figure 1.2 summarizes
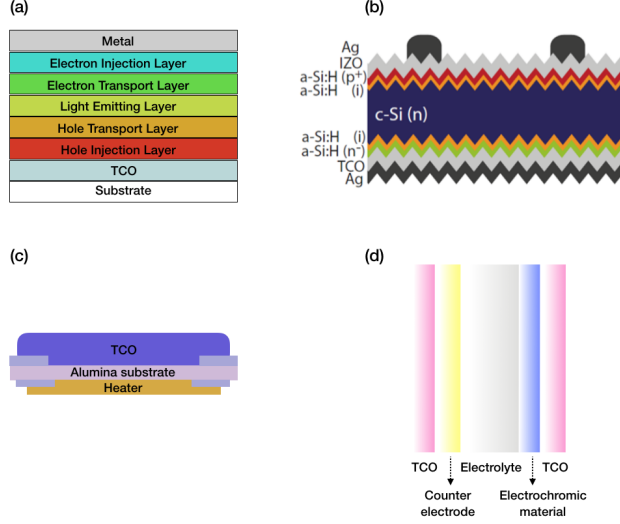
Figure 1.1: Scheme of typical devices fabricated with a TCO. (a) An organic LED, (b) a silicon heterojunction solar cell, (c) a gas sensor and (d) an electrochromic window [8] [9] [10] [11].

the ranges of electrical conductivity for metals, TCOs and semiconductors [12]. More generally, the conductivity of TCOs varies from 1 to 10^4 S cm^{-1}. For what concerns optical transparency, figure 1.3 gives an overview of the typical optical transparencies of different materials.

1.0.1 Optoelectronic properties

The electrical conductivity of a material σ can be expressed as a function of the established electric field $\vec{E}$ as follows:

$$\vec{J} = Ne\vec{v} = Ne\tau\vec{a} = Ne\frac{e\vec{E}}{m}\tau = \frac{Ne^2\tau}{m}\vec{E} = \sigma\vec{E} \tag{1.1}$$

where $\vec{J}$ is the current density, $\vec{v}$ the average speed of electrons between two collisions, $\vec{a}$ the acceleration established because of the presence of an electric field, τ the time between two collisions, N the number of charge carriers, e the electron charge and m its mass. The quantity $\frac{e\tau}{m}\vec{E}$ represents the mobility of an electron in the medium (if m is its effective mass), so that σ (having the dimension of (length)$^{-3}$ (mass)$^{-1}$ (time)^3 (electric-current)^2) can also be expressed as

$$\sigma = Ne\mu. \tag{1.2}$$

Figure 1.2: Overview of electrical conductivities of several semiconductors, TCOs and metals. The conductivity of TCO materials sits in between semiconductors and metals [12].

Figure 1.3: Optical transparency of several materials: metal oxide have transparency which sits in between the one of standard semiconductors and fluorides [12].

From the previous relation it appears clear that in order to increase the conductivity of a material, it is necessary to increase either its carrier concentration N or the mobility μ or both. These two quantities are not equivalent in the c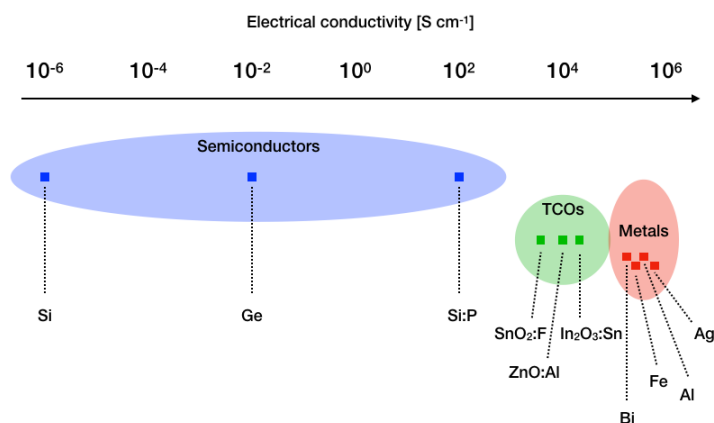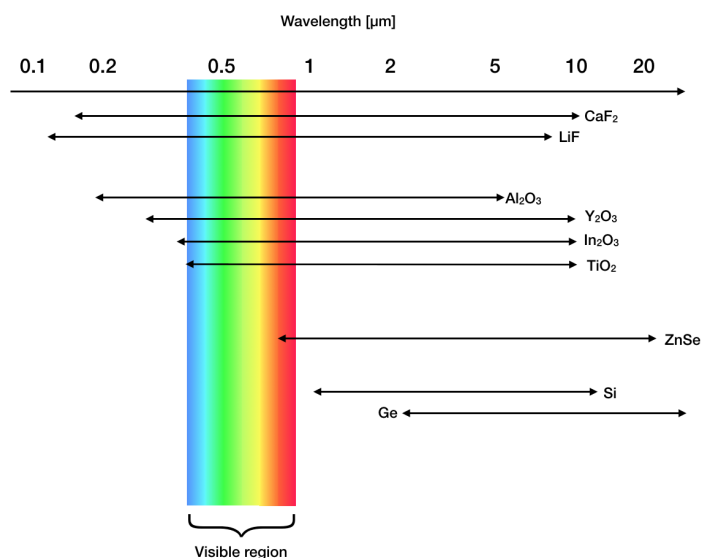ase of a TCO, since, this class of materials has to keep the optical transparency high in an extended optical range. Indeed, the carrier concentration N is related to the plasma frequency as follows

$$\omega_p = \sqrt{\frac{Ne^2}{m^*\epsilon}} \qquad (1.3)$$

The plasma frequency is the typical frequency with which the electron density oscillates in a conducting medium. ω_p is inversely proportional to the effective mass m^* and the medium permittivity ϵ and directly proportional to the carrier density N and the electron charge e. From the Drude-Lorentz model, when the incident radiation frequency is equal to ω_p, the real part of the refractive index $n = \eta + ik$ is zero, therefore the medium becomes highly absorptive and if N increases, ω_p increases accordingly, so that the medium is able to absorb light with higher frequencies and smaller wavelengths. This situation has to be avoided in order to preserve the transparency of the TCO. The typical indium tin oxide (ITO) carrier density is around $10^{21}\,\mathrm{cm}^{-3}$, which leads to a plasma wavelength in the near-infrared region, this means that the material will absorb the light above this wavelength and transmit the one with smaller wavelength. An optimum carrier concentration for a TCO must then be smaller than $10^{21}\,\mathrm{cm}^{-3}$. The lower limit of wavelength of a TCO transmittance is set by the bandgap energy, since photons with an energy higher than E_g are absorbed by the material. The carrier density has, nevertheless, an influence on the small wavelength part of the spectrum too. Indeed, adding carriers in conduction band causes the shift of the bandgap towards higher energies, the so-called Burstein-Moss effect. The consequence of this effect is to widen the optical window of the material in the ultra-violet region of the spectrum.

Generally the metal oxides have a wide bandgap, therefore they are good candidates to be used as TCOs, but in order to obtain a highly conductive material, one should engineer its N and μ. The carrier concentration N can be modified by doping, whereas the mobility μ is an intrinsic property of the material. Indeed, the mobility can be expressed as

$$\mu = \frac{v}{E} = \frac{e\tau}{m^*} \qquad (1.4)$$

where v is the speed of charge carriers under the effect of an electric field $\vec{E}$. The effective mass m^* is related to the curvature of the energy band and can be written as

$$\frac{1}{m^*} = \left(\frac{2\pi}{h}\right)^2 \frac{\partial^2 E}{\partial k^2} \qquad (1.5)$$
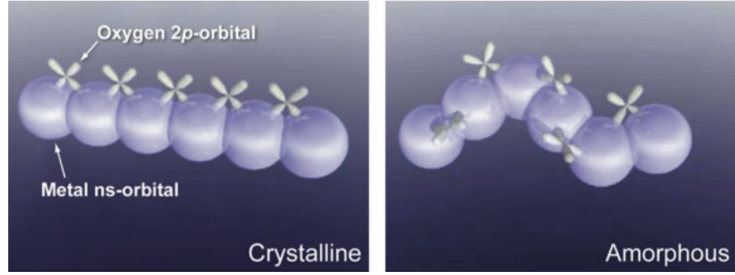
Figure 1.4: Spherical s-orbitals in a crystalline and amorphous arrangement. The structural distortion does not affect the overlap between orbitals since their symmetry is isotropic (sketch from Hosono *et al.* [2]).

where k is the wavenumber and $\partial^2 E/\partial k^2$ represents the curvature of a one-dimensional band. The larger the curvature, the smaller the effective mass of electrons, which leads to a higher electron mobility. TCO materials can be fabricated with different structures, from amorphous to mono and poly-crystalline. Nevertheless, since many TCOs' conduction band is formed by s orbitals, the overlap between these spherical shaped orbitals assures a conduction path for electrons and a high mobility, since the mobility is found to be proportional to the orbital overlap through the formula

$$\mu \propto \frac{\partial^2 E}{\partial k^2} = -2H_{mn}a^2 \tag{1.6}$$

where H_{mn}, the resonant integral value is bigger when the overlap between orbitals is large and a is the distance between two adjacent nuclei [12]. On average, a crystalline material possesses high mobility because the distance between nuclei is minimized and the conduction path is ensured. However, having spherical shaped orbitals grants the TCO a high mobility despite the possible distortion of the structure. Figure 1.4 summarizes this concept. Indeed, for a TCO formed by metal oxides, the conduction band is composed by unoccupied ns^0 orbitals (coming from the metal), whereas the valence band is composed by occupied $2p$ orbitals (originated in the oxygen). This is the reason why the conduction of charged particles is not influenced by the material structure. Since the conduction band, as it is, is an empty band, the TCO behaves as a non-degenerate semiconductor, but when it is doped with enough charge carriers, the bottom of the conduction band starts to be filled and the material behaves as a degenerate semiconductor. In fact, regardless of its structure, doping is fundamental for a metal oxide to be conductive. Stoichiometric materials do not have, in principle, free carriers to give to the conduction band and therefore are not conductive.

TCOs exist in both crystalline and amorphous structures [13], the industry standard is mainly constituted by indium-based TCOs [14] [15] [4] [16] [17], but

alternative and amorphous TCOs are also largely used in several applications. In particular, tin-based TCOs constitute a promising substitute to indium-based ones. Good electrical properties are registered for both amorphous and crystalline materials. A complete overview of their specific properties will be given in the chapter dedicated to the state-of-the-art of these materials.

The transport of charge carriers in TCOs is characterized by its mobility, which is governed by scattering mechanisms that differ from one structure to another and from which depends the mobility of these materials. A charged carrier is able to travel through the energy bands of a TCO until it encounters a collision. These collisions can be originated from different mechanisms and particles. The more relevant scattering mechanisms are the collisions between electrons and impurities, which can be neutral or ionized, together with phonon scattering (lattice vibrations), defect scattering and grain boundaries, etc. [18] [19] [20] [21]. Not all of these scattering mechanisms are present in a material at the same time, or more precisely, not all of them contribute to the overall mobility in the same way because of the fact the one can dominate over the others. The rule regulating the scattering mechanisms and therefore the mobility in a material is the Matthiessen'rule:

$$\frac{1}{\mu_{tot}} = \frac{1}{\mu_{impurities}} + \frac{1}{\mu_{phonons}} + \frac{1}{\mu_{grainboundaries}} + ... \qquad (1.7)$$

where every single mobility is the mobility that the material would exhibit if only one scattering mechanism is present.

1.0.2 Materials

TCOs can be made out of different materials and combination of metal oxides. Several reviews are present in literature and the material choice mainly depends on which application the material is designed for [22] [3] [23]. The following tables are a non-exhaustive overview on the most used materials for certain applications (Table 1.1) and the most common way of doping them (Table 1.2).

The present work aims to investigate the physical properties of a certain class of transparent conductive oxides *i.e.* tin-based TCOs, with the goal of substituting the indium-based ones, industry standard but expensive and scarce. The response of such TCOs to high temperature thermal treatments is also investigated since many applications need the TCO to survive to high temperature with well preserved optoelectronic properties. From the first experimental results, several hypothesis on the microstructural and electrical behavior of these TCOs with respect to annealing temperature are proposed and confirmed by the employment of additional experimental techniques and theoretical simulations

Table 1.1: Several TCOs and their peculiar properties from Gordon *et al.* [24].

Properties	Material		
	Simple	Binary	Ternary
High transparency	ZnO:F	Cd_2SnO_4	
High conductivity	In_2O_3:Sn		
High plasma frequency	In_2O_3:Sn		
High work function	SnO_2:F	$ZnSnO_2$	$Zn_{0.45}InO_{0.88}Sn_{0.66}O_3$
Lowest work function	ZnO:F		
High thermal stability	SnO_2:F	Cd_2SnO_4	
High mechanical durability	SnO_2:F		
High chemical durability	SnO_2:F		
Easy to etch	ZnO:F		
Good resistance to H plasma	ZnO:F		
Low deposition temperature	In_2O_3:Sn ZnO:B a-InZnO		
Low toxicity	ZnO:F SnO_2:F		
Low cost	SnO_2:F		
High mobility	CdO In_2O_3:Mo In_2O_3:Ti		

Table 1.2: Typical doping of TCO materials from Minami *et al.* [25].

Material	Dopant or compound
SnO_2	Sb, F, As, Nb, Ta
In_2O_3	Sn, Ge, Mo, F, Ti, Zr, Hf, Nb, Ta, W, Te
ZnO	Al, Ga, B, In, Y, Sc, F, Ge, Ti, Zr, Hf
CdO	In, Sn
Ga_2O_3	
Zn-SnO_2	Zn_2SnO_4, $ZnSnO_3$
ZnO-In_2O_3	$Zn_2In_2O_5$, $Zn_3In_2O_6$
In_2O_3-SnO_2	$In_4Sn_3O_12$
CdO-SnO_2	Cd_2SnO_4, $CdSnO_3$
CdO-In_2O_3	$CdIn_2O_4$
$MgIn_2O_4$	
$GaInO_3$	Sn, Ge
$CdSb_2O_6$	Y
Zn-In_2O_3-SnO_2	$Zn_2In_2O_5$-$In_4Sn_3O_12$
CdO-In_2O_3-SnO_2	$CdIn_2O_4$-Cd_2SnO_4
ZnO-CdO-In_2O_3-SnO_2	

combined. The results are put in perspective comparing them with the existing literature.

In the introductory chapter, an overview on what a TCO is and the basic working principles is given, together with its main structural and optoelectronic properties and main applications. A review on the industry standard materials is also explored and the perspectives on future compounds, based on their abundance and price, are finally presented. In the chapter dedicated to state-of-the-art, properties of tin-based TCOs are reviewed with the addition of a comparison with indium-based TCOs. Zinc tin oxide (ZTO) and tin oxide (SnO_2) are selected as main TCOs and a chapter is dedicated to the structural and optoelectronic properties obtained with respect to the annealing temperature and atmosphere. A focus is put on high temperature applications and how to achieve the fabrication of a TCO that preserves good electrical conductivity after high temperature treatments. Several trends, mainly linked to the material defects concentration, are highlighted from the simultaneous adoption of different techniques, which are further explored in the fifth chapter. This investigation allowed to confirm some of the hypothesis introduced in Chapter 4. Afterwards, with the goal of increasing the electrical conductivity of tin-based TCOs and following a theoretical screening study performed by a partner group in Basel, an experimental strategy is put in place and described in Chapter ??, in order to dope the ZTO. Two elements were retained from density functional theory (DFT) calculations because of their specific properties, iodine and bromine. A first attempt of doping is described in this chapter, using a spin coating technique to deposit the dopant-rich solution on top of several ZTO samples, fabricated with different geometrical configurations in order to maximize the doping probability. The last chapter is focused on the structural properties and growth mechanisms of tin-based TCOs and a comparison is done using indium-based ones as a benchmark (zirconium doped indium oxide (IZrO)). An extensive use of electron microscopy let to the recognition of common behaviors between the two classes of materials, which contributed to the proposition of two growth models that describes tin and indium-based TCOs.

CHAPTER 2

Tin-based TCOs – State of the art

2.1 Introduction

A transparent conductive oxide (TCO) is a material that is employed in many applications such as flat screens, organic LED and photovoltaic cells and has to possess two main characteristics: transparency to light up to the infrared part of the spectrum and high electrical conductivity in order to allow carrier transport. Indium-based TCOs represent the industry standard for these class of materials due to their optimal electrical and optical properties. Nevertheless indium is listed among the elements which are classified as scarce [26]. In particular, the European Commission issued a report where the economic importance is displayed against the scarcity of an element. This is reported in the graph of Figure 2.1 and indium is included in the critical materials. As reported by Lokanc *et al.* [28], even if the indium supply is currently sufficient to cover the worldwide demand, this statement could be not valid anymore in a near future. Figure 2.2 represents this forecast, taking into account the increase of photovoltaic-generated energy in the future together with the employment of indium for OLEDs and flat screens, these predictions are likely to be accurate.

Tin-based TCOs are also extensively used because of their wide bandgap and high stability, which makes them good candidates for corrosive environments.
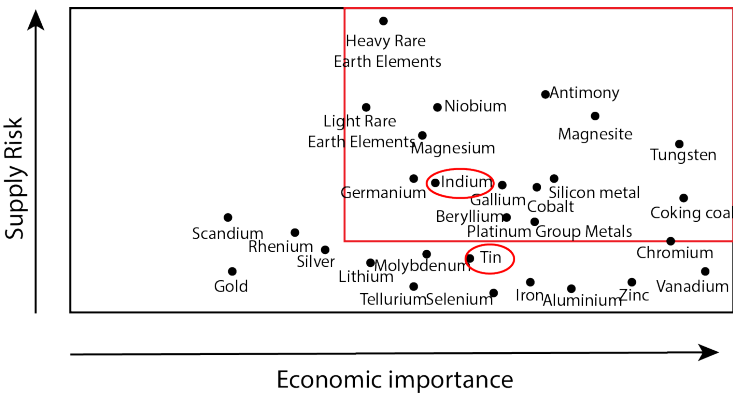
Figure 2.1: Scarcity with respect to economic importance of several elements used across different sectors. Inside the red square are materials considered as critical [27] (May 2014).
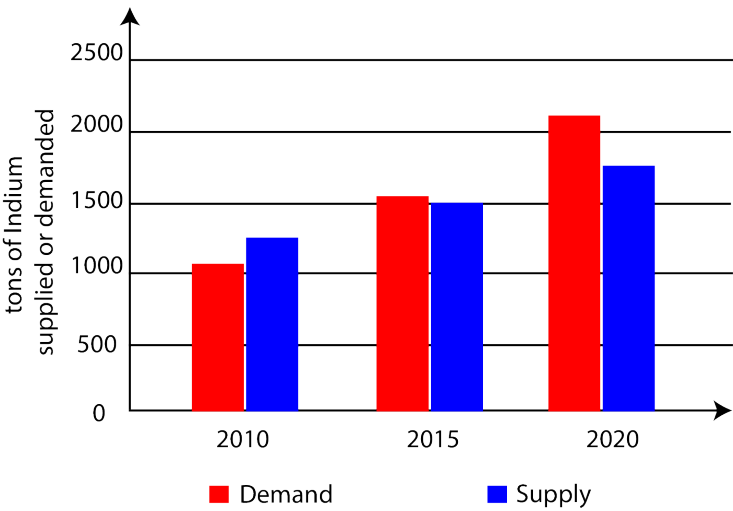

Figure 2.2: Forecast evolution for indium demand and supply mainly driven by flat panel displays and PV [29] (2011).
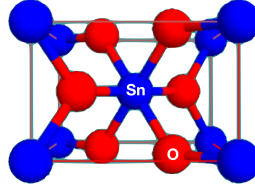
Figure 2.3: Rutile crystal structure of SnO$_2$ with one tin atom (blue) surrounded by oxygen atoms (red).

Moreover, tin is not included between the elements considered scarce. The purpose of this work is therefore to develop an indium-free TCO with a particular focus on tin-based ones.

Literature studies on tin-based TCOs show either optoelectronic or micro-structural properties of these materials, but little make the link between the two. In this chapter, the state of the art of tin-based TCOs properties is presented and, when possible, the link between the micro-structure and optoelectronic properties is highlighted. In the following sections the main characteristics of crystalline and amorphous phase of tin dioxide are reviewed together with the elements that are known to be good dopants for tin oxides. Finally, the last section is dedicated to the addition of zinc into a tin oxide matrix, which will be the focus of the experimental part of this work. Particular attention will be put on the influence that the annealing temperature has on the optoelectronic properties and the micro-structure of this class of materials.

2.2   Pure crystalline tin dioxide

The crystal structure of tin dioxide is rutile with a tetragonal unit cell where one tin atom has six oxygen neighbors (Figure 2.3). The lattice constants are $a = b = 3.188$ Å, $c = 4.738$ Å and $\alpha = \beta = \gamma = 90°$. The band diagram of tin dioxide has been simulated by many groups using different approximations such as Hartree-Fock pseudopotential and density functional theory (DFT) calculations [30]. Figure 2.4 shows the band diagram of SnO$_2$ as obtained by Mishra *et al.* [31]. The valence band maximum (VBM) and conduction band minimum (CBM) are both situated at the Γ point, highlighting a direct band gap. Values for the energy gap calculated by several groups sit around 3.9 eV [32] [33] [34].

It is known that the conduction band of SnO$_2$ is mainly formed by Sn *5s* orbitals, which are responsible for the high dispersion of the conduction band. On the other hand, the valence band is mainly formed by O *2p* states, therefore
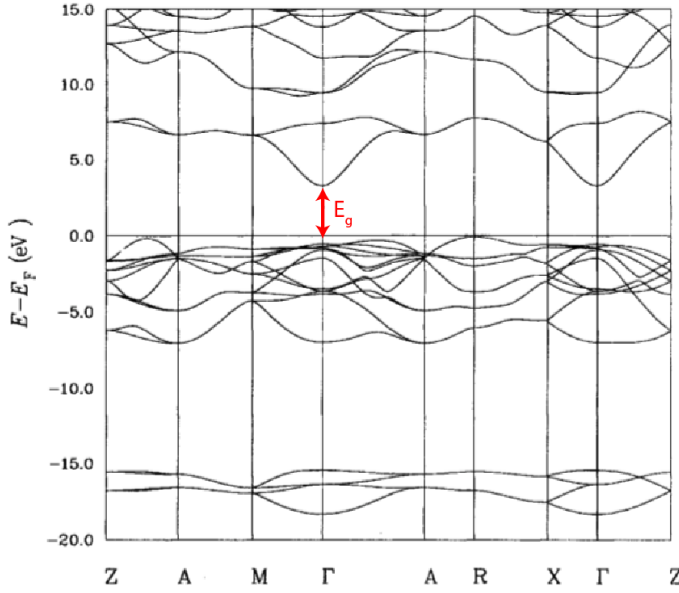
Figure 2.4: Tin dioxide band diagram around the gamma point Γ [31].

the dispersion of the density of states (DOS) near the valence band maximum is less pronounced. Figure 2.5 shows the contribution to the density of states of tin and oxygen orbitals. This is the reason why the hole effective mass is bigger than the electron effective mass. Sanon *et al.* calculated a hole effective mass of $\sim 1.0 m_0$ [35]. Theoretical calculations have proven that the mobility of charge carriers is high due to a low electron effective mass because of a high dispersion of the density of states near the CBM. Theoretical and experimental effective masses are found to be around 0.20 and $0.26 m_0$ depending on the crystallographic orientation (the tetragonal structure being anisotropic) [36]. Other groups found values around $0.40 m_0$ (experimentally) [37], $0.275 m_0$ [38] (experimentally) and $0.10 m_0$ [39] (theoretically).

Regarding the fabrication processes, it appears difficult to link the structural and optoelectronic properties of the material to one particular deposition method, since many parameters, such as stoichiometry, deposition temperature and atmosphere play a role all together during the process. Deposition techniques are generally divided into vacuum based and non-vacuum processes. The latter include spray pyrolysis, sol-gel processes, chemical vapor deposition at atmospheric pressure and electrodeposition. It is clear that each of these techniques results in a material with different optoelectronic properties that might also influence the post-deposition treatments needed to enhance the final prop-
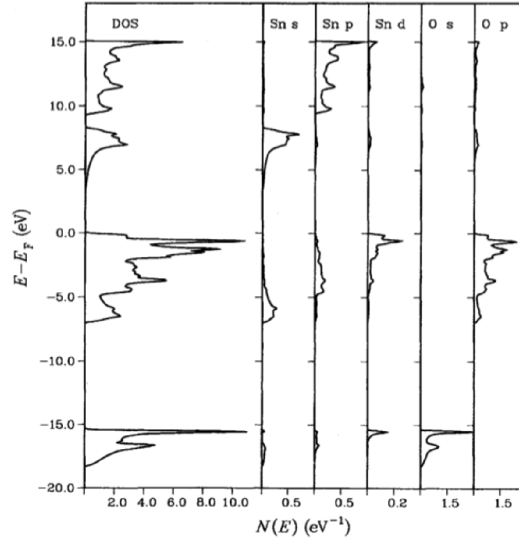
Figure 2.5: Contribution to the total density of states of single orbitals in undoped tin dioxide [31].

erties of the material. Indeed some processes are known to give a high quality material *e.g.* spray pyrolysis and CVD [40] and some others rely on post deposition annealing to obtain high conductivities [41]. Vacuum based processes can be divided into two categories: chemical vapor deposition methods (such as plasma enhanced chemical vapor deposition (PECVD), metal-organic chemical vapor deposition (MOCVD), low pressure chemical vapor deposition (LPCVD) or atomic layer deposition (ALD)) and physical vapor depositions (PVD) such as evaporation, pulsed laser deposition, ion plating and magnetron sputtering. CVD type processes, such as PECVD are most commonly reported for the deposition of front contacts TCOs used in amorphous/microcrystalline silicon thin film solar cells [42]. Regarding their applications, TCOs deposited mainly with non-vacuum techniques are the ones used for low-cost applications, such as anti-reflection coatings [43]. For solar cells, such as SHJ cells, the TCO is required to have higher quality opto-electronic properties, since these types of cells reach high efficiencies (>22%) and therefore vacuum-based processes are preferred. Regarding the physical processes, the main applications for TCOs are flat panel displays, touch screens, gas sensors, radiation shields and thin films for photovoltaics among others [44] [45] [46] [47] [48] [49] [50] [51] [52] [53] [54] [55] [56].

SnO_2 in its crystalline and stoichiometric configuration is not conductive, behaving as a non-degenerate semiconductor [57]. However, intrinsic defects such

as oxygen vacancies are able to donate electrons to the conduction band and brings conductivity to an otherwise insulating material [58]. An oxygen deficient tin dioxide structure is a structure where one or more oxygen atoms are missing from their sites (because of the chosen deposition parameters) and therefore two or more electrons, respectively are not linked in any chemical bond. These electrons can, if the vacancy is ionized, be donated to the conduction band. Using the Kröger-Vink notation an oxygen vacancy can be indicated as follows

$$O_O^x \rightarrow V_O^{\cdot\cdot} + 2e' + \frac{1}{2}O_2(g). \tag{2.1}$$
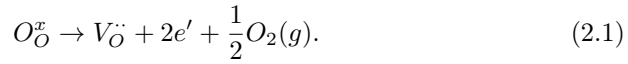
The presence of oxygen vacancies and therefore free electrons in the conduction band transforms the material into a degenerate semiconductor, creating shallow levels [59] near the CBM. Several theoretical calculations were conducted in order to study the formation energies of intrinsic defects in tin dioxide, with the goal of understanding which are the ones most likely to occur in the SnO_2 structure. Together with oxygen vacancies (V_O), tin interstitial (Sn_i), tin antisite (Sn_O), tin vacancy (V_{Sn}) and oxygen interstitial (O_i) were studied [60]. Sn_i and V_O are those that produce the majority of defects in SnO_2 and that are responsible for the conductivity of the material. The fact that these defects produce shallow levels next to the CBM is the reason why SnO_2 can be conductive and transparent at the same time [61]. Indeed, when the defect is placed at mid gap, it act as a recombination center for the charge carriers. The trade-off between electrical conductivity and transparency arises from the fact that adding charge carriers in CB translates in increasing the absorption of the material in the infrared part of the spectrum via the relationship $\lambda_p \sim \sqrt{N}$, where λ_p is the absorbed wavelength and N is the carrier density [62]. The coexistence of electrical conductivity and optical transparency in SnO_2 can be associated to the shallow donor levels located near the CBM, that are formed because of a large concentration of oxygen vacancies [63]. Nagasawa *et al.* deposited a non intentionally doped single crystal tin dioxide with an average conductivity of $4\,\mathrm{S\,cm^{-1}}$, a carrier concentration of $10^{17}\,\mathrm{cm^{-3}}$ and an average mobility of $200\,\mathrm{cm^2\,V^{-1}\,s^{-1}}$ [37]. These values represent a material with a low carrier concentration (compared to the usual doping levels) and therefore a high mobility.

Intrinsic defects are not the only way to increase the electrical conductivity in tin dioxide. In the following section an overview of the most known doping elements for tin oxide is reviewed.

2.3   Doping of tin dioxide

When a sufficient amount of ionized defects is introduced in a stoichiometric material, the Fermi level is shifted towards the conduction band allowing the transport of charge carriers. In addition to the intrinsic defects that can donate electrons to the conduction band, foreign elements can be introduced into the original material in order to dope it. Depending on the size of the dopant introduced in the SnO_2 structure, they can act as substitutional or interstitial dopants. Substitutional doping occurs when the alien atom has about the same size of the host one, whereas interstitial doping occurs when the sizes are significantly different. Interstitial doping is also known to create energy levels halfway into the band-gap, which act as traps and recombination centers. On the other hand, substitutional dopants are able to effectively donate electrons to the CB, enhancing the electrical properties of the starting material, creating energy levels right below the CB. In the case of tin dioxide, for a dopand to be substitutional, its ionic radius must be similar to the one of Sn^{IV} being $0.071\,nm$.

The main source of charge carriers for tin oxide is thought to be oxygen vacancies. Nevertheless other additional elements have been introduced with different concentrations into the tin oxide matrix and their effects have been studied by means of theoretical simulations and practical experiments. With respect to n-type doping, the most promising elements are antimony and fluorine. In particular, Sb^{5+} is thought to substitute a Sn^{4+} whereas F^{1-} sits on a O^{2-} site [64] [65]. Also, molybdenum, tantalum and chlorine are known to act as donors for tin oxide [66] [67]. All of these elements are able to donate an electron in CB. Fluorine, for example, does not contribute greatly to the distortion of the crystal structure, given its similarity in ionic radius to oxygen. On the other hand, chlorine has a bigger radius, which leads to slight distortions of the unperturbed crystal structure. Some cations that might dope tin dioxide can be multivalent and therefore assume at least two different oxidation states while incorporated in tin dioxide. Elements of groups II and III, such as In, Ga, Al, Fe and Zn, are thought to create acceptor-like states in SnO_2. The doping level is highly dependent on the element and the initial characteristics of the starting material [68] [69] [70] [71]. Typical values of carrier concentration and mobility for poly-crystalline tin dioxide are around $15 \times 10^{19} cm^{-3}$ and $20\,cm^2\,V^{-1}\,s^{-1}$ as reported by Agashe *et al.* [72]. The applications for which tin dioxide is used depends strongly on its electrical conductivity. The doping of the structure is the main discriminating factor in determining the electrical conductivity, which can vary in a range between $10^{-6} S\,cm^{-1}$ [73] and $1.2 \times 10^4 S\,cm^{-1}$ [74] [72].

When adding elements of group III of the periodic table to SnO_2, the conductivity usually drops because of their electronic structure. For the same reason,

Table 2.1: Carrier concentration and mobility of antimony doped single crystal tin dioxide analyzed by Fonstad and Rediker [79] at 300 K.

	N ($\mathrm{cm^{-3}}$)	μ ($\mathrm{cm^2\,V^{-1}\,s^{-1}}$)
Heavily doped sample	2.2×10^{18}	150
Doped sample	8.6×10^{16}	240
Not intentionally doped sample	8.5×10^{15}	260

adding elements of group V increases the overall conductivity as reported by Carrol *et al.* [75]. The same work explores the trend of electrical conductivity with respect to the amount of dopants added to the pure tin dioxide: while the conductivity first decreases with the addition of dopants, it begins to increase when the dopant concentration continues to increase up to an optimum that depends on the added element itself. Common dopants for tin dioxide are antimony, fluorine and molibdenum, all source of n-type conductivity [76]. In some cases the introduction of dopants does not modify the crystal structure of SnO_2 and the lattice parameters [65] [31]. Li, Ga, In and N are also largely used as tin dioxide dopands because of their ionic sizes similar to the one of tin [71] [77]. The defect level is usually calculated using theoretical simulations that combine a mixture of Perdew-Burke-Ernzerhof (PBE) and Heyd–Scuseria–Ernzerhof (HSE06) approximations and they converge in the description of defects whereas they usually fail in the calculation of the energy gap [78]. Typical values for tin dioxide conductivity vary depending on many factors, such as doping, deposition methods, deposition temperature and pressure. Jarzebski *et al.* [58] reported several values for crystalline tin dioxide conductivity depending on the deposition temperature and method. In the following literature review, the deposition parameters and methods, such as deposition temperature (T_d), pressure (P_d), type of substrate, etc. will be given (when stated in the original paper) in order to present a solid comparison between different studies.

Fonstad and Rediker [79] studied the scattering mechanisms in crystalline tin dioxide as a function of measurement temperature. Several single crystal antimony-doped tin dioxide samples were deposited using chemical vapor deposition and the electrical properties were measured using temperature-dependent Hall effect. At 300 K the obtained values are reported in table 2.1. The trend highlighted in table 2.1 confirms that when dopants are added to the crystalline form of tin dioxide, the material starts to have a considerable amount of charge carriers in CB. Samson and Fonstad [63] studied the influence of annealing atmosphere and temperature on crystalline tin dioxide samples using different oxygen partial pressures and annealing time. They compared the carrier concentration, measured at room temperature, of samples before and after annealing. Table 2.2

Table 2.2: Single crystal undoped tin dioxide samples analyzed by Samson and Fonstad [63] annealed and quenched.

N at room temperature (cm^{-3})	Annealing temperature (°C)	Oxygen partial pressure (atm)	Time (h)	N (cm^{-3})
1.44×10^{16}	1450	1	14	4.5×10^{17}
0.9×10^{16}	1350	1	14	3.3×10^{17}
/	1400	0.21	14	3×10^{17}
high ρ	1275	1	20	1×10^{17}
high ρ	1275	1	20	9×10^{16}

shows the results. The samples reported in this table are all nominally undoped. It is interesting to notice here that the overall carrier concentration increased after the thermal treatments from an average value of $1 \times 10^{16} cm^{-3}$ to the ones highlighted in the table. From previous analysis conducted by the same group, it was known that two donor levels, at $34 \, meV$ and $140 \, meV$ were active in the tin dioxide crystals before annealing. The increase of carrier concentration in CB after annealing is thought to be due to the donation of carriers to the CB from these donor levels. Fonstad and co-workers claimed that these levels are associated to doubly ionized oxygen vacancies. No considerable difference is observed between samples annealed in different oxygen partial pressures.

Transport mechanisms in SnO_2 are governed by different factors and depend on the investigated range of temperatures and on the structure of SnO_2. At room temperature, the conduction of undoped single crystal SnO_2 appears to be dominated by optical phonon scattering [79] whereas when doping is introduced, whether intentional or not, the material behaves as a degenerate semiconductor and the main scattering mechanism is due to ionized defects. For polycrystalline SnO_2 films, in addition to the previously mentioned scattering mechanisms, the presence of grain boundaries has to be taken into account. Grain boundaries would, indeed, act as a trap for electrons, decreasing the overall conductivity [80], becoming the dominant scattering mechanism. In the aforementioned studies it is reported that films with larger grain size have better electrical properties. Regarding high temperature treatments, some authors claim that annealing polycrystalline SnO_2 in an inert atmosphere or in vacuum might lead to an increased film mobility ($60 \, cm^2 \, V^{-1} \, s^{-1}$ *vs.* 1 to $20 \, cm^2 \, V^{-1} \, s^{-1}$) most probably due to grain growth [79].

In order to investigate which elements would be a good candidate to dope tin oxide, a preliminary theoretical study was conducted by the group of Prof.
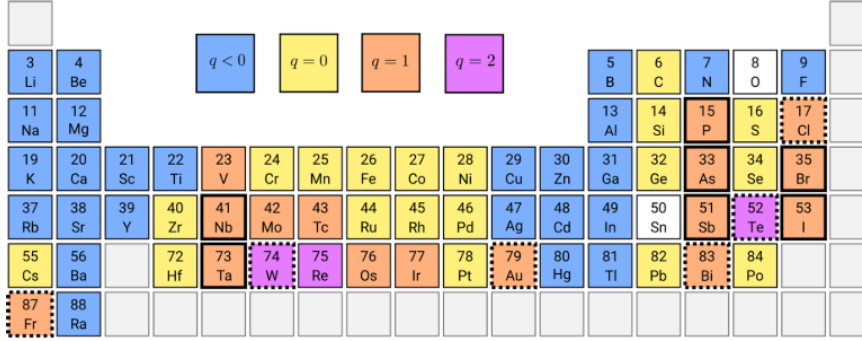
Figure 2.6: Stable PBE charge state of a substitutional atom on a Sn site, when $\Delta\epsilon_F$ is at the CBM. The elements are highlighted in different colors to distinguish the charge state: in blue, q<0; in yellow, q=0; in orange, q=1 and in purple, q=2. The thick black outline indicates no localized defect states, and the dashed outline indicates elements with intriguing behavior at the CBM [81].

Goedecker and in particular by a PhD student in the group, Miglé Graužinyte, from the Department of Physics at Universitaät Basel in Switzerland. In their study, Graužinyte *et al.* [81] conducted several theoretical simulations screening the whole periodic table with the goal of assessing which elements are energetically prone to acting as dopants for crystalline SnO_2. A PBE0 hybrid functional method was used, which predicts the good gap for SnO_2 and allows to perform a parameter-free large-scale defect study on SnO_2. This study is referred to as a large-scale study because not only the behavior of isolated defects is studied, but also the overall doping trends. In these simulations, 63 dopants were considered as substitutional dopants for the tin site. Super cell of SnO_2 used for this study was one composed by 72 atoms. Calculations using pure PBE predict 19 elements as potential n-type dopants (with the Fermi energy level at the bottom of CB), because they are positively charged. This means that one or two electrons are donated to the conduction band (represented in orange and purple, respectively, in Figure 2.6). The n-dopants were further separated into three categories, i) the elements that do not affect the electronic structure of SnO_2 and therefore should act as good donors (outlined by a black solid line), ii) elements that do not form electronic states inside the band gap but nevertheless distort a lot the bottom of the conduction band (outlined by a black dashed line) and iii) transition d metals resulting in defect states inside the band gap due to metal-d and O-$2p$ orbital interactions. It is important to mention here that the overall goal of the study is to find dopants that do not create defect states inside the SnO_2 band gap, because they would act as trap centers or recombination states, decreasing the conductivity of the material and increasing the optical absorption. Moreover, they would contribute to
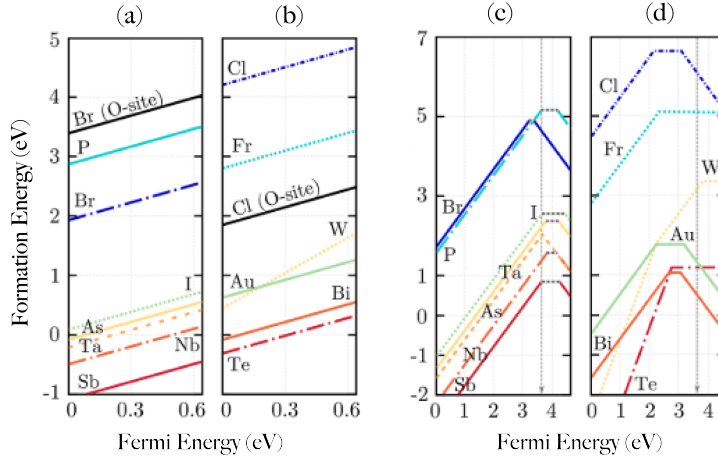
Figure 2.7: Formation energy with respect to the position of the Fermi levels for different elements considered as dopants in the study. Panels (a) and (b) report the results obtained using a pure PBE whereas panels (c) and (d) using a PBE0 approximation. The predicted trend remains mostly the same for elements that do not distort the DOS of the material and do not introduce defects inside the band gap ((a) and (c)), but the prediction of PBE is completely reversed when using PBE0 for those elements that cause strong distortion next to the CBM [81].

decrease the energy gap itself, decreasing the overall transparency of the TCO. To further investigate the substitution of dopants either in a tin or oxygen site, Graužinyte *et al.* calculated the formation energies for the three categories of n-type dopants discussed above. They did the same calculation using first a pure PBE approximation and then a PBE0 approximation The main difference between the two methods is that the PBE0 mixes the PBE exchange energy and Hartree-Fock exchange energy with a relative proportion equal to 3:1, with the full PBE correlation energy [82]. Results are shown in Figure 2.7. For simplicity just the first and second categories are reported in the figure. When the calculation is conducted using PBE approximation, it predicts one stable charge state for all the defects in a tin site (they result to be in a donor state), but when the approximation is slightly changed in order to span a bigger range of energies for the Fermi level, it is seen that some defects have the tendency to change charge state, starting from a donor state and becoming acceptors. This is proven to happen mainly when the Fermi energy approaches the CBM. The bigger differences can be seen in the group of elements that distort the vicinity of CBM, *i.e.* in Figure 2.7 from the case (b) to the case (d). In the same figure, in (a) and (b) are also presented the cases of bromine and chlorine when they act as substitutional dopants for the oxygen site instead of the tin site, these two are the only elements whose formation energies are still favorable. The rest

of substitutional dopants in an oxygen site have formation energies too high to be probable. The most favorable elements, to act as good dopants in tin dioxide, arising from this investigation are potentially the ones included in graphs of Figure 2.7, but in particular, those that can be substitutional for both oxygen and tin sites, without being energetically too expensive, such as bromine and chlorine, are even more favorable.

The electronic structure arising from doping was also investigated in this study, the goal was to verify that the dopants would not introduce any localized state inside the band gap. Some of them do introduce localized defect states next to the VBM, but remain shallow enough to not be detrimental for electrical and optical properties of SnO_2.

2.4   Amorphous tin-based TCOs

In its amorphous phase, tin dioxide is a suitable material to be used on flexible/light weight substrates. Many authors reported about the existence of amorphous tin oxide, but very little is known about its electrical properties. The conductivity of amorphous tin dioxide is included between 1 and $500\,\mathrm{S\,cm^{-1}}$ [83]. Chen $et\ al.$ deposited a thick ($6\,\mu\mathrm{m}$) tin-dioxide sample by pulsed laser deposition that became crystalline after heat treatment [84]. The base pressure was about 10^{-6} mbar, the working pressure was about 2×10^{-6} mbar. The deposition was carried out on top of silicon substrates and at room temperature, samples were then annealed for 2 hours at $150\,^{\circ}\mathrm{C}$. Nevertheless, no indication about the electrical properties was reported in this study. Lekshmy $et\ al.$ [85] reported also that an amorphous as deposited tin dioxide sample, became crystalline after annealing in oxygen atmosphere at $350\,^{\circ}\mathrm{C}$, whereas the films annealed in air at $350\,^{\circ}\mathrm{C}$ stayed in its amorphous phase. The crystalline films exhibited SnO_2 rutile crystal phases during XRD experiments (in particular (110), (101) and (211) orientations). The starting material was deposited by sol-gel dip coating on a quartz substrate. No electrical properties were reported in this study. Shin $et\ al.$ [86] used anodic oxidation of pure tin metal to deposit tin oxide, obtaining an amorphous as-deposited tin dioxide becoming crystalline after annealing at $500\,^{\circ}\mathrm{C}$ for three hours. No information about electrical properties is reported. Jousse $et\ al.$ [87] deposited tin dioxide films using chemically sprayed techniques and reported dependence on the substrate deposition temperature of the electrical properties for an amorphous tin dioxide and a polycrystalline one. Figure 2.8 summarizes their findings. Overall, the trend is that an as-deposited tin dioxide film becomes crystalline if submitted to high temperature treatments, but little is known about the electrical properties of such materials and how they evolve with respect to the annealing temperature.
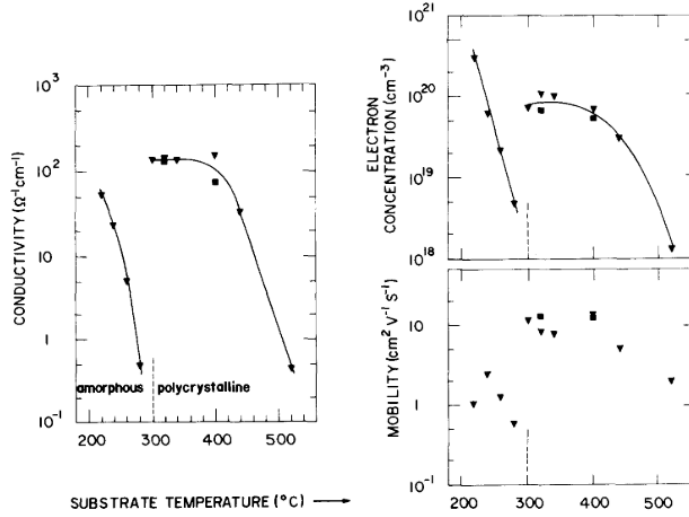
Figure 2.8: Electrical conductivity, carrier concentration and mobility of tin diox-
ide samples (amorphous and polycrystalline) versus substrate deposition temperature,
reported by Jousse *et al.* [87]. Conductivity of amorphous and polycrystalline samples
are comparable at the starting temperatures.

Wang *et al.* [88] prepared tin dioxide films, under various flow ratios of O_2-Ar
on unheated glass substrate and using ion beam sputtering deposition. They re-
ported the change in electrical resistivity with respect to annealing temperature
to be dependent on the amount of oxygen dispersed in the annealing atmo-
sphere. In particular, the higher the oxygen partial pressure, the higher the
resistivity, since the amount of oxygen vacancies, responsible for the creation
of carrier concentration, is thought to decrease. This trend is shown in Figure
2.9. Hemissi *et al.* [89] conducted annealing experiments of Sb-doped tin oxide:
the samples annealed at $500\,°C$ present better electrical properties than the ones
conducted at $600\,°C$. Moreover, a clear dependence on the annealing time is also
highlighted. The trend in this case is non-linear but presents a local minimum
at 120 minutes. The reason for this behavior is ascribed to the increasing size of
crystalline grains with annealing time. More on this subject will be investigated
in the chapter dedicated to the results of this work.
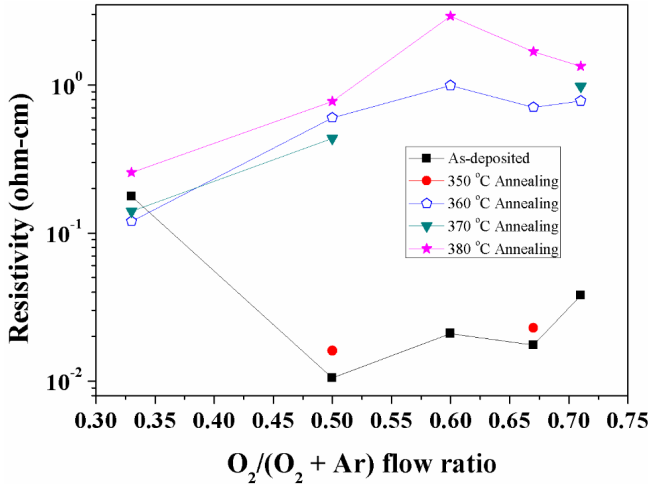
Figure 2.9: Variation of the electrical resistivity of tin dioxide films deposited with various flow ratios of $O_2/(O_2 + Ar)$ at the annealing temperature from $350\,^\circ\text{C}$ to $380\,^\circ\text{C}$ and a working pressure of $4.7 \times 10^{-2}\,\text{Pa}$ [88].

2.5   Effect of the addition of zinc in double oxides

The evolution of tin dioxide electrical properties with respect to the annealing temperature is related to many factors such as the annealing atmosphere and the amount of defects dispersed in its structure. On the other hand, if the starting material is crystalline or amorphous, it might behave differently upon thermal treatments. It was also assessed that once the material is submitted to annealing, the drop in electrical properties depends on the ability of the tin dioxide of preserving a decent amount of charge carriers dispersed in its structure so that the annihilation or passivation of these defects is delayed. One strategy that can be adopted in order to introduce more defects into the structure can be to introduce different species inside the double oxide matrix so that the degree of disorder, in the case of an amorphous material, increases and with it the probability of donating electrons to the conduction band [90]. In order to shift the drop of SnO_2 electrical properties towards higher temperatures, not only a foreign element has to be introduced into the tin oxide matrix in order to act as a donor, but also and more importantly, the element has to have proven properties of keeping the electrical properties of the material stable upon thermal treatments.

Figure 2.10 shows a summary of the electrical conductivities of the ZTO and IZO found in literature with respect to the annealing temperatures. The stoi-

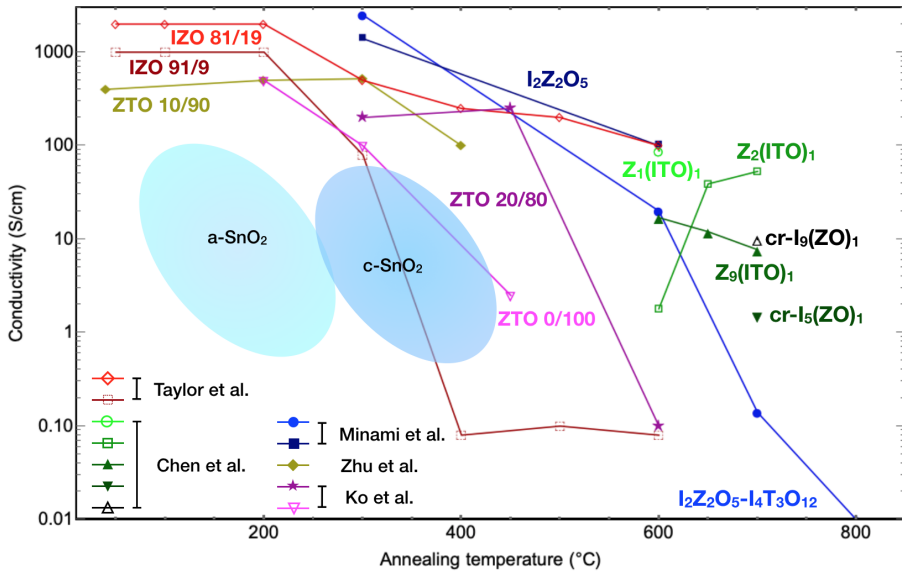**Figure 2.10:** Summary of some of the electrical conductivities vs. annealing temperature found in literature of zinc-enriched TCOs. The figure refers mainly to ZTO and IZO with different stoichiometries. If not specifically indicated, the materials are in the amorphous phase ("cr" meaning crystalline material). All the thermal treatments were conducted in air. As a comparison, two semi-transparent blue regions indicate the average conductivity for amorphous and crystalline tin oxide. These data are taken from the literature review presented in this chapter.

chiometry of the materials is not the same for every study and also the deposition methods can vary completely from one study to another. Nevertheless it is interesting to compare the curves within the same color code and the overall trend confirms that the presence of zinc enhances the thermal stability of the correspondent binary TCO. Each and every TCO shown in Figure 2.10 is amorphous in its as-deposited state and remains amorphous across the presented temperature range, the only exception being the I_9ZO_1 and I_5ZO_1, which are in the crystalline state at 700 °C. The feature highlighted in Figure 2.10 underlines the fact that adding zinc in the original matrix of tin and indium-based TCOs has the effect of postponing the drop in electrical conductivity with respect to the annealing temperature. Indeed, the average conductivity of tin oxide without any zinc addition is found to drop once the threshold of 400 °C is crossed. In the previous section several studies reporting on the acceptor-like characteristic of zinc added into a tin dioxide matrix is not observed in the materials described in Figure 2.10. Zinc does not seem to alter the as-deposited electrical conductivity of tin oxide. Dinner *et al.* [91] demonstrated that annealing a zinc doped

indium oxide leads to a stability of the material up to $500\,^\circ$C in a mixture of N_2 (95%) and H_2 (5%) atmosphere. In this study it is highlighted that the crystalline phase of the presented materials is electrically conductive and that the resistivity appears to only depend on the concentration of indium in the film. Minami *et al.* [92] compared the behavior under thermal treatments of SnO_2, ZnO and a mixture of amorphous SnO_2-ZnO. The conductivity depends on the relative concentration of tin oxide to zinc oxide, with a peak when the SnO_2 content reaches 80 wt%. Thermal treatments were carried out and it was found that the mixture SnO_2-ZnO was more stable compared to the single oxides, maintaining its electrical properties unchanged until a temperature of $350\,^\circ$C was reached in an oxygen-rich atmosphere. An increased chemical stability of the SnO_2-ZnO was also reported with respect to SnO_2 and ZnO alone. In a separate study, Minami *et al.* [93] investigated the high temperature annealing of ternary compounds containing zinc, revealing an average conductivity much higher with respect to compounds not containing zinc (shown in Figure 2.10). Taylor *et al.* reported that the addition of ZnO during the deposition of In_2O_3 significantly improved the thermal stability of the TCO, leading to a preserved electrical conductivity up to $600\,^\circ$C [94]. Jain *et al.* [95] also reported good electrical properties ($1.44\cdot10^{-3}\,\Omega\,\mathrm{cm}$) for a mixture film of In_2O_3 and ZnO annealed up to $450\,^\circ$C for one hour. In this case, the material is found to be crystalline in its as deposited state and thermal treatments are thought to increase the grain size and therefore decrease the scattering of carriers from grain boundaries. Zhu *et al.* [96] studied the local structure of amorphous and crystalline ZTO using a combination X-ray techniques for structural investigation such as extended X-ray absorption fine structure (EXAFS) and compared it to those of SnO_2 and ZnO. The addition of zinc is thought to improve the thermal stability of ZTO by increasing the crystallization temperature and keeping the material electrically conductive up to higher temperatures. The reason of this increased crystallization temperature seems to be linked to the strain added to the overall structure that might reduce the lattice thermal vibrations and increase the energy barrier towards crystallization. Ko *et al.* [97] investigated the effect of the addition of zinc into the tin dioxide amorphous network and performed annealing studies up to $600\,^\circ$C. The electrical conductivity presents a maximum around $250\,^\circ$C and then decreases as soon as the crystallization threshold is reached. Kim *et al.* [98] analyzed ZTO with different relative concentration of zinc to tin, reporting that the more zinc is introduced into the SnO_2 network, the more the crystallization is shifted towards high temperatures, reaching $600\,^\circ$C when the concentration of zinc to tin is 73:27. Jayaraj *et al.* [99] study two different compositions of ZTO in particular 1:1 and 2:1 (Zn:Sn), reporting that the films containing more zinc crystallize later and that as soon as the phase change occurs, the material becomes highly resistive. The crystallization is postponed the more zinc is added into the tin oxide network. Since the ZTO films were found to behave as degenerate semiconductors, the reason for the increased resistivity seems to be due to the poor crystallization, because of the presence of grain boundaries and

voids withing the structure. On the other hand, since the conductivity depends on the overlap between s orbitals in this class of materials, the overlap should be preserved even in the crystalline phase and despite longer bonds of the crystalline phase [96] and changes in the bond angles from the amorphous to the crystalline arranged structure. Chen *et al.* [100] reported on the crystallinity of zinc indium tin oxide (ZITO) and claimed that the material remains conductive even in its crystalline form, suggesting that the drop in electrical properties does not depend on the material phase but rather on a decrease of charge carriers as soon as high annealing temperatures are reached.

To summarize the properties of ZTO issued from the published analysis, the following points can be emphasized:

- the majority of as deposited ZTO samples are in the amorphous phase;

- regardless of the deposition method, when the amount of zinc into the SnO_2 network is increased, the resulting TCO is more resistant to high temperature treatments;

- electrical conductivity of ZTO increases upon thermal treatments, having a maximum at a certain temperature σ_{max} and then decreases when the crystallization threshold is reached;

- annealing atmosphere affects electrical properties of tin-based TCOs but the link between atmosphere and σ has not been systematically investigated;

- regardless of its structural phase, ZTO is found to be conductive and the drop in conductivity seems to be related to the decrease of charge carriers due to passivation of defects.

- in few cases, because of non-homogeneity of the crystalline structure, given by grain boundaries or point defects, the carrier transport appears to be more difficult.

Overall the general outcome that can be highlighted after the literature analysis is that further investigations must be carried out on the microstructural properties of the ZTO and focus on the influence that the TCO structure has on its electrical properties is of fundamental importance. In addition, the quality of the crystalline structure has to be deeply inspected. Furthermore, the impact of annealing atmosphere and temperature has to be separated from other parameters in order to better understand which are the effects on the conductivity. To answer these questions a combination of several techniques such as *in situ* X-ray Diffraction (XRD) and transmission electron microscopy (TEM), together with energy dispersive X-ray spectroscopy (EDX) are used in order

to inspect the microstructure of the material and study the evolution of its chemical composition with respect to annealing atmosphere and temperature. Opto-electronic properties of every sample are also recorded with respect to the annealing temperature and atmosphere. In order to experimentally test the theoretical results obtained from DFT calculations, a plan is set up to introduce the most favorable novel dopants into the ZTO matrix. Optoelectronic measurements and TEM/EDX analysis are carried out to study the impact of such dopants (iodine and bromine) on the ZTO properties. The general objective of this work is to understand the influence of thermal treatments on the microstructural and optoelectronic properties of ZTO, with the specific goal of separate the microstructural effects from the stoichiometry-linked ones on ZTO electrical conductivity. A growth model for tin-based TCOs is finally proposed and compared to the observations done on indium-based TCOs, in particular on zirconium-doped indium oxide.

Experimental techniques

The majority of the experimental techniques presented in this chapter were extensively used in this work. Other techniques and methods employed for specific experiments and investigations will be described in dedicated chapters. This chapter exposes the methods and parameters used for sample fabrication as well as for their characterization of both opto-electronic and micro-structural properties.

3.1 Deposition method

In order to deposit the thin films used for the present study, a Physical Vapor Deposition (PVD) System was used. This method imposes the source material to be transformed from the condensed phase to a vapor phase and then again to a condensed phase to form the desired thin film. In particular, a sputter deposition is the deposition of particles being ejected from a source target by a momentum-transfer from a bombarding particle (typically a gaseous ion) ionized by a plasma [101]. Figure 3.1 summarizes the scheme of the deposition system used in this work. The RF magnetron sputtering system works using an alternating current at high frequency that allows to sputter from metallic but also insulating targets because it avoids a charge building-up on certain positions of the target material. The magnets placed behind the targets create a magnetic
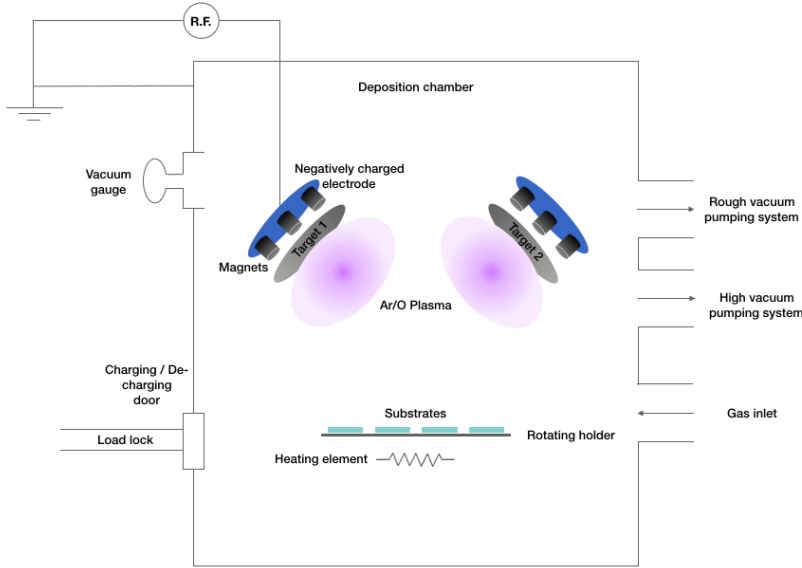
Figure 3.1: Scheme of the magnetron RF sputtering system used to deposit the TCOs that have been studied in this work.

field that trap electrons over the negatively charged target material so they do not directly bombard the substrate but instead enhance the ionization rate of the gases used in the plasma. These ionized particles are then free to hit the target, triggering a cascade reaction that allows the deposition onto the desired substrate [102]. The atoms ejected by the target are neutrally charged, so they are free to escape from the magnetic trap that keeps the ionized gas particle in its vicinity. It is crucial to point out that the atoms that leave the target surface have high kinetic energies with a large "tail" in the energy distribution that can be of several tens of eV [101]. In addition, because of the impact between target atoms and substrate, a displacement of bulk atoms and small "thermal spikes", as well as other types of damages may occur, so that the material surface may undergo crystalline-amorphous transitions [103].

3.1.1   Tin dioxide deposition

The deposition of tin dioxide, as well as of the majority of TCOs studied in this work was performed in a Leybold Univex 450B. The Univex is an RF magnetron sputtering machine equipped with a load-lock. The substrate is laid down into a rotating support, while the targets are positioned on top of the substrate, slightly

tilted and oriented towards it, with an average distance between target and substrate of 12 cm (Figure 3.1). The heating system works through an halogen lamp positioned below the substrate. Every target is closed by a shutter that can be controlled by the operator. The injection of gases, *i.e.* oxygen and argon, is controlled by two knobs and the amount can vary between 0 and 10 sccm for oxygen and 50 sccm for argon. It is crucial to mention here that the oxygen flow is actually a mixture of oxygen and argon with a ratio of 5/95, so that when the oxygen knob is set to 100%, it means that in the chamber are injected 0.29 sccm of oxygen. The optimized tin dioxide is deposited using a substrate temperature of 100 °C, an argon flow of 17% (equivalent to 12.3 sccm) and an oxygen flow of 40% (equivalent to 0.2 sccm). The initial pressure measured into the deposition chamber before injecting the gases is 7×10^{-7} mbar whereas the working pressure is 1.7 µbar. The used power is $1.01 \, \mathrm{W}^2 \, \mathrm{cm}^{-1}$. The deposition time depends on the desired thickness of the material.

3.1.2   ZTO deposition

The present study is focused on amorphous zinc tin oxide previously optimized starting from a deposition using co-sputtering from two targets: SnO_2 and ZnO [104]. Electrical, optical and structural investigation led to the development of a recipe using a single target, with the composition inspired by RBS and EDX analysis carried out on the co-sputtered films ($Zn_{0.05}Sn_{0.30}O_{0.65}$). The power density used during single target deposition was $0.32 \, \mathrm{W}^2 \, \mathrm{cm}^{-1}$, with a base pressure of 1×10^{-3} mbar. The electrical properties vary with the oxygen flow injected in the deposition chamber, reaching the best value when the amount of oxygen is equal to 0.1 sccm. The argon flow was kept constant and by reducing the working pressure from 1×10^{-3} mbar to 5×10^{-4} mbar the overall conductivity improved, enhancing the mobility while only slightly decreasing the carrier concentration. Substrates are heated up to 60 °C during deposition (since this appears to be the optimal temperature to obtain high conductivity-ZTO films). The ZTO films were deposited using two deposition systems: an Oerlikon Clusterline sputtering system and a Leybold Univex system. In both cases, the parameters used for every deposition are summarized in table 3.1. ZTO samples were deposited on two main types of substrates: glass or sapphire, in order to allow optical properties measurements and (100)-oriented silicon wafers, to avoid any interaction between the substrate itself and the film and to make micro-structural characterization easier, as well as on dedicated TEM grids. As insulating substrates, standard aluminoborosilicate glasses were used, whereas the standard silicon substrates were sometimes substituted with crystalline silicon with the addition of 300 nm of amorphous silicon oxide on top. The standard grids were CF200 meshed copper grids with a carbon film deposited on top (carbon thickness 6-8 nm) from Electron Microscopy Sciences

Table 3.1: Deposition parameters used for the ZTO fabrication

	Univex	Clusterline
Power density (W cm^{-2})	1.01	0.32
Base Pressure (mbar)	4.4×10^{-7}	1×10^{-3}
Working Pressure (mbar)	2.2×10^{-3}	5×10^{-4}
Ar/O_2 flow	3	5
Normal thickness (nm)	150	150

Company. In addition in order to avoid the copper EDX signal coming from the TEM grids, silicon nitride grids were also used (SiMPore UltraSM, Electron Microscopy Sciences Company).

3.1.3 Zirconium-doped indium oxide deposition

In order to compare tin-based TCOs to indium-based TCOs (Chapter 6), a zirconium doped indium oxide was deposited by sputtering onto aluminoborosilicate glass substrates and directly onto TEM grids. The deposition process was done by Esteban Rucavado on the Leybold Univex sputtering system that was used for tin oxide and zinc tin oxide. The single target had 98/2 weight composition ratio of $\text{In}_2\text{O}_3/\text{ZrO}_2$ with a target diameter of 10 cm and the RF power density was fixed to $0.95 \, \text{W}^2 \, \text{cm}^{-1}$. The deposition atmosphere was a mixture of argon and oxygen, with an initial base pressure of 10^{-6} mbar. After deposition, the films were annealed at $200 \, °\text{C}$ for thirty minutes under atmospheric pressure or under a pressure of 0.5 mbar of H_2 or N_2.

3.2 Electrical properties

To measure the electrical properties of bulk samples, a HMS-5000 *Hall Effect* equipment in the Van der Pauw configuration was used. This method allows to measure the mobility μ and carrier concentration N of a material and then to give an estimation of the conductivity if the thickness of the sample is known. Its working principle is based on the Hall effect: when a current flows across a

conductive sample and a magnetic field is applied to its surrounding, an electric field perpendicular to both the current and the magnetic field is induced in the sample. Measuring the voltage associated to this electric field, the so-called Hall tension, allows to understand what type of carriers, electrons or holes, are responsible for the current flow and enables to calculate the carrier concentration N:

$$N = \frac{IB}{hqV_H} \tag{3.1}$$

where I is the current that has been applied to the sample, B the magnetic field, V_H the Hall tension that can be measured and h the thickness of the sample. The conductivity can then be calculated using the following

$$\sigma = \frac{1}{R_{sh}h} \tag{3.2}$$

where R_{sh} is the sheet resistance and it is measured for every sample. The mobility is therefore calculated using the known relation

$$\mu = \frac{\sigma}{eN} \tag{3.3}$$

where e is the electron charge and N the carrier concentration. It is fundamental to highlight that in order to precisely calculate the N, σ and μ values, the sample thickness has to be given as an input. It is measured here using an Ambios technology XP-2 profilometer.

3.3 Optical properties

3.3.1 UV-VIS-IR Spectroscopy

Optical properties such as transmittance T and reflectance R were measured using a Perkin-Elmer Lambda 900 spectrometer in the UV-VIS-IR regions of the spectrum. For those measurements, all samples were deposited on top of aluminoborosilicate glass. If I_0 is the intensity of a monochromatic beam of wavelength λ arriving with normal incidence on the sample surface, this beam will be partly transmitted and partly reflected back by the sample itself. The transmitted and reflected intensities, I_T and I_R, are obtained by the integration over all the directions done with the help of an integrating sphere. The total transmittance and total reflectance are defined as follows:

$$T = \frac{I_T}{I_0} \qquad R = \frac{I_R}{I_0} \tag{3.4}$$

For the characterization of a TCO, it is important to measure not only the amount of light that is transmitted through it but also the amount of absorbed

light. The transmitted radiation depends on the multiple back and forth reflections that the radiation undergoes because of the presence of top and back surface of the sample, which act as separation barrier between media with different refractive indexes. These beams interfere with each other in a constructive or destructive manner depending on the thickness of the sample. Therefore, absorptance, transmittance and reflectance are all related by the formula

$$A = 1 - T - R \tag{3.5}$$

Calculating the absorptance allows an estimation of the material band gap, the free carrier absorption in the infrared part of the spectrum and the presence of defects inside the band gap. In particular, through the Beer-Lambert law

$$T = \frac{I_T}{I_0} = e^{-\alpha h} \tag{3.6}$$

it is possible to calculate α, the absorption coefficient of the material knowing h, its thickness and measuring the transmittance T. Then, since the absorption coefficient due to interband transitions (near the band-gap) is described by the Tauc law

$$\alpha \hbar \omega \propto (\hbar \omega - E_g)^2 \tag{3.7}$$

E_g, the optical band-gap can be extracted from the optical measurements. The exponent of the previous relationship is chosen because the interband transitions are considered to be direct and allowed.

3.3.2 Photothermal Deflection Spectroscopy (PDS)

Photothermal deflection spectroscopy is a technique that allows to characterize with high sensitivity the light absorption at the band edge of a material and further, to access the information about the density of states if the band structure is known. The physical principles of this technique are the following: an incident beam (modulated radiation) in a non-absorbing medium passes through the sample (absorbing medium), the energy dissipated in the sample will diffuse in all directions giving rise to temperature variation $\Delta T(x, y, z)$, which in turn is responsible for a variation of the medium refractive index. This variation can be employed to deflect a laser beam directed parallel to the sample by an angle ϕ from its original path. Measuring this deflection angle allows to calculate the absorption coefficient α of the investigated samples [105] [106]. As stated before, the access to the absorption coefficient gives an information about the optical gap. These measurements are used to precisely compare the sub-gap absorption of the studied materials before and after thermal treatments and to extend the knowledge about what type of defects are responsible for the changes in optical properties.

3.4   Micro-structural characterization techniques

In the following sections, the main techniques used for the structural characterization of studied TCOs are presented. The investigations vary from the macroscopic scale, using X-ray diffraction, to the nano scale with the use of electron microscopy and relative chemical analysis.

3.4.1   *In situ* X-ray Diffraction

In order to investigate the structure of the deposited samples, X-ray diffraction (XRD) was one of the most extensively used techniques. In particular an *in situ* diffractometer was used to conduct heating experiments. This tool allows to heat a sample while continuously acquiring XRD patterns. The goal was to track the evolution of the sample structure, highlighting any potential change in it during a heat treatment. The samples dedicated to this technique were deposited on silicon substrates in order to avoid any melting of the substrate itself at high temperatures.

This technique is based on the diffraction principle which is the interaction between an electromagnetic wave of a certain energy and the crystalline structure of the sample. The diffraction itself is a scattering phenomenon in which a large number of atoms play the role of multiple scattering centers arranged in a periodic fashion and scatter incident light. The fact that atoms are periodically arranged in a crystal makes the scattered rays to have a definite phase relation between each other (coherent scattering). This relation can lead to a constructive or destructive interference. In the former case, diffracted beams are created in certain directions and can be detected.

The diffraction is governed by the Bragg law, which states that

$$\frac{n\lambda}{2d} = \sin\theta \tag{3.8}$$

where λ is the incident wavelength and d the spacing between adjacent crystal planes. $n\lambda$ must be less than $2d$ for the law to be valid. d is on the order of $3\,\text{Å}$ or less, hence, λ cannot exceed about $6\,\text{Å}$. If $n = 1$, which means the diffraction is occurring between the adjacent crystal planes, the Bragg law can be written as follows

$$\lambda = 2d\sin\theta \tag{3.9}$$

If this condition is met, diffracted beams can be detected by the Bruker LYNX-EYE, a 1D detector composed by 255 channels, each of them being a single detector. This type of detectors makes the acquisition much faster with respect
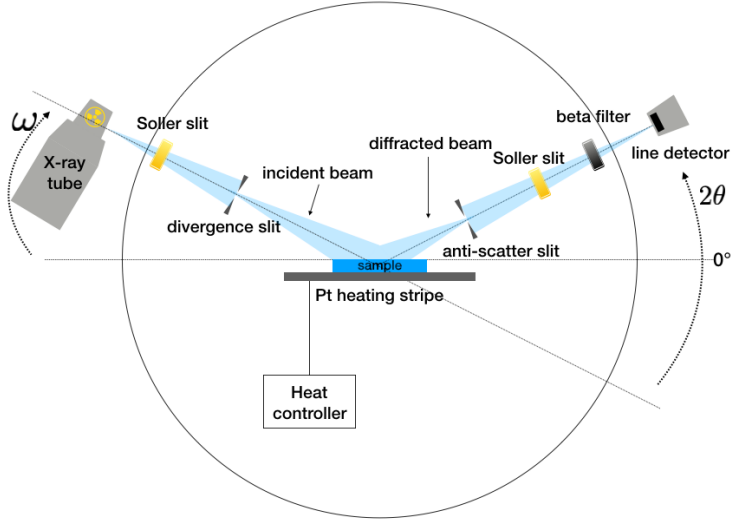
Figure 3.2: Schematic representation of the X-ray diffractometer used during the *in situ* heating experiments in a $\omega - 2\theta$ configuration.

to the standard scintillation counter. The detector is positioned at the sample exit, as shown on the scheme in Figure 3.2, that represents the geometry of a typical positioning between the X-ray source, detector and sample. For the experiments presented in the following chapters, a PANalytical X'Pert PRO equipment was used, equipped with an X-ray source of copper (K_α line of copper being $\lambda = 0.1541$ nm), in a $\omega - 2\theta$ configuration. The crystallography of TCOs was investigated in the majority of the cases using 1×1 cm samples, in a scanning range comprised between $20°$ and $80°$. Once the diffracted beams are detected, they can be represented in an x-y graph where the intensities of diffracted beams are displayed versus the angle θ that represents the direction to which each beam has been diffracted. The peak intensity is related to the number of elementary cells through the formula

$$I_{\max} \propto n^2 \left| F_{hkl} \right|^2 \tag{3.10}$$

where n is the number of elementary cells and $|F_{hkl}|$ is the scattering amplitude with which each of the cells contributes to the total scattering amplitude $n\left|F_{hkl}\right|$. If the crystal is now separated into two equal halves, each of thickness $t/2$ (where t is the total thickness of the crystal), the total scattered amplitude for each crystal is now $n/2\left|F_{hkl}\right|$, therefore the peak intensity is proportional to $n^2/4\left|F_{hkl}\right|^2$. So if the two intensities are added together, the maximum intensity becomes

$$I_{\max} \propto \frac{n^2}{2} \left| F_{hkl} \right|^2 \tag{3.11}$$

which is half of the single crystal value. On the other hand, the width of the peaks is doubled. The Scherrer equation states that:

$$\tau = \frac{K\lambda}{\beta \cos \theta} \tag{3.12}$$

where K is the shape factor, β is the line broadening, λ the X-rays wavelength and θ the incident angle. Following the same strategy used before, if the crystal is cut into two equal parts and hence the thickness divided into two, the broadening will increase. What remains constant is the integrated intensity, which is independent of the crystallite size in the specimen. From the XRD data it is also possible to extract the lattice parameters of the crystallized unit cell. In the case of this specific work, the unit cell of SnO_2 belongs to the tetragonal rutile crystal structures. The d-spacing is then related to the lattice constants a and c by the following relation:

$$\frac{1}{d^2} = \frac{h^2 + k^2}{a^2} + \frac{l^2}{c^2} \tag{3.13}$$

by substituting the Bragg equation $\lambda = 2d \sin \theta$ into the (3.13) the final expression is obtained

$$\sin^2 \theta = \left(\frac{\lambda^2}{4}\right)\left(\frac{h^2 + k^2}{a^2} + \frac{l^2}{c^2}\right) \tag{3.14}$$

From this last equation, the lattice parameters a and c can be calculated. The aforementioned development represents the theoretical base for the analysis that will be presented in the following chapters.

A platinum stripe was used as a heating element and sample holder, with a thermocouple connected to it in order to measure its temperature. A calibration was made in a separate experiment, with the X-ray source switched off (using three thermocouples, one sealed to the bottom of the platinum stripe, the second one attached to the top of the platinum stripe and the third one attached to the sample top surface). Figure 3.3 sketches the thermocouples position. The difference in temperature between the thermocouple sealed to the bottom of the platinum stripe and the one attached to the top of it was recorded while increasing the stage temperature ($\Delta T = T_1 - T_2$). This difference was associated to the fact that the contact between the thermocouple and the stripe was not perfect. It was assumed that both of these thermocouples should indicate the same temperature. Furthermore, the temperature on top of the sample was also recorded (T_3). The real temperature of the sample is then given by $T_{\text{sample}} = T_3 + \Delta T$. This correction is taken into account in all the calculations where XRD data were used as input.

In the case of ZTO, *In situ* annealings were performed in air and in vacuum (with a pressure of $\sim 5 \times 10^{-4}$ mbar) and with a constant heating rate
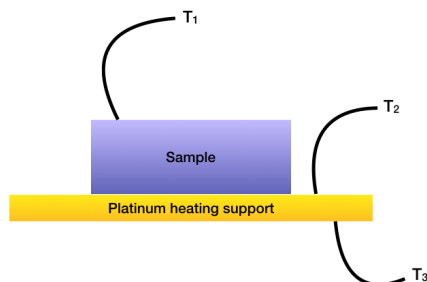
Figure 3.3: Scheme of the heating element in the diffractometer during the calibration step. Three thermocouples were attached respectively to the bottom of the platinum stripe, the top of it and the top of the sample.

of $5\,°\mathrm{C\,min^{-1}}$ with patterns acquired every four minutes in order to have a sufficient number of experimental points in every range of angles and an acceptable track of the evolution of the structure. Seven samples were annealed up to $200\,°\mathrm{C}$, $550\,°\mathrm{C}$, $570\,°\mathrm{C}$, $600\,°\mathrm{C}$, $650\,°\mathrm{C}$, $750\,°\mathrm{C}$, $1050\,°\mathrm{C}$ in air and once the maximum temperature was reached, they underwent a quick controlled cooling ($50\,°\mathrm{C\,min^{-1}}$). Four extra samples were heated in vacuum up to $200\,°\mathrm{C}$, $600\,°\mathrm{C}$, $900\,°\mathrm{C}$ and $1050\,°\mathrm{C}$ then similarly quenched. For SnO_2 three samples were annealed in air *In situ* at $300\,°\mathrm{C}$, $380\,°\mathrm{C}$ and $500\,°\mathrm{C}$, whereas at $600\,°\mathrm{C}$ and $700\,°\mathrm{C}$ in vacuum. To obtain a plot of the resulting data, a Mathematica code was developed to analyze the patterns in batch. The code consists of the following steps:

- XRD patterns are imported and data such as the starting time and temperature of each pattern are extracted;

- each and every pattern is displayed with the superposition of theoretical reflections of tin oxide, silicon (coming from the substrate) and platinum (heating stripe element) taken from the software JEMS [107] as indicated in Figure 3.4;

- the silicon 004 reflection is used to align the experimental data, as a shift can be induced by the initial misalignment of the sample and/or bending of the platinum stripe due to high temperatures;

- the background of each pattern is subtracted, using a top hat filter combined with a linear function;

- an algorithm finds the position of each peak;

- the fitting of each peak is performed using a pseudo-Voigt function. To avoid fitting issues induced by the $K_{\alpha2}$ shoulder, only the first half of the
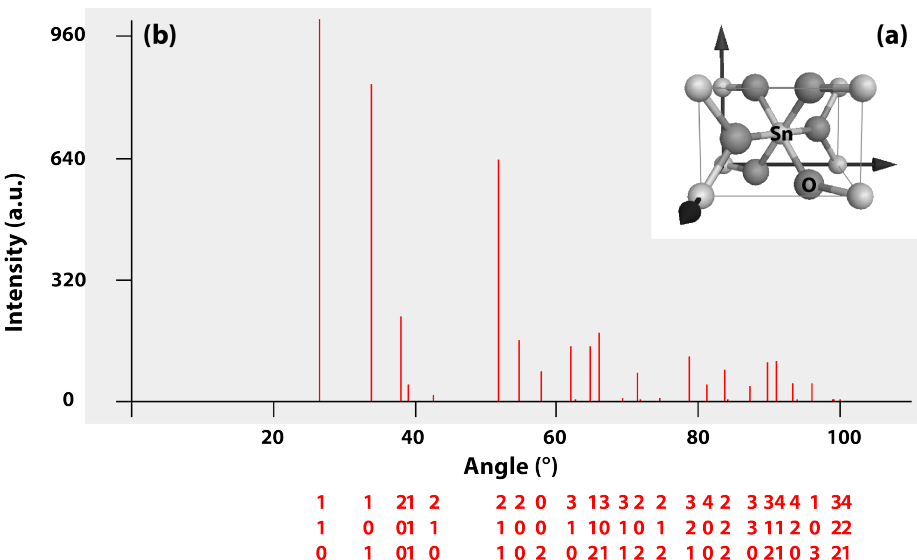
Figure 3.4: (a) Crystal structure of SnO_2 in its tetragonal form and (b) theoretical X-rays reflections for the K_α line of copper used as a source.

peak is fitted;

- the evolution of the peak intensity and full width at half maximum (extracted from the fitting) are tracked and from the latter, the crystal size is extracted using the Scherrer law [108] as written in equation 3.12. This procedure was applied for the main reflections of tin dioxide;

- the amorphous shoulder between $\theta = 20$ and $\theta = 32$ is integrated as reference;

- finally, the experimental lattice parameters are determined using equation 3.14.

3.4.2 Transmission Electron Microscopy

One of the experimental techniques that have been extensively used during this work to study the material microstructure is transmission electron microscopy (TEM). Because of the multiple modes of operation and the information that can be extracted from each mode, this technique is extremely versatile and useful for nanoscale material investigation.
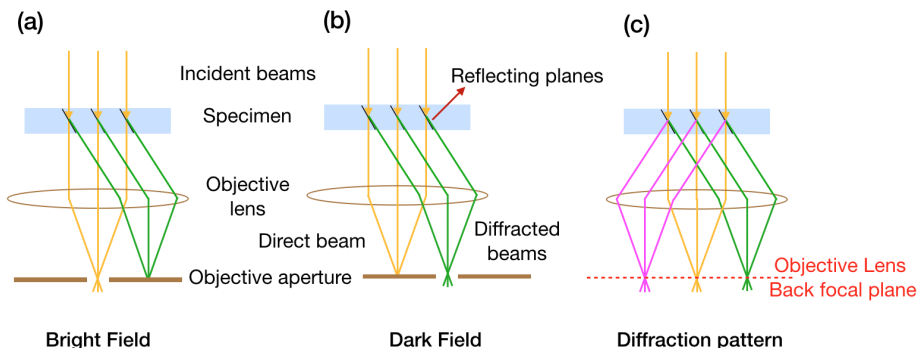
Figure 3.5: Operation modes for TEM: (a) scheme representing the position of the objective aperture when a bright field image is selected. (b) position of the objective aperture to obtain a dark field image and (c) objective aperture removed when the diffraction pattern has to be projected onto the fluorescent screen.

The electron microscope can be operated in two main modes, using a convergent beam that scans across the region of interest of the sample (STEM mode) or using a parallel beam fixed onto the region of interest of the sample (TEM mode). Regardless the chosen one, both modes of operation allow the formation of a bright field image (BF) and a dark field one (DF). In BF images (TEM mode), the electrons not interacting with the specimen and continuing in a straight line are selected by the objective aperture, positioned in the back focal plane of the sample, whereas in DF mode, the Bragg diffracted electrons collected by the objective aperture are projected into the fluorescent screen. A fundamental information about the sample structure can be extracted from the analysis of these two image modes. In addition, once removed the objective aperture and when the strength of the projection lenses of the microscope is changed, the operator can choose to project the back focal plane of the objective lens into the screen. By choosing this configuration, the diffraction pattern (DP) will appear on the screen. In this case the crystallographic orientation of the sample is revealed and by consecutive indexation of it, the unit cell type and its orientation can be reconstructed. Figure 3.5 shows a scheme of the three operation modes.

The other configuration largely used during the material investigation in this work is the aforementioned scanning transmission electron microscopy (STEM). In this mode a convergent beam scanned across the sample by a pair of *scan coils* is used and instead of hitting a fluorescent screen, the scattered electrons are collected by concentric detectors that integrate and register the signal pixel by pixel to then reconstruct the final image. Three complementary detectors can be used to form the image. The bright field detector (BF) intercepts the electrons

that go through the sample forward scattered. The annular dark field detector (ADF) is an annular detector that detects the electrons that have been scattered at low angles, *i.e.* the Bragg-diffracted electrons. The last and outer one is the high angle annular dark field detector (HAADF). This detector, because of its position, is able to detect all the electrons which have been scattered to high angles (Rutherford scattering). So the contrast of this detector relates to the mass and thickness of the sample: a heavier element will scatter more electrons to high angles, giving a brighter image. TEM and STEM analysis were carried out here using a FEI Tecnai Osiris microscope operated at 200 kV. The TEM camera is a 4k x 2.6k Gatan Orius CCD camera with large field of view and two sample holders were used during the investigations, a FEI standard single tilt and an FEI low background double tilt.

3.4.3   Energy Dispersive X-rays Spectroscopy

Two types of X-rays are emitted when electrons interact with matter: i) characteristic X-rays and ii) bremsstrahlung X-rays. The primary beam electron has a non zero probability to donate its energy to a core electron and eject it (above the Fermi level). This core electron will leave a hole in the inner shell and the atom in an excited state. The ionized atom will then fill the hole with another electron coming from an outer shell which will need to lose energy in order to adjust itself to a lower level. The way this electron loses a portion of its energy can be by emitting a photon of light which will carry the same amount of energy as the difference between the starting shell and the final one. This energy is usually in the range of X-rays, therefore between 0.1 and 60 keV. These X-rays are characteristics because the distance between one shell and another is fixed and unique to the atom. The bremsstrahlung X-rays, on the other hand, are the result of electrons being decelerated by the interaction with the atomic nucleus (Coulomb interaction) and therefore they can lose any amount of energy, usually in a lower energy range with respect to characteristic X-rays. This energy is emitted in the form of continuous energy X-rays. Figure 3.6 schematically summarizes the creation of characteristic X-rays and Bremsstrahlung radiation.

In order to chemically quantify the atomic species in the specimen, a standard sample of known composition $C_{(i)}$ has to be used in order to compare the measured intensity $I_{(i)}$ emerging from this specimen and the one from the actual specimen I_i. Castaing proposed that concentration and intensity of standard and unknown sample follow the formula

$$\frac{C_i}{C_{(i)}} = K \frac{I_i}{I_{(i)}} \tag{3.15}$$
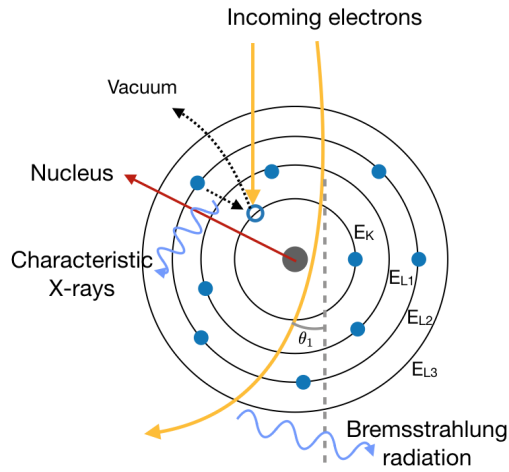
Figure 3.6: Schematic of the Bohr atomic model. When a primary beam electron penetrates to the inner shells of the specimen atoms, it has enough energy to ionize it, ejecting one of the core electrons. An outer shell electron will therefore lose its energy in order to fill the hole left by the ejected electron. In order to be adjusted in a lower energy state, the electron has to lose some of its energy, emitting it in the form of an X-ray. The shells are named with letters that indicate their position. Incoming electrons that do not hit an electron of the electron cloud have non zero probability of being decelerated by the coulombic interaction, emitting a continuous radiation (Bremsstrahlung).

where K is a sensitivity factor that accounts for the difference between the generated and measured X-ray intensity. Correction factors compensating from different physical phenomena taking place during the emission of X rays have to be included into K. In order to take into account the difference between the generated and the measured X-rays, three correction factors are considered. The effects that decrease the amount of measured X-rays with respect to the generated ones are called *matrix effects*. These effects arise because of the propagation of X-rays into the specimen when they travel towards the detectors. The main factors are those due to the atomic number Z_i, to the X-ray absorption A_i and X-ray fluorescence F_i. The Z correction takes into account the effect of atomic number on the excitation efficiency, fluorescent yield and also the detector efficiency. The second factor is the so-called absorption effect. Once an X-ray is generated, it has a non zero probability to be absorbed by the sample itself before being detected because of the photoelectric effect. X-rays generated deeper in the specimen will have a greater probability to be absorbed by the matrix. The A correction takes into account this effect. The third and last factor is the fluorescence effect. The photoelectric absorption mentioned earlier can result in the ionization of the inner atomic shells of another species in the specimen and therefore this ionization can cause the generation of characteristic x-rays. This is taken into account by the relative correction F. This correction method is usually referred to as the ZAF correction. Only the Z correction is considered in the case of an electron transparent sample. The Cliff-Lorimer technique is a way to use the relation 3.15 but without using a standard sample, so that, if one sample is composed by two elements, one can write

$$
\frac{C_A}{C_B} = K_{AB} \frac{I_A}{I_B}. \tag{3.16}
$$

It is sufficient then to link C_A and C_B and the previous equation can be solved. If the sample is only made out of the two elements A and B, the relationship is $C_A + C_B = 100\%$. K_{AB} factors are determined theoretically or experimentally and they depend on parameters such as the ionization cross-section, the fluorescence yield, detector efficiency and other microscope parameters. These factors are already integrated in the EDX quantification software, which in the case of present work was Bruker Esprit.

In our case, the TEM microscope used for the micro-analysis was equipped with a ChemiStem SuperX detector [109], with four silicon drift detectors arranged around the sample position to maximize the total amount of X-rays detected (scheme in Figure 3.7) and allowing a detection angle of 0.9 sr.
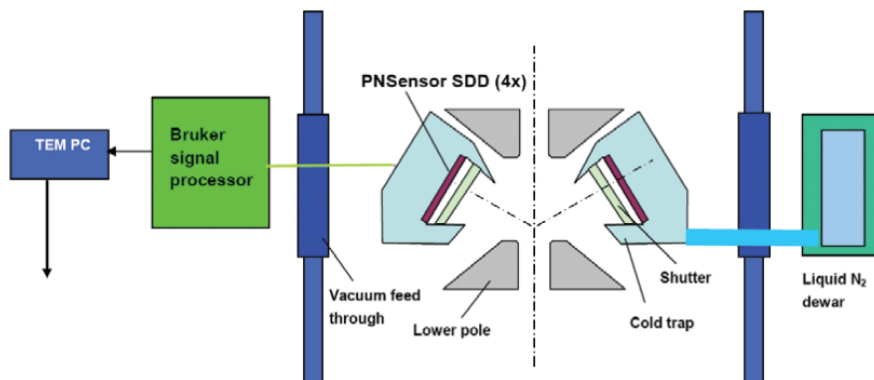
Figure 3.7: FEI ChemiStem detector for micro chemical analysis showing the SuperX geometry, with a schematic representation of two of the four detectors integrated around the sample (image from Schlossmacher *et al.* [109]).

3.4.4   Sample preparation for TEM observations

Before being suitable for TEM observation, a bulk sample has to be submitted to a preparation step that transforms the physical dimensions of the samples into suitable dimensions for the sample holder to be inserted in a transmission microscope. Typical dimensions for a TEM electron transparent lamella can vary but are around 3 µm by 5 µm with a thickness that can vary around 100 nm and lower.

Focused ion beam (FIB) is the the technique which was mainly used for the preparation of TEM samples. It involves the use of a scanning electron microscope (SEM) equipped with a second column with a gallium ions source. These gallium ions are used to mill part of the bulk sample, extract a lamella and thin it down to electron transparency. Prior to mill the bulk sample with the gallium ions, a carbon coating step is needed in order to protect the top surface from any milling damage and to reduce charging effects. This coating can be done in a separated carbon evaporator and/or directly in the FIB, which is equipped with a gas injector that deposits the desired material (carbon in this case) on top of the sample. Usually both depositions, outside and inside the FIB are needed to efficiently protect the sample surface. The advantage of using the FIB is that the sample can be imaged while being cut, so the cut itself is more controlled than during the conventional mechanical polishing technique and the dimensions can be checked constantly. Moreover, no additional steps are needed afterwards. Once the sample is in the FIB, the following procedure is applied:

- the region of interest is marked and a coating of carbon is deposited using the electron source;

- another carbon coating is applied this time using the gallium source as a catalizer. In total a thickness between $1\,\mu m$ and $2\,\mu m$ of carbon is deposited on the top surface of the sample (Fig. 3.8 (a));

- three trapezoidal holes are dug around the region of interest, leaving the sides exposed to the gallium ions. These holes are around $10\,\mu m$ deep (Fig. 3.8 (b));

- by adjusting the tilt angle of the sample, an undercut is performed and a micro-manipulator is brought to one side of the sample in order to attach it to the sample itself and then extract it from the bulk;

- the micro-manipulator is connected to the sample using carbon deposition and the last cut is performed. The bulk part of the sample is removed (Fig. 3.8 (c));

- the thick lamella is attached to the copper grid which serves as a support (Fig. 3.8 (d)). To thin it down, an average angle of $\pm\,1.4°$ is used for the forward and backward faces;

- the lamella is finally thinned down to a thickness of about $100\,nm$, using a final voltage of $5\,kV$ and a current of $80\,pA$, with a tilt included between $\pm\,6°$ for the forward and backward faces of the lamella (Fig. 3.8 (e)).

The FIB used for this work was a Zeiss NVision 40 CrossBeam with a Schottky field emission gun (FEG) that can be operated between $0.1\,kV$ and $30\,kV$ and a liquid the gallium source.

3.5   Differential Scanning Calorimetry

Differential Scanning Calorimetry (DSC) is a thermoanalytical technique that enables to monitor the structural transformations of a material depending on temperature. It is a technique widely used to observe glass transitions [110] and structural relaxation [111] among others [112] [113]. The technique is based on the measurement of the amount of heat needed to increase the temperature of a sample and of a reference of known heat capacity using two separated crucibles. Phase transitions will be either endothermic or exothermic, meaning that additional heat will have to be provided or extracted from the sample to maintain its temperature as that of the reference. The convention adopted here was to use the heat flow divided by the sample mass in y-axis (mW/mg).
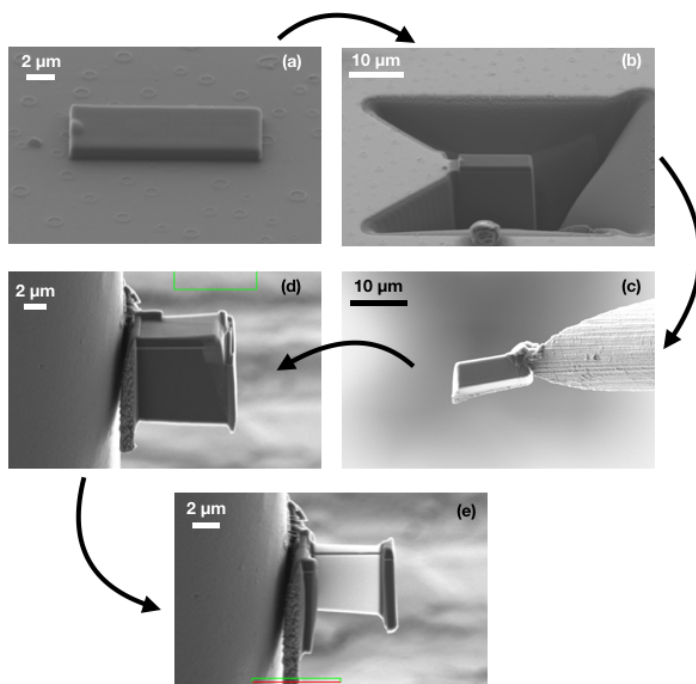
Figure 3.8: SEM views of the sample preparation steps by FIB. (a) carbon coating of the region of interest, (b) trapezoidal cuts and lamella, (c) lamella attached to the micro-manipulator, (d) lamella attached to the support grid and ready to be milled, (e) electron transparent lamella with the bright part indicating the thin area.

The crucibles are made of alumina (Al_2O_3), since they have to sustain high temperatures without melting or undergoing phase transitions. The experiments can be conducted in different atmospheres and using different heating rates. The studied samples were analyzed during both the heating phase and the cooling phase. This strategy allows to understand whether the structural and chemical transitions are reversible or not in the measured materials. All the analysis were done in a Netzsch DSC 404 C Pegasus instrument where the heating and cooling rate can be adjusted. The goal was to keep the same heating rate as the one used during the *in situ* XRD in order to have one common heating rate for all the different experiments. Preliminary tests were nevertheless conducted with slight different conditions in order to quickly check if any signal was registered. In the following list a complete specification of DSC experiments is presented:

- complete cycle - argon flux ($50\,\mathrm{ml\,min^{-1}}$) - $10\,^\circ\mathrm{C\,min^{-1}}$ - $600\,^\circ\mathrm{C}$
- complete cycle - argon flux ($50\,\mathrm{ml\,min^{-1}}$) - $10\,^\circ\mathrm{C\,min^{-1}}$ - $800\,^\circ\mathrm{C}$
- complete cycle - air atmosphere - $5\,^\circ\mathrm{C\,min^{-1}}$ - $700\,^\circ\mathrm{C}$
- complete cycle - air atmosphere - $5\,^\circ\mathrm{C\,min^{-1}}$ - $800\,^\circ\mathrm{C}$
- complete cycle - air atmosphere - $5\,^\circ\mathrm{C\,min^{-1}}$ - $400\,^\circ\mathrm{C}$

where a complete cycle is composed by the heating plus cooling step, both of them done with the same temperature rate. It is then indicated if any specific gas flow was introduced in the chamber, the temperature rate and the final temperature are also indicated. The reason why certain temperatures were chosen among others is that the experiment had to be stopped either before or after the crystallization. Before every measurement with the actual sample, a calibration was conducted, with the reference crucible and the one supposed to contain the sample, both empty. The obtained curves were automatically subtracted from the the experimental ones, so that the results shown in the dedicated section are already presented without background.

Sample preparation DSC is a technique meant to be used on bulk samples, whereas the samples studied in this work are in the form of a thin film. The main issue in applying this technique to thin films is related to the minimum mass of sample that has to be analyzed, which needs to be between $1\,\mathrm{mg}$ to $10\,\mathrm{mg}$ of material. With an average thickness for the ZTO of $150\,\mathrm{nm}$, it would be necessary to deposit as much as $10^4\,\mathrm{cm^2}$ to $10^5\,\mathrm{cm^2}$ in order to have between $1\,\mathrm{mg}$ and $10\,\mathrm{mg}$ of ZTO, the material density being around $6\,\mathrm{g\,cm^{-3}}$. In practice, the samples are always deposited on an average substrate surface of $2.25\,\mathrm{cm^2}$. Increasing the film thickness in a single deposition is not possible as the material

tends to crystallize from a threshold thickness and therefore presents two phases (amorphous and crystalline) simultaneously, which is not representative of the studied films. This topic will be further explained in chapter 4. For the DSC to reveal a change in the sample structure in the temperature range in which we were interested, it was crucial for the sample to stay in its amorphous phase. It was therefore decided to deposit several thin layers (150 nm each) of ZTO one on top of the other (for a total thickness of about 450 nm) with an in between-step of ten minutes during which the sample is taken out of the deposition system and exposed to air so that any strain or stress within the structure could relax before starting the following deposition. This method successfully led to an overall thick and amorphous material.

If a thin film sample is deposited on a bulk substrate and analyzed in a standard DSC equipment, the majority of the signal will come from the substrate, in other words, the substrate signal would completely mask the signal related to the actual sample. In order prevent the substrate signal to mask the thin film one, a free-standing sample was necessary (meaning that the sample had to be detached from its substrate). The common strategy was to proceed to a lift off of the ZTO in order to separate it from the substrate, using a liquid solution and then filtering the ZTO from the solution itself. After an extensive literature research, three main approaches were tried.

A ~ 300 nm of material was deposited on top of a specific photoresist (LOR) which was spin coated onto a silicon wafer [114]. A lift off step was conducted in a TMAH solution. The solution dissolved, together with the LOR, a portion of the silicon wafer and the result was a mixed powder containing ZTO mixed with silicon particles.

Another attempt was to deposit ~ 300 nm of material on top of a salt substrate, which was then dissolved in water and the floating flakes of ZTO was filtered using a special filter paper. Despite being more reliable than the first method, the resulting material was a lot contaminated by the salt, which remains dispersed in the water solution.

Finally ~ 450 nm of material was deposited onto a flexible mica substrate previously coated with a thin layer of carbon. The lift off was conducted in water, where the carbon detaches from the mica, resulting in a compact film of carbon plus ZTO floating at the surface of the solution. This method was the more efficient and the one employed in the DSC samples preparation. Figure 3.9 summarizes the main steps to gather the final ZTO flakes after the lift off procedure. The fact that few nanometers of carbon remains attached to the ZTO does not affect the measurement (thicknesses are not comparable), moreover an additional step of plasma cleaning was implemented in order to remove the majority of carbon prior to measurements.
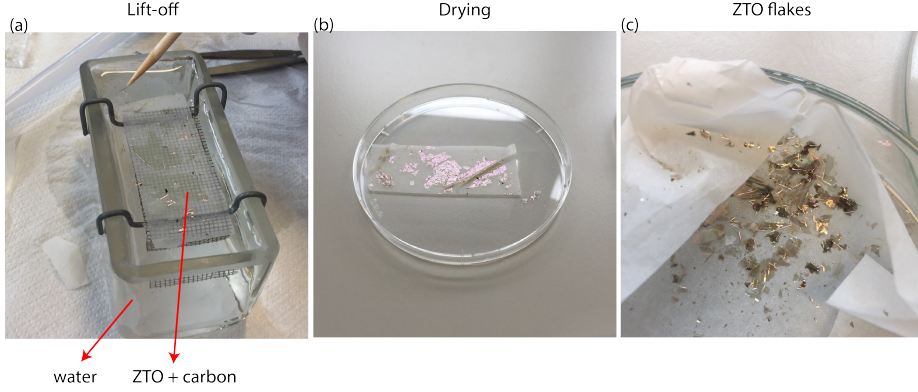
Figure 3.9: (a) Lift off procedure of a multi-layer of ZTO deposited on top of a mica substrate using water. The material is deposited onto a filter paper and let dry in air (b) before obtaining the flakes pictured in (c) and ready for the DSC analysis.

3.6 Electron Paramagnetic Resonance

In the attempt to shine light onto the defect analysis of our TCOs, electron paramagnetic resonance (EPR) experiments were carried out. EPR is a technique that allows to detect paramagnetic defects in a material. For a species to be paramagnetic, it has to have one un-paired electron in its outer shell. This characteristic is usually an indication of a defect in a material which would otherwise have a complete shell. The nature of the defects will be analyzed in the dedicated chapter.

The detection of these defects is based on the interaction between an external magnetic field B_0 and the unpaired electron, the quantum mechanics Zeeman effect. This interaction occurs because the unpaired electron has a magnetic moment μ, which spins around an external magnetic field. Because energies are quantized, an electron has two allowed states: one of lower energy where μ is aligned with the external field and another of higher energy with μ aligned against the magnetic field. The projection of the electron's magnetic moment on the direction of the external field can therefore assume the values $m_s = -1/2$ for the parallel state and $m_s = +1/2$ for the anti-parallel state. The energy difference between these two states is

$$\Delta E = g\mu_B B_0 \Delta m_s = g\mu_B B_0 \tag{3.17}$$

where g is the g-factor, $\mu_B = e\hbar/2m_e$ is the Bohr magneton and $\Delta m_s = \pm 1$. The needed energy to transition from one state to the other (parallel to anti-parallel or vice versa) is ΔE. In Figure 3.10 a scheme helps to visualize the process. When an external magnetic field is applied to the system, the two
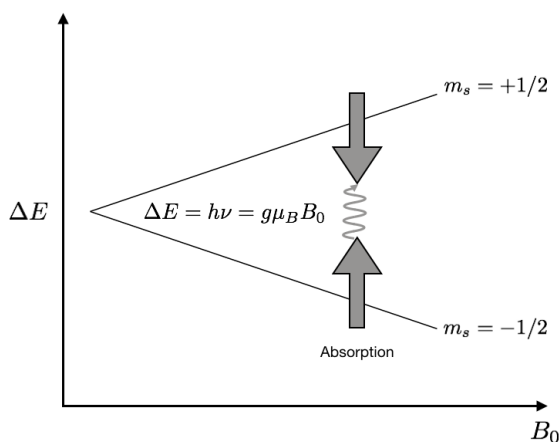
Figure 3.10: Scanning a magnetic field to a system containing unpaired electrons results in the splitting of the two possible spin states. When an electromagnetic radiation is then applied to the system, a transition from one spin state to the other can be observed. This signal is associated to a unique g-factor, fingerprint of the compound.

spin states have different energies that diverge linearly as the magnetic field increases. In these conditions, if an external electromagnetic wave is applied, this wave has a non-zero probability of enabling the transition from one spin state to the opposite one. This transition is usually referred to as an absorption because there are statistically more electrons with spin associated to a lower energy state than electrons with a higher energy state. The absorption occurs only when the magnetic field creates an energy difference between the two spin states equal to the radiation energy. There are two ways to produce this absorption, one is to keep the magnetic field constant and scanning the electromagnetic wave frequency or to keep constant the frequency and scanning the magnetic field. Most EPR spectrometers work by keeping the electromagnetic wave constant (usually microwaves) and scanning the magnetic field. The g-factor is independent of the microwave frequency and is therefore a fingerprint of the analyzed compound or element or defect. As a reference, the g-factor of a free electron is $g = 2.0023$. Variations from this value can indicate that the electron sits in a different environment with respect to the free electron.

The intensity of EPR signal is proportional to the concentration of unpaired electrons in the sample. In Appendix is presented a detailed explanation on how the EPR signal is acquired. The intensity I also depends on the microwaves

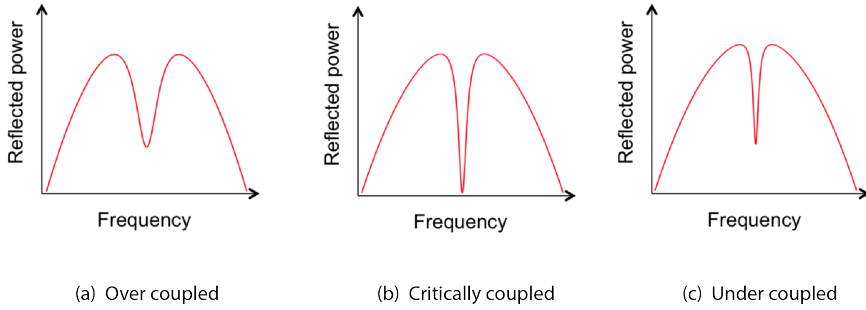(a) Over coupled   (b) Critically coupled   (c) Under coupled

Figure 3.11: Possible conditions of *coupling* between the cavity and the sample. The desirable situation is the one depicted in (b) where the power is not reflected. To tune the power, the sample has to be carefully positioned inside the resonator.

power P as follows

$$I \propto \sqrt{P}. \tag{3.18}$$

In order to increase the detected signal, the sample is inserted in a cylindrical cavity, the *resonator*, which is fundamental to amplify the signal coming from the sample. For the microwaves to be in resonance with the cavity means that the cavity "stores" the microwave energy and that microwaves stay inside it (there is a standing wave inside the cavity). Cavities are characterized by the Q-value which is defined as follows

$$Q = \frac{2\pi \cdot \text{energy stored}}{\text{energy dissipated per cycle}} \tag{3.19}$$

and is an indication of how well the microwaves are stored inside the resonator. Energy can be also dissipated because the microwaves generate a current in the cavity walls, which is dissipated under the form of heat. These concepts will be useful in the analysis of the EPR results.

Before starting the measurements, the cavity (or resonator) has to be *critically coupled* with the source, in order for the power to not be reflected. Therefore a pre-measurement fine tuning is needed. In Figure 3.11 the optimum shape of the reflected power is shown. It is fundamental to notice that the electrical conductivity of the sample interferes with the coupling to the cavity, resulting in a complicated process before the measurement itself. The goal is to obtain the condition shown in Figure 3.11 (b) before starting the measurement.

More information about the species or defects can be found analyzing the hyperfine interactions between the nuclei of the atoms and the electrons. The

nuclei can often have a magnetic moment that interacts with the magnetic moment of electrons. Registering this signals brings information about the sample such as the number of atoms composing a molecule. Moreover, if the unpaired electrons are embedded in an environment such as a molecule or a crystal, the electron spins might interact with the local magnetic field generated by the molecule or the crystal resulting in a non-isotropic g-factor. When anisotropy is present in the g-factor, three different values will be recorded for the three components of g g_x, g_y and g_z.

The EPR measurements were conducted in collaboration with the Institut für Experimentalphysik of the Freie Univerität in Berlin, using the so-called *continuous wave* EPR, where the frequency of the microwave is kept constant and the magnetic field varies. In particular the spectrum of the X-band was investigated, meaning that the microwave frequency is around 9 GHz, therefore, the expected transition for a free electron sits around a magnetic field of 332.1 mT. The specific equipment is a home-built X-band EPR spectrometer. The magnetic field was regulated by a field controller (Bruker BH15), and a microwave bridge (Bruker ER 048 R) was used for microwave generation and detection. Magnetic-field modulation in combination with lock-in detection was employed using a lockin amplifier (Stanford Research SR810) and a modulation amplifier (Wangine WPA-120), resulting in derivative spectra. The sample was placed in a Bruker ER 4122 SHQ microwave resonator. The quality factor Q of the resonator loaded with the sample was determined from the mode picture before each EPR measurement was started. The measured derivative spectra were background-corrected and double integration was performed to obtain the integrated EPR signal amplitude. This intensity was compared to the double integrated intensity of a reference sample with a known number of spins (4-Hydroxy-TEMPO dissolved in toluene). Taking into account Q, as measured for the respective sample, and all experimental parameters that influence the signal intensity, this comparison yields the absolute number of spins [115].

EPR measurements were performed on both free standing films and thin films deposited on dedicated quartz substrate that allowed to control exactly the amount of material deposited on top of it. Using this last method, quantitative calculations on the amount of defects contained in each sample were performed. In both cases, the sample is inserted in a narrow quartz tube which is then inserted in the resonator. In addition to the determination of *g-values*, EPR measurements allow to count the actual number of defects in the sample starting from the recorded signal. In order to enhance the signal-to-noise ratio in continuous wave EPR, the magnetic field is modulated to use a lockin detection. This field modulation leads to the first derivative of the absorptive EPR transition. For the quantitative evaluation of EPR signals one can use the following procedure:

- a background correction is performed and a double integral of the signal is calculated to obtain the total amount of signal intensity;

- the quality factor, Q, of the system is determined in parallel;

- the system is calibrated with a reference sample with a known spin count. This gives the machine transfer factor;

- all the parameters are plugged into the following formula and the absolute number of spins is therefore determined:

$$N = \frac{I}{C_f \left(\sqrt{P_m} B_{\mathrm{mod}} Q n_B S \left(S + 1 \right) \right)} \tag{3.20}$$

where I is the double integral, C_f the calibration factor, P_m the microwave power, B_{mod} the field modulation strength, n_B the Boltzmann population difference for a spin state equilibrium at a certain temperature and microwave frequency, Q the quality factor of the cavity and $S = 1/2$ for a doublet state [115] [116].

Tin-based Transparent Conductive Oxides

4.1 Introduction

In the context of studying structural and electrical properties of tin based TCOs and make a link between them, a systematic study was conducted on tin dioxide and further on zinc tin oxide. Both materials were submitted to thermal treatments up to high temperature and in different atmospheres and were investigated using some of the methods described in the dedicated chapter such as X-ray diffraction (XRD), transmission electron microscopy (TEM), UV-VIS-IR optical properties and standard Hall effect.

The first section of this chapter presents in depth investigation of the structural mechanisms happening in tin dioxide and make a link with its electrical properties, the discussion being based on the existing literature on tin dioxide. These analysis are fundamental in order to better understand what parameters are able to control the properties of the material and eventually being able to intervene on these parameters to improve the quality of the oxide. The electrical properties with respect to the annealing temperature are introduced, followed by the structural properties (XRD, TEM) and finally a route to enhance the material properties are suggested.

The second part of this chapter details the introduction of zinc (in low concentration) to the tin dioxide matrix and the effect of high temperature treatments in different atmospheres. Structural properties investigated by XRD and TEM are linked to the optical and electrical properties and additional techniques, such as thermal desorption spectroscopy, are used to investigate specific effects. A combination of EDX and Rutherford backscattering (RBS) is used to have a precise insight on the material chemistry. The link between opto-electronic properties and DFT simulations is discussed and helps to corroborate the experimental results. Finally, a summary on the properties of zinc tin oxide is presented and used as a starting point for the further investigations that are presented in the following chapters.

4.2   Electrical properties of Tin dioxide

The electrical properties of tin dioxide after various annealing were investigated at room temperature in order to understand if there is any dependence of the electrical conductivity on high temperature treatments. The latter were mainly conducted *in situ* in the XRD, in order to simultaneously acquire the temperature and structural information, some of the samples were annealed *ex situ* on a hot plate. In the following analysis the annealing method will be always specified. The thermal treatments were conducted in two different atmospheres, air and vacuum ($\simeq 10^{-4}$ mbar). The goal of conducting experiments with different pressures was to understand the role of atmosphere into the transport and structural properties of tin-based TCOs.

In order to track the evolution of the structure, tin dioxide samples were deposited on top of undoped silicon substrates, which are known to be highly stable upon thermal treatments and no interaction or mixed phase between the material and the substrate was observed. To ensure the deposition of amorphous SnO_2, a ~ 120 nm-thick material was deposited in three separated runs, during each one, 40 nm of material were deposited and extracted from the deposition system, exposed to air for few minutes and then re-introduced in the system for the second round. This method prevents the material to crystallize. The reasons behind will be explained in the paragraph dedicated to the structural properties.

Figure 4.1 illustrates the carrier concentration and mobility of tin dioxide samples annealed in air and in vacuum up to a maximum temperature of 500 °C in air and 700 °C in vacuum. The starting material (as deposited state) exhibits a carrier concentration of $\sim 9 \times 10^{19}$ cm^{-3} and a mobility of ~ 22 cm V^{-1} s^{-1} for a conductivity of ~ 316 S cm^{-1}. When annealed in air at 300 °C its carrier concentration (dashed blue line) starts to decrease to 6.6×10^{19} cm^{-3} and
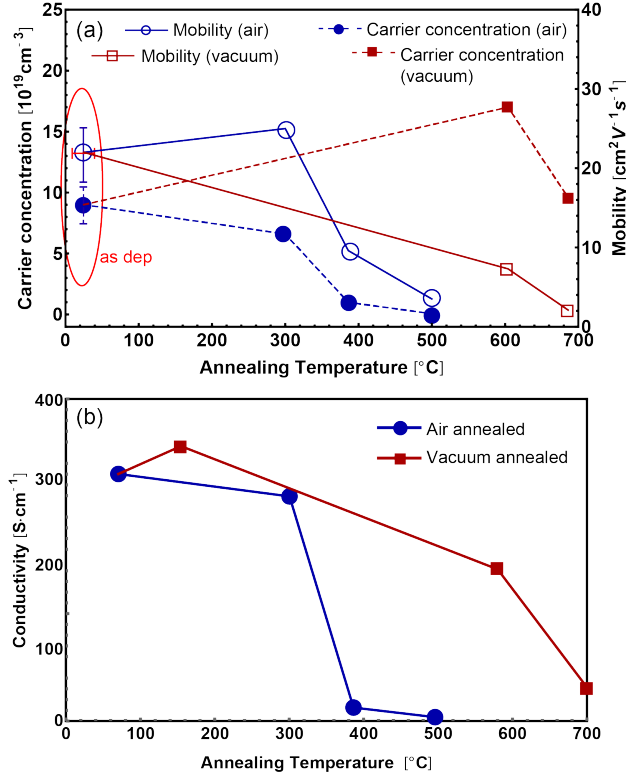
Figure 4.1: Mobility and carrier concentration (a) of SnO_2 samples annealed in air (blue lines) and in vacuum (red lines). The red circle highlights the as deposited samples. The drop in electrical properties differs by $\sim$200 °C between air and vacuum annealing. In (b) is shown the relative electrical conductivity for air and vacuum annealed samples. All samples were sputtered using a deposition temperature of 60 °C.

then to 1×10^{19} cm^{-3} at 386 °C and finally to 7×10^{17} cm^{-3} at 500 °C. The mobility remains mainly constant at 300 °C (24.5 cm V^{-1} s^{-1}), to then decrease to 9.7 cm V^{-1} s^{-1} at 386 °C and 3.5 cm V^{-1} s^{-1} at 500 °C. On the other hand, samples annealed in vacuum register a slight increase in carrier concentration at 600 °C (17×10^{19} cm^{-3}), paired with a decrease in mobility (9 cm V^{-1} s^{-1}), then the samples become completely resistive and impossible to be measured at around 700 °C. The big drops in both mobility and carrier concentration occur already at around 380 °C in air and at 600 °C in vacuum. Nevertheless, it is still possible to measure the samples up to an annealing temperature of 500 °C in air and 700 °C in vacuum. The literature review on tin dioxide highlighted that the main source of carriers is oxygen vacancies [**?**] and that if the material is stoichiomeric, it is not conductive and behaves as a non degenerate semiconduc-

tor [57]. During annealing in air, oxygen is thought to enter into the structure and to passivate oxygen vacancies, causing the observed drop in carrier concentration. This hypothesis is confirmed by the fact that when annealed in air, SnO_2 shows a decrease in carrier concentration that occurs before than that occurring in vacuum (pressure of 10^{-4} mbar). In this latter case, less oxygen is available to passivate these vacancies in the TCO, *i.e.* passivation occurs later, postponing the drop in electrical properties.

As stated in the chapter dedicated to the state of the art of tin-based TCOs, the electrical properties of such materials strongly depend on many parameters such as the substrate temperature during deposition and more importantly on the oxygen partial pressure in the deposition chamber. Adjusting the amount of oxygen during deposition allows to tune the electrical properties of tin dioxide and in particular the amount of oxygen deficient sites that allow the addition of free electrons in CB. Nevertheless, the effect of structural relaxation on the electrical properties has remained elusive.

4.3   Structural properties of tin dioxide

In order to fully understand the graph in Figure 4.1, a structural analysis of the material is fundamental. In the following section a combined XRD and TEM study is conducted in order to make the link between electrical and structural properties.

4.3.1   Transmission Electron Microscopy

As a preliminary analysis, intended to investigate the as-deposited structure of tin dioxide, a single deposition-150 nm-thick SnO_2 was deposited on a silicon substrate (heated at 60 °C) and the cross-section observed by TEM. Figure 4.2 shows a clear contrast between the bottom part of the film and its upper part. The first 30 nm of material deposited on top of the substrate are clearly amorphous, whereas the material grown on top of these first layers is polycrystalline, with conical structures highlighted by the red lines in Figure 4.2 (a). The sample in Figure 4.2 was not submitted to heat treatments.

The conical-shaped crystals highlighted in the TEM images are known in literature and are common to many materials such as silicon. Teplin *et al.* [117] investigated this phenomenon and discovered that conical shapes appear when there is sparse nucleation into an isotropically grown material and the new seeds form a phase, which is able to grow faster with respect to the matrix phase.
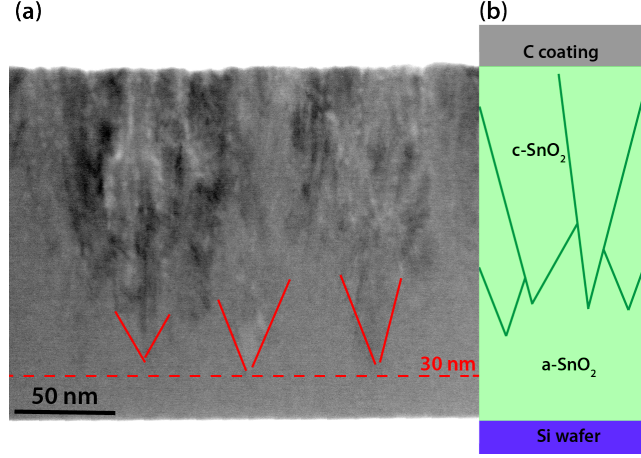
(a)

(b)

Figure 4.2: Cross-section (a) of a tin dioxide sample deposited on a silicon substrate and coated with carbon. The contrast difference between the bottom and top part is due to a phase change from amorphous to crystalline triggered by the material thickness. (b) Schematic representation of the sample with the co-existing phases.

These crystalline seeds can be created during the material deposition because of several factors such as local stress or strain, which would induce a certain probability to form crystalline arranged clusters of atoms rather than randomly arranged ones. Moreover, it is possible, starting from the measurements of the angles, to give an estimation of the ratio between the growth velocity of the amorphous phase with respect to the polycrystalline phase as follows:

$$\cos\theta = \frac{Z_0}{R} = \frac{v_a}{v_c} \tag{4.1}$$

where θ is the semi-angle of the cone, Z_0 the height of the cone, R its lateral side, v_a and v_c the growth rates of amorphous and poly-crystalline phases, respectively. From several TEM images (not shown) acquired on the cross-section of tin dioxide, the angle θ was extracted and the ratio between the growth rate of amorphous and crystalline phase was extracted. On average, being $\theta \simeq 30°$, it is found that the growth speed of the crystalline phase is 15% faster than the amorphous one. So, while the crystalline phase appears to be slow to nucleate, once the crystallization is triggered and the crystalline grains are formed this new phase is faster than the amorphous one. Figure 4.3 illustrates the scheme of this process. The explanation of this phenomenon resides in the competing growth on the planar surface of several crystalline seeds, so that the growth itself is restricted to a cone with a spherical cap. As Teplin *et al.* found out, the existence of the previously mentioned conical structures depends on the presence of crystalline seeds within the deposited material. The seeds can be observed in
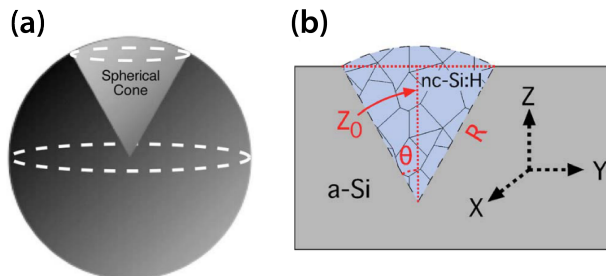
Figure 4.3: Schematic of the appearance of poly-crystalline cones within an amorphous matrix [117]. 3D representation (a) [118] and cross section (b).

the structure only when they have not developed yet into columnar crystalline grains, therefore was the main reason for a double observation, the top view and cross section one. An in depth study of the thickness with respect to the amorphous to crystalline amount of material was conducted on other TCOs too, in order to compare different materials and will be illustrated in the following chapters (and summarized in Chapter 6).

Taking into account these preliminary results and in order to investigate the structural properties of tin dioxide, three layers of 40 nm-thick each were deposited onto a TEM copper grid, for a total thickness of $\simeq 120$ nm; this deposition in three steps was chosen to maximize the chances of having an amorphous layer, according to the results just presented. Figure 4.4 summarizes the results obtained by TEM on the top view of tin dioxide. A bright field and two dark field images are shown to highlight that, in an overall amorphous material (as confirmed by the diffused rings on the diffraction pattern) there are few crystallites dispersed in the structure with an average diameter of $\simeq 20$ nm. These crystalline aggregations most probably act as nucleation seeds that trigger the phase change once the thickness reaches a threshold value.

4.3.2 X-ray Diffraction

Figure 4.5 shows the result of the *in situ* XRD experiments of SnO_2 samples annealed in air and vacuum atmosphere. The patterns were acquired every four minutes and the heating rate was kept at $5\,^\circ C\,min^{-1}$. Once the desired temperature was reached, the samples underwent a quenching step with a cooling rate of $50\,^\circ C\,min^{-1}$ and their microstructure was analyzed. In Figure 4.5 (a) the patterns show how the sample behaves when annealed in air, starting from room temperature up to $400\,^\circ C$. At a temperature of around $350\,^\circ C$, new peaks mark the appearance of crystalline phases, as highlighted by the appearance
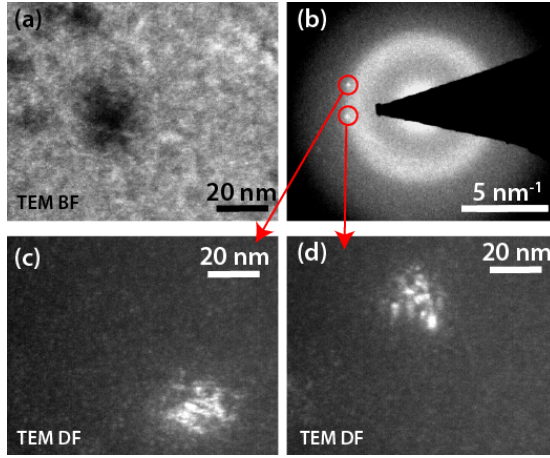
Figure 4.4: TEM top views (a), (c), (d) and diffraction pattern (b) of a tin dioxide sample deposited on a copper grid consisting of three layers of 40 nm each. Bright field image (a) with some diffraction contrast associated to a crystalline seed. (c) and (d) dark field images issuing from the analysis of the bright spots highlighted in the diffraction pattern (b). The DP corresponds to a mainly amorphous structure with few bright spots indicating the presence of small crystallites.

of the (101) and (200) reflections, in an otherwise amorphous material. This phenomenon is largely known in thermodynamics, since, transmitting energy (under the form of heat) to an amorphous material triggers the transition to the crystalline phase: the chemical bonds have enough energy to re-arrange themselves and reach a more stable energy configuration, which is the crystalline one. The peak at $\theta \simeq 33°$ comes from a forbidden reflection of the silicon substrate [119]. In Figure 4.5 (b) is shown the result of vacuum *in situ* annealing. The appearance of new peaks is, in this case, observed at around 604 °C where the reflections associated to (101) and (200)-SnO_2 appear. The amount of oxygen in the surrounding atmosphere has a clear influence on the crystallization temperature of the sample. More oxygen in the annealing atmosphere leads to a lower crystallization temperature, whereas when the atmosphere is oxygen deficient, the crystallization happens at higher temperature and after longer time. It indicates that oxygen is needed for the amorphous tin oxide to form the crystalline rutile structure. Moreover, there is a good adhesion between the sample and the platinum heating stripe, both in air and in vacuum, so the argument of a possible bad heat transfer between the stripe and the sample itself was discarded as a possible responsible for the late vacuum crystallization. Indeed, tin dioxide, as it is deposited, includes oxygen vacancies in its structure, this being the main reason why the material is actually conductive, as discussed in the previous section. The lack of oxygen during vacuum annealing delays
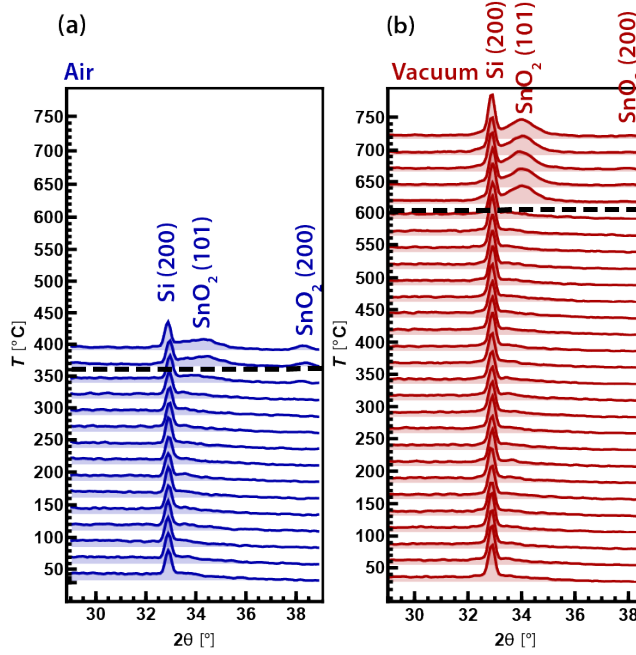
Figure 4.5: XRD patterns for tin dioxide annealed in air (a) and in vacuum (b). The black dashed lines indicate the temperature at which a phase change happens, marked by the appearance of new peaks associated to SnO_2. A shift of about $300\,^{\circ}C$ is observed between the two crystallization temperatures. The peak at $\theta \simeq 33^{\circ}$ is associated to the silicon substrate on top of which the samples are deposited.

the crystallization process, whereas annealing in air facilitates it. Kobayashi *et al.* reported that amorphous tin oxide starts to crystallize in vacuum at $450\,^{\circ}C$ forming SnO crystals and at higher temperatures ($550\,^{\circ}C$) forming SnO_2 crystals [120]. In their study, Kobayashi *et al.* documented the dependence of the crystal size on the thickness of the material. In the same study it is mentioned that crystallization is an abrupt phenomenon. This fact is confirmed by the present observations, indeed, the phase change happens within the acquisition of one XRD pattern. In our case neither XRD or EDX revealed evidences of the presence of SnO.

The drop in electrical properties of SnO_2 observed at $\sim 400\,^{\circ}C$ in air and $\sim 600\,^{\circ}C$ in vacuum is coincident with the phase change reported by the XRD experiments, suggesting that the crystalline phase is completely resistive and therefore unable to conduct electricity. On the other hand, many evidences of conductive crystalline and polycrystalline SnO_2 were found in literature [61] [10]. The main difference between what is reported in literature and the present re-

sults lies in the presence of dopants within the crystalline structure. Indeed, all the previously reviewed studies describe a crystalline SnO_2 material rich in dopants such as oxygen vacancies, which are fundamental for the electrical conductivity. The stoichiometric tin oxide structure is a non degenerate semiconductor and therefore not conductive. We hypothesize that after air annealing, oxygen enters the amorphous structure, passivating the oxygen vacancies, transforming the tin oxide into an insulating material. Once the stoichiometry is reached, the energy given with the heat treatment is sufficient to trigger the phase change of the material. The graph showing the electrical properties in Figure 4.1 suggests that the conductivity of SnO_2 starts to drop before the crystallization threshold is attained, indicating that most probably, oxygen entering the amorphous matrix passivates the oxygen vacancies and reduces the concentration of charge carriers in the CB. A similar behavior is observed in vacuum where, given the lower oxygen concentration, the passivation of vacancies and consequent drop of electrical properties occurs at higher temperatures.

From this preliminary analysis it can be concluded that starting from an amorphous SnO_2 and crystallizing it by using heat treatments causes a drop in electrical properties that makes the material unable to be used for any practical application. The combination of electrical measurements and structural investigation (XRD, TEM) allowed to discover that the actual drop in electrical conductivity is not caused by crystallization in the first place but rather by the passivation of defects (oxygen vacancies) that provokes a drop in carrier concentration. This was proven by the measurements done on vacuum annealed samples, were the drop in electrical properties is delayed by the late passivation of defects due to the lack of oxygen in the surrounding atmosphere. In this case, since the correct stoichiometry is reached at higher temperatures, the crystallization occurs later. Given this connection between drop of electrical properties and crystallization of SnO_2, the strategy was then to try to postpone the structural change to higher temperatures, in order to keep the material as much conductive as possible. Having a stable and conductive material even at higher temperatures would also allow tin oxide to be used in devices that need to work at higher temperatures, extending therefore the range of applications.

4.4 Increasing the material stability upon thermal treatments

As seen in the literature review, in order to postpone the crystallization and having a more resistant material to high temperatures, one strategy would be to increase the level of disorder of the amorphous matrix, adding another ion to a single oxide, transforming it in a double oxide. But not all elements are proven

to work as stabilizers upon thermal treatments. Zinc oxide is an element that, when inserted in the amorphous phase of a transparent oxide, is demonstrated to increase the energy barrier towards crystallization because some strain is introduced at the level of the atomic bonds and it might diminish the lattice thermal vibrations, delaying the crystallization [96]. In fact, as seen in Chapter 2, the addition of zinc in various TCOs, transforms them in more stable and conductive materials up to temperatures at which, with no zinc addition, the material is usually extremely resistive. Another study [121] reports on the effect of adding strain to a graphene sample that leads to an overall increase of the heat capacity, which is by definition, the ability of a material to absorb energy before increasing its temperature by one degree. The addition of strain in graphene is thought to soften the phonon modes, in other words, to decrease the thermal vibrations of the material itself. In the following sections the structural and electrical properties of tin dioxide with the addition of zinc into the amorphous matrix are studied and the results illustrated.

4.5 Zinc Tin Oxide

4.5.1 Electrical properties

In Chapter 3 are explained in details the deposition parameters used to fabricate the material analyzed in the following sections. As a reminder, the composition of the investigated ZTO is $Zn_{0.05}Sn_{0.30}O_{0.65}$.

As for tin dioxide experiments, samples were annealed *in situ* in the XRD in air and in vacuum (10^{-4} mbar). For these experiments, 150 nm of material were deposited on top of 1×1 cm silicon substrates in order to fit into the diffractometer heating chamber. The heating and cooling parameters were kept the same as for the tin dioxide annealing and the electrical properties of each sample were measured *ex situ* by standard Hall effect. Figure 4.6 shows the mobility and carrier concentration of ZTO samples annealed in air and vacuum. Three different regimes can be distinguished looking at the mobility and carrier concentration in air-annealed samples. From room temperature to $300\,^{\circ}\mathrm{C}$, carrier concentration increases from $\sim 7 \times 10^{19}\,\mathrm{cm^{-3}}$ to $\sim 12 \times 10^{19}\,\mathrm{cm^{-3}}$, whereas the mobility slightly increases from $\sim 20\,\mathrm{cm\,V^{-1}\,s^{-1}}$ to $\sim 27\,\mathrm{cm\,V^{-1}\,s^{-1}}$. The overall conductivity increases from $205\,\Omega^{-1}\,\mathrm{cm^{-1}}$ to $522\,\Omega^{-1}\,\mathrm{cm^{-1}}$. The enhanced carrier concentration might come from a slight structural relaxation giving rise to a release of donors from point defects already present within the structure [96], [122], [123]. This increased carrier concentration was also observed in samples that underwent annealing in nitrogen and hydrogen atmosphere [124], corroborating the hypothesis that this phenomenon is not linked
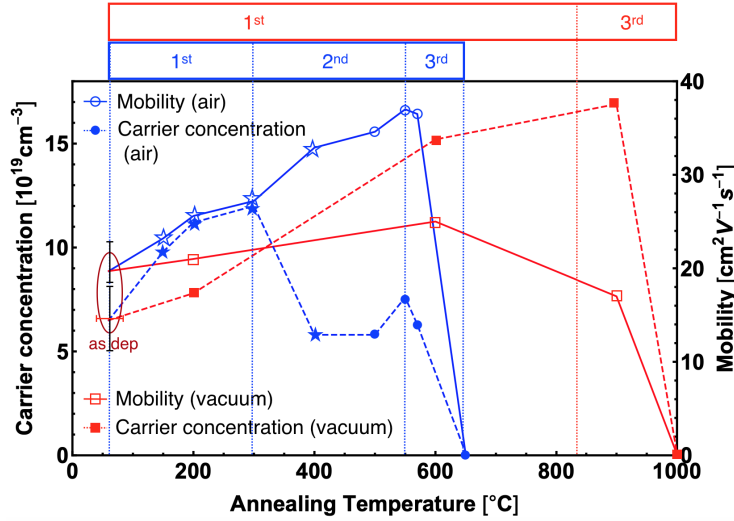
Figure 4.6: Carrier concentration (dashed lines) and mobility (solid lines) of ZTO films as a function of annealing temperature in two atmospheres: air and vacuum(10^{-4} mbar). In air, three different regimes, highlighted in the top blue rectangle, can be isolated depending on the temperature. An increase of both mobility and carrier concentration up to 300 °C, a drop of carrier concentration between 300 °C and 400 °C paired with a decrease of mobility and the final drop of both mobility and carrier concentration happening at 570 °C. In vacuum just two regimes, highlighted in the red rectangle, can be distinguished, an increase in electrical properties between room temperature and 650 °C before a final drop at 1050 °C. With stars are indicated the samples heated *ex situ* on a hotplate, whereas with circles and squares are indicated the samples annealed *in situ* in the XRD.

to the influence that the surrounding atmosphere might have. Increasing the carrier concentration results in a shift of the Fermi level to higher energies inside the conduction band and therefore far away from the localized defects that create potential barriers and that restrict the mobility [125], which would explain the simultaneous increase in mobility. Between 300 °C and 500 °C carrier concentration decreases from $\sim 12 \times 10^{19}\,\mathrm{cm}^{-3}$ down to $\sim 6 \times 10^{19}\,\mathrm{cm}^{-3}$, whereas the mobility increases further from $\sim 27\,\mathrm{cm\,V^{-1}\,s^{-1}}$ to $\sim 37\,\mathrm{cm\,V^{-1}\,s^{-1}}$. The consequence on the conductivity is a drop down to $306\,\Omega^{-1}\,\mathrm{cm}^{-1}$ (Figure 4.7). Similarly to what happens in SnO_2, this behavior is ascribed to a passivation of oxygen deficiencies when the annealing is performed in an oxygen rich atmosphere [124], with a consequent decrease of charged scattering centers. Having less scattering centers means being able to increase even more the mobility but on the other hand, causing a decrease in carrier concentration, which, as stated before, is mainly thought to be due to oxygen vacancies in these materials.
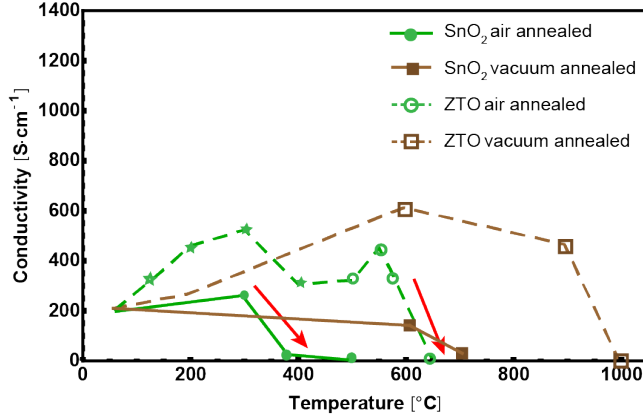
Figure 4.7: Electrical conductivity of SnO_2 and ZTO annealed in air and vacuum. Measurements were done using Hall Effect on the samples annealed *in situ* in the XRD and *ex situ* on a hot plate, the latter are represented with stars instead of circles. 5% addition of zinc in the SnO_2 network results in a more stable material upon thermal treatments, indeed the drop in conductivity in ZTO is delayed by $\sim 300\,°C$ with respect to SnO_2.

Other groups also reported that annealing TCOs in an oxygen-rich atmosphere leads to a decrease to electrical conductivity due to passivation of oxygen vacancies [126]. The third interval is represented by the highest temperatures and similarly to what happened to tin oxide, since the electrical conductivity decreases, the crystal is thought to contain a low defect concentration. In vacuum atmosphere, only two main trends can be distinguished: carrier concentration increases from the as deposited value to a maximum of $\sim 17 \times 10^{19}\,cm^{-3}$ at $\sim 900\,°C$ whereas the mobility stays almost constant ($\sim 17\,cm\,V^{-1}\,s^{-1}$), for an overall conductivity increase from the as deposited value ($200\,\Omega^{-1}\,cm^{-1}$) up to $612\,\Omega^{-1}\,cm^{-1}$. At the highest temperature, conductivity drastically decreases. This behavior fits with the previous explanation on the passivation of oxygen deficiencies, happening at higher temperatures in an oxygen poor atmosphere. As introduced before, the source of charge carriers of this class of materials is oxygen vacancies which, once ionized can donate one or more electrons to the conduction band [127] [128]. In addition, substitutional species can also donate electrons to the conduction band. It is important to notice that ionized impurity scattering centers in the lattice increase the probability for an electron to recombine, diminishing τ_e, defined as the time an electron can travel in CB before recombination, and therefore decreasing mobility [129].

Figure 4.7 compares the electrical conductivity of SnO_2 and ZTO when the annealing is conducted in air and in vacuum. Even if the two materials have similar as-deposited electrical properties, adding a small percentage of zinc into the

amorphous network of tin dioxide helps to keep the material more stable when submitted to thermal treatments, with good electrical properties maintained at higher temperatures. Having similar electrical properties at room temperature would mean that the addition of zinc would not be creating additional carriers in the tin dioxide matrix, but the fact that the drop of properties occur at higher temperatures would be the consequence of a built-in resistance of the material to high temperature treatments, thanks to the addition of zinc. To have a complete picture of the ZTO, the structural properties were investigated in details and presented in section 4.6.

4.5.2   Optical properties

As introduced in the description of the state of the art of TCOs and following the requirements of the specific application, a trade-off must be found between the enhanced electrical properties and the optical properties of the material. Increasing the charge carrier density N translates in an increased absorption in the infrared part of the spectrum. Moreover, in the attempt of doping the material in order to create more charge carriers, energy levels are created right above the valence band maximum or right below the conduction band minimum. These centers can act as recombination centers, shrink the optical band gap of the material and therefore deteriorate the optical properties in the visible range.

 In the context of all the optical measurements that were carried out on several ZTO samples, Photothermal Deflection Spectroscopy (PDS) spectra were acquired. Figure 4.8 shows the results for the samples annealed in air at 500 °C and 600 °C together with the as deposited sample. These measurements allow to calculate the optical band gap of materials by extracting the absorption coefficient and then using Tauc's relationship [130] [104]. For this calculation it was assumed that the optical transitions are allowed and direct. An obvious difference is highlighted in Figure 4.8 between the as deposited sample and samples annealed in air at 500 °C and 600 °C. The as deposited sample shows a broad sub-gap absorption centered at ∼2 eV, which disappears after the annealing at 500 °C. The calculated optical gap energy was $E_g^{opt} = 3.7$ eV for the sample annealed at 500 °C. This value was found to be in the same range as those in literature [99] [131] [132] (values between $E_g^{opt} = 3.35$eV and $E_g^{opt} = 3.89$eV). The difficulty in using such a method resides in the fact that all the energy levels below the conduction band minumum (CBM) could misrepresent the real value of bandgap. After annealing there is a clear reduction of the levels below the conduction band (either passivation or complete removal) which are responsible for the absorption of energies below the band gap. When going from an amorphous film (blue curve) to the annealed ones (red and green curves) the disorder into the material drastically diminishes, resulting in the removal of
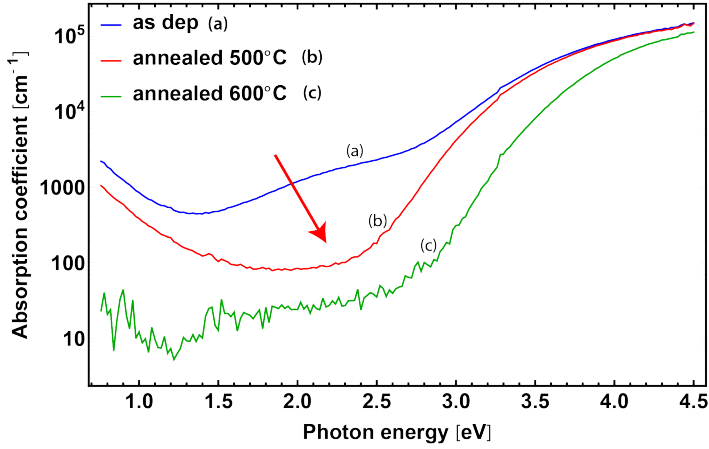
Figure 4.8: Photothermal deflection spectroscopy (PDS) measurements of three ZTO samples: as deposited, annealed in air at 500 °C and annealed in air at 600 °C.

subgap tails and consequent opening of the band gap [133]. Density Functional Theory (DFT) calculations were conducted and it was found that the Density of States (DOS) for 38 ZTO amorphous samples with different compositions (from stoichiometric to oxygen poor and with the addition of hydrogen) showed characteristic tails due to the local disorder of the amorphous structure. These tails are responsible for the shrinking of the optical band gap and they are removed once the samples undergo high temperature annealing. Figure 4.9 shows the effect of removing one oxygen atom from the structure and the calculations highlight the appearance of defect states located inside the band gap shifted towards the CBM. These states are the ones responsible for the optical absorption of the material towards the visible part of the spectrum. High temperature treatments help therefore to remove sub-gap states and hence improve optical transmission of the ZTO.

4.6 Structural properties

4.6.1 Thickness effects

In order to check if the thickness effect that was registered for SnO_2 during deposition, is also present in ZTO, i.e. a phase change from amorphous to crystalline driven by the material thickness, a 1 µm-thick ZTO layer was deposited on top of a glass substrate. Similarly to tin oxide, ZTO crystallizes after a cer-
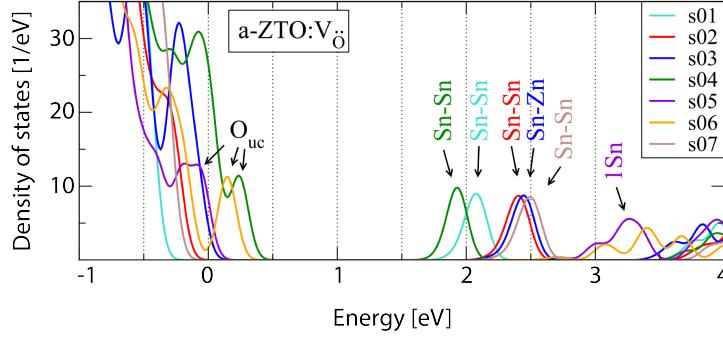
Figure 4.9: Densities of states of the 8 a-ZTO:$V_{\ddot{O}}$ samples that contain a local oxygen deficiency in the network. The deep levels inside the band gap are carried by one or two metal atoms (vicinity of CBM), whereas undercoordinated oxygen atoms are responsible for the levels close to the VBM. (Calculations conducted by Dr. Urban, (Fraunhofer Institute for Mechanics of Materials (IWM) [124])

tain thickness within which it exhibits amorphous characteristics. Figure 4.10 (a) shows a film cross-section that reveals that ZTO crystallizes after the first 150 nm of deposition, which is different with respect to tin oxide, that crystallizes after ~40 nm. This might be related to the fabrication conditions that follow the particular recipe used for deposition [117] (*e.g* oxygen concentration). Further analysis on the crystallization mechanisms will be presented in chapter 6. EDX characterization was conducted on the thick ZTO in order to verify if any difference in the chemistry is registered between the amorphous and the poly-crystalline phase. Figure 4.10 presents the EDX maps of tin, zinc and oxygen next to a STEM DF image of the thick ZTO. The EDX maps show no chemical separation between the amorphous and crystalline part of the sample. The growth speed was calculated as for tin dioxide using several cone angles extracted from TEM images and applying equation 4.1. Similar to the case of SnO_2, the crystalline phase is found to be faster in growing with respect to its amorphous counterpart. In particular, the ratio $v_{/}v_c \simeq 0.98$, attesting the crystalline phase a 2% faster than the amorphous one.

4.6.2 X-rays diffraction

In order to investigate the ZTO microstructure, *in situ* XRD experiments were performed with the same experimental parameters used for tin dioxide and in a scanning range comprised between 20° and 80°. Seven samples were annealed up to 200 °C, 550 °C, 570 °C, 600 °C, 650 °C, 750 °C, 1050 °C in air and four samples were heated in vacuum up to 200 °C, 600 °C, 900 °C and 1050 °C before the quench. Figure 4.11 shows the XRD patterns for both air and vacuum
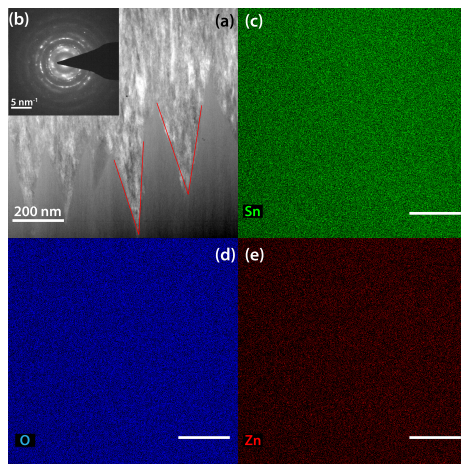
Figure 4.10: (a) STEM DF image of thick ZTO sample with (b) SAED taken from the upper part of the sample and EDX maps of tin (c), oxygen (d) and zinc (e). No segregation of elements or interface accumulation is visible from the chemical analysis, indicating that the chemistry of the material does not change from the amorphous to the crystalline portion of the sample.

annealing at their maximum temperature. The peak visible along the whole temperature range is related to a forbidden reflection of the silicon substrate [119]. The evident change of the structure happens at 570 °C in air and at 930 °C in vacuum, when new peaks associated to SnO_2 appear in the patterns. In detail, the reflections at $\theta \sim 34°$ and $\theta \sim 38°$ are associated to SnO_2 (101) and (200) reflections, respectively. These peaks indicate new crystalline phases that appear in the material, which goes from the amorphous to the crystalline phase. Figure 4.12 shows a comparison between the first pattern (acquired at room temperature) and the last one (acquired at 1050 °C in air). The low intensity signal appearing between $\theta = 28°$ and $\theta = 34°$ at room temperature arises from the short range order in the amorphous structure that is not anymore present at medium to large distances, since the structure is predominantly disordered [85]. This low intensity signal disappears once the crystallization occurs. In the acquired XRD patterns no crystalline phase associated to ZTO was found, most probably because the known crystalline phases of ZTO, such as Zn_2SnO_4 and $ZnSnO_3$ are associated to a different stoichiometry [134].

The main difference between air and vacuum annealing is the temperature at which the phase change occurs, i.e. the crystallization temperature T_C which is around 570 °C in air and around 950 °C in vacuum. Atmospheric oxygen seems therefore to play an essential role in the crystallization process, helping the formation of the rutile phase of tin dioxide. Despite the initial stoichiometry
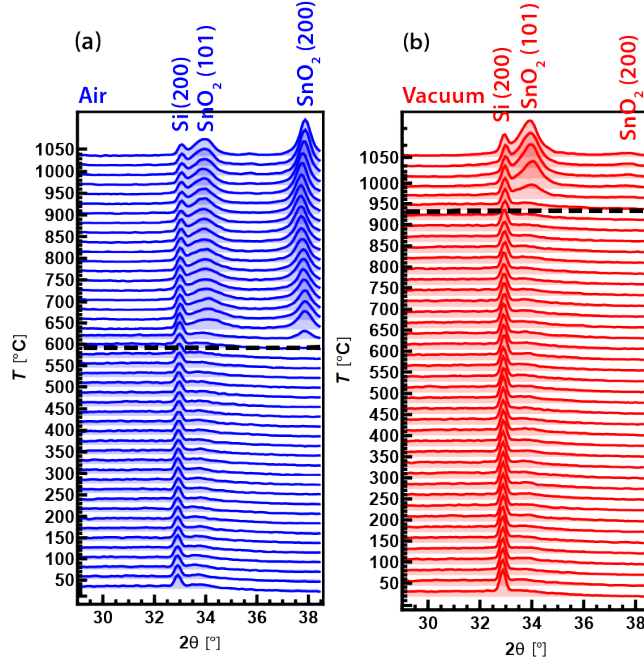
Figure 4.11: XRD patterns for ZTO annealed in air (a) and in vacuum (b). The black dashed lines indicate the temperature at which a phase change happens and it is marked by the appearance of new peaks associated to SnO_2. A shift of around $300\,°C$ is observed between the two crystallization temperatures. The peak appearing at $\theta \simeq 33°$ is associated to the silicon substrate on top of which the samples were deposited.

($Zn_5Sn_{30}O_{65}$) already rich in oxygen, oxygen vacancies are present in the film and these must be passivated to some extent before crystallization occurs. To reinforce this assumption, Rutherford Backscattering measurements (RBS) were conducted onto ZTO samples. This technique allows to measure the relative molar concentration of the selected material. The results are summarized in Table 4.1 It is clear that there is an increase in the relative concentration of oxygen during the air annealing with respect to the concentration of the as deposited sample. Contrary to the oxygen already present within the ZTO structure, this increased amount of oxygen might be directly available for the formation of the tin dioxide phase. These results lead to the proposition of a structure where the oxygen present into the as deposited ZTO might be "trapped" in a molecular form such as water and therefore not directly available for the formation of a new phase. To verify whether oxygen might be trapped in a molecular form within the ZTO and therefore not available to form crystalline SnO_2, Thermal Desorption Spectroscopy (TDS) experiments were conducted. This technique allows to measure the desorbed molecules from the sample while heating it.
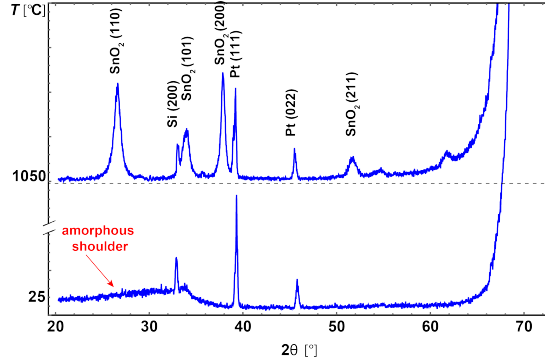
Figure 4.12: *In situ* XRD annealing in air of the first and last patterns, acquired at room temperature and 1050 °C respectively. The main peaks are indicated in the top part of the figure. The ones appearing since room temperature are associated to either the substrate (silicon) or the heating element (platinum).The low intensity signal highlighted by the red arrow represents the short range order within the material while in its amorphous phase. This order disappears as soon as the crystallization takes place.

Table 4.1: ZTO compositions from the Rutherford Backscattering measurements before and after annealing in air.

As deposited	$Zn_{0.049}Sn_{0.299}O_{0.652}$
Annealed at 500 °C	$Zn_{0.047}Sn_{0.289}O_{0.664}$

The sample is heated in high vacuum (1×10^{-10} mbar) up to 900 °C in a chamber connected to a mass spectrometer. In Figure 4.13 the relative amount of water and oxygen coming out of the ZTO sample during high vacuum annealing is illustrated. It is important to notice that the amount of water coming out of the sample can be water desorbed from the surface of the sample and not from the whole thickness of it. Nevertheless, these experiments corroborate the hypothesis that some of the oxygen atoms, although present within the ZTO matrix, might not be available to form the crystalline structure of tin dioxide, being occupied in bonds with hydrogen atoms in order to form water molecules. This might be the reason why in order to form stoichiometric SnO_2 more oxygen coming from the surrounding would be needed. The same effect was observed in tin dioxide alone.

Being the crystalline reflections in Figure 4.12 entirely related to SnO_2, it is clear that zinc does not influence the dimensions of the rutile unit cell of tin dioxide, whereas it increases the crystallization barrier towards higher energies. In order to understand if the addition of 5% of zinc in the amorphous ma-
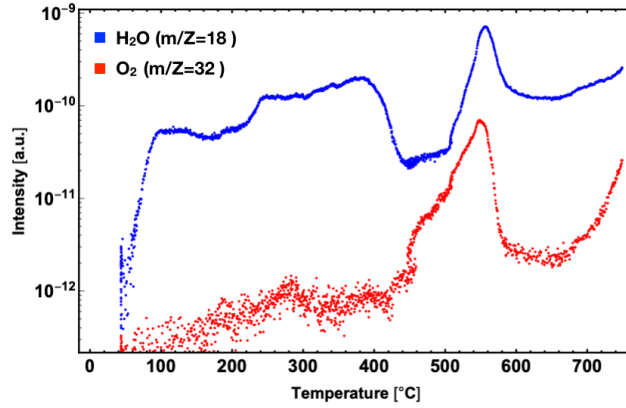
Figure 4.13: Water and oxygen released in the atmosphere through the ZTO surface during high vacuum annealing and measured by a mass spectrometer in TDS experiments. (TDS experiments were conducted by E. Rucavado at the Research Center for Photovoltaics (AIST, Japan))

trix of tin dioxide modifies the lattice parameters, a calculation of a and c was conducted. Starting from the position of the X-rays reflections, the lattice constants were calculated using the relations described in the experimental section of this thesis. Figure 4.14 shows the evolution of the lattice constants versus temperature. The theoretical lattice parameters of SnO_2 are $c = 0.4738$ nm and $a = 0.3187$ nm (taken from the JCPDS database) with a distortion factor $U = c/a = 1.4866$ [135]. The theoretical evolution of the lattice parameters with respect to temperature was not found in literature, instead, some experimental values are found, which highlight the fact that no clear trend can be extrapolated. Both a and c appear to vary differently with respect to the study [136]. Other available experimental data concern the lattice evolution with the pressure, which happens to shrink the unit cell [137] [30]. Therefore, the dashed red lines on the graph represent the values of a and c at room temperature. The mean of the experimental distortion factors is 1.458 ± 0.008, which is slightly lower than the theoretical value. The experimental value of c is only slightly smaller with respect to its theoretical value whereas a respects well its theoretical value. The addition of 5% of zinc into the tin dioxide matrix might be the reason why the measured lattice parameter c is 3% smaller than the theoretical one, being the zinc an element with smaller ionic radius with respect to the one of tin. No important variation throughout the annealing are reported from this calculation. Zhu *et al.* [96] reported that because of the difference in bond lengths between $Sn-O$ and $Zn-O$, there is a globally compressive strain in the ZTO network, which is confirmed by the slight shrinkage of c extracted from the XRD data. Furthermore, the ionic radius of Zn^{2+} is smaller (74 pm) than
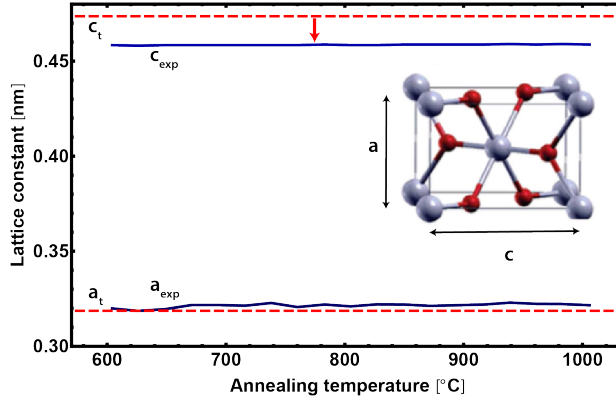
Figure 4.14: Experimental lattice constant a_{exp} and c_{exp} of the SnO_2 rutile structure with respect to the air annealing temperature. Red dashed lines indicate the correspondent theoretical values a_t and c_t.

the one of Sn^{2+} (118 pm), which reinforces the previous observations.

The intensities of the XRD reflections are, as formerly explained, a combination of different contributions, such as the scattering amplitude (which depends on the structure factor) and the number of unit cells with a particular crystal orientation. The theoretical intensities of the SnO_2 reflections are indicated in Figure 3.4 in the chapter dedicated to the experimental techniques. Comparing these intensities with the experimental ones in Figure 4.11(a) makes it immediately clear that the most intense ones in this graph do not correspond to the most intense ones in Figure 3.4. This can be an indication of which crystalline orientation is dominant within the material. The patterns in Figure 4.11(a) suggest that more unit cells with a (200)-orientation are present in the crystalline SnO_2. On the other hand, in Figure 4.11(b) the most intense reflection is the SnO_2-(101), whereas the (200) is very weak. There are some evidences in literature of such effects, in particular Deepu *et al.* [138] reported that by changing the oxygen flow during annealing, ZnO thin films exhibit different texture. Alaf *et al.* [139] reported that (211) preferred orientation increased as argon gas pressure increases during the deposition of tin. Martel *et al.* [140] compared different textures issuing from treatments done on SnO_2 in different atmospheres and hypothesized that the probability of one surface to be more stable than another one could influence the final texture of the material, reporting a varying ratio between (110), (101) and (211) orientations. In particular the amount of oxygen dispersed in the surrounding atmosphere would oxidize or reduce more one surface with respect to another, resulting in a different preferred orientation.

Fluorine doped tin oxide was also found to prefer a (200)-orientation [141]

which can depend on several parameters, such as substrate temperature during deposition, deposition rate [142], growth temperature [143] and annealing temperature [144]. Wang *et al.* reported that the (200) preferential orientation was also associated with an increase in electrical mobility. Korber *et al.* reported about the influence of surface energy minimization on the preferential orientation [145], and theoretical calculations were carried out for stoichiometric tin oxide. Unsaturated bonds along a direction would also make that direction favorable with respect to others [88]. Montero *et al.* highlighted the link between certain crystallographic orientations and the chemical properties of Sb-doped SnO_2, reporting a change in ionization potential related to the change in orientation from (101) to (110), linked to the amount of oxygen during the deposition [146]. It is clear that the amount of oxygen during annealing and deposition plays a fundamental role in the chemistry of the material. The debate is still open in literature for what concerns the way oxygen affects the formation of one orientation rather than others. Hypothesis were published on the probability of a certain crystallographic orientation to form more stable surfaces, as an example, (101) surface, being rich in Sn^{2+} atoms, would be more stable at low oxygen chemical potentials, whereas the (110), rich in Sn^{4+} atoms, would be more stable at high oxygen chemical potentials [10]. Batzill *et al.* calculated the more stable surfaces using several DFT calculations, not taking into account the chemisorbed oxygen from the environment, but just the lattice oxygen, showing that the (200) orientation, which is the most intense during air annealing, was not found during their calculations. This corroborates the thesis that in order to be present, this orientation has to be sustained by a strong oxygen activity, that is absent in vacuum annealing. However, in order to make a precise comparison, more vacuum data would be needed, but in our case, the highest temperature (1050 °C) was close to the maximum temperature attainable by the heating holder of the diffractometer. The comparison between the textures reported in literature and the ones found in the present work is arduous because of the amount of parameters that are completely different within the studies and that can all have an impact on the final texture of tin dioxide.

The crystallite size and peak intensity evolution of SnO_2 phase in ZTO were extracted from XRD patterns and tracked for air annealing, results are depicted in Figure 4.15. The intensity of the broad peak related to the amorphous shoulder decreases drastically after the crystallization temperature is reached, confirming the phase change from amorphous to crystalline. A small contribution of the amorphous phase remains nevertheless present and decreases gradually as the annealing temperature increases. At the same temperature threshold, crystalline SnO_2 reflections appear. The intensity of these peaks remain constant throughout the entire annealing process except from the (110) and (200) reflections that keep growing with increasing temperature. In terms of crystal dimension, having higher intensities translates in bigger crystal grains with that specific orientation, as shown in the experimental section dedicated to XRD.

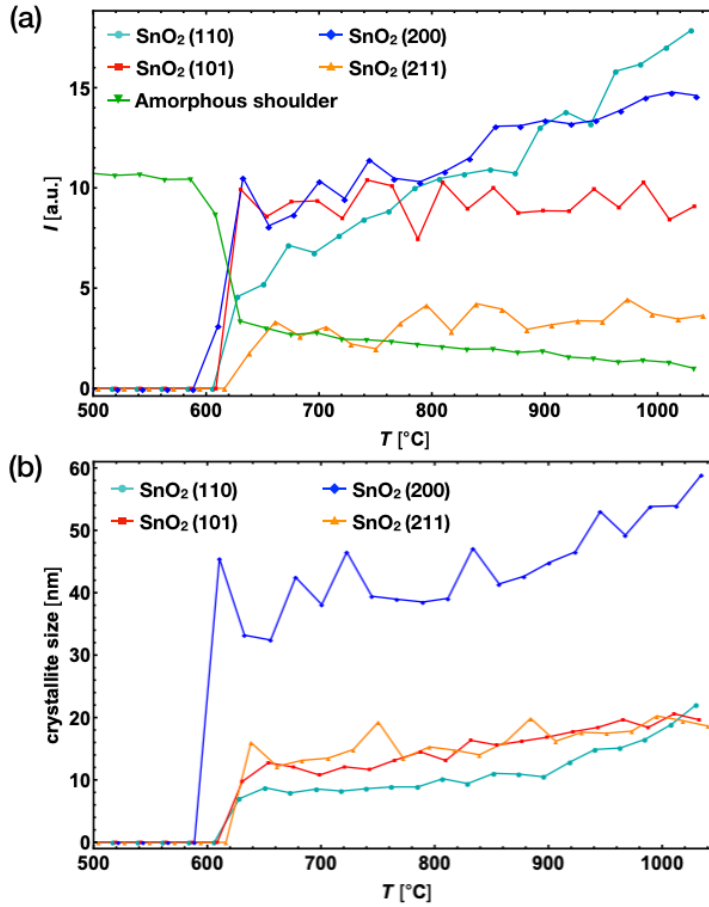**Figure 4.15:** Intensity of different crystal orientations appearing after the crystallization temperature (T_C) together with the amorphous shoulder intensity (a), which gradually disappears after T_C. In (b) the crystal sizes have been calculated, proving that especially (110), (101) and (200) orientation continue to grow with increasing annealing temperature. These calculations were carried out for air annealed ZTO samples.

4.6.3 Transmission electron microscopy

In order to confirm the results arising from XRD experiments and investigate locally the microstructure of samples annealed in different atmospheres and at different temperatures, an *ex situ* electron microscopy study was conducted. Figure 4.16 shows the selected area electron diffraction (SAED) and STEM HAADF images together with EDX maps and line profiles of zinc, for the ZTO samples annealed at 550 °C, 650 °C, 750 °C and 1050 °C in air. The sample annealed at 550 °C shows a dense and homogeneous structure, with no detectable diffraction contrast coming from any particular crystal orientation confirming its amorphous structure (similar to the as-deposited sample, not shown here). Going towards higher temperatures, the structure starts to change and when the crystallization threshold is crossed, between 550 °C and 650 °C, the images show diffraction contrast from all over the structure confirmed by SAED patterns. The new crystallographic orientations previously detected in the XRD patterns are responsible for the diffraction contrast seen in the HAADF images. Small grains and boundaries are present throughout the sample cross section.

At the highest annealing temperature (1050 °C), voids are visible mainly towards the bottom part of the film. In Figure 4.16 are also shown the EDX maps of zinc taken on the air annealed samples. The ratio of tin to zinc (Sn/Zn) was calculated applying the Cliff-Lorimer method [147] and using the k_α lines of both zinc and tin. It was calculated that the amount of zinc starts to decrease with increasing annealing temperatures, starting from a value of Sn/Zn=5.4 at 550 °C, which is in agreement with the ratio of the target used during the deposition, to Sn/Zn=9 at 1050 °C. The evaporation of zinc starts to be significant at 650 °C and when the temperature reaches 1050 °C, zinc almost completely evaporates from the bottom part of the film but is still present in clusters at the top surface, as also confirmed by the line profiles to the right of Figure 4.16. The profiles are not homogeneous but seem to reflect an accumulation of zinc at the top surface of the sample. This behavior is thought to be due to the heat source being located at the bottom surface of the sample and therefore making the zinc evaporation possible through its top surface. This phenomenon of zinc evaporation was already reported and the observed evaporation temperature of zinc in an oxygen rich structure sits in between the literature values [148], even if the evaporation rate of a certain species strongly depends on the chemistry of the environment and also the pressure at which the reaction is conducted. As introduced before, Zhu *et al.* [96] performed Extended X-Rays Absorption Fine Structure (EXAFS) on ZTO and reported the bond strength of Zn-O and Sn-O, concluding that Sn-O bonds are stronger than Zn-O bonds, which could be a possible explanation for the evaporation of zinc. The high temperature would provide enough energy in order to break these bonds and release the zinc in the surrounding atmosphere. It is fundamental here to notice that the crystal-
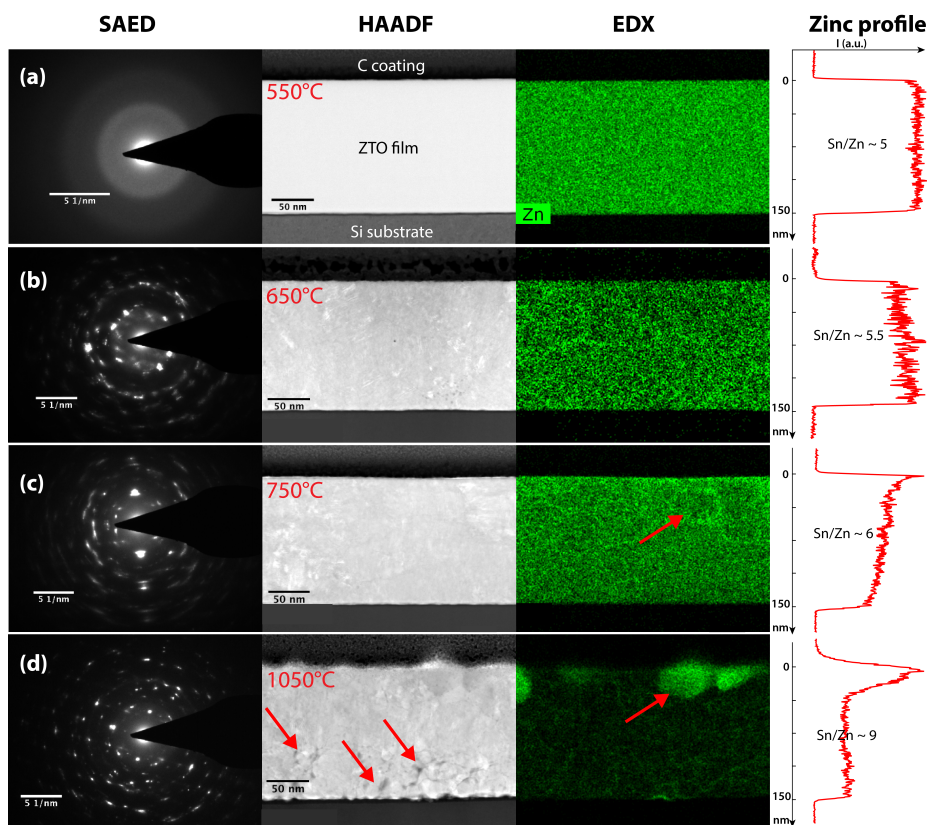
Figure 4.16: Diffraction patterns, STEM HAADF images, EDX maps and zinc depth profile of the ZTO cross-sections, of the samples annealed up to 550 °C, 650 °C, 750 °C and 1050 °C in air. Despite at low temperature the structure appears homogeneous and dense, at temperatures higher than 1050 °C it becomes porous and heterogeneous. Line profiles indicate the transverse distribution of zinc and EDX maps show the evaporation of zinc starting at temperatures higher than 550 °C, right after the crystallization, confirmed by the tin/zinc ratio indicated to the right of EDX maps

Figure 4.17: SAED and HAADF of the layer cross-sections, together with EDX maps taken on the samples annealed up to 600 °C, 900 °C and 1050 °C in vacuum. Contrary to the air anneal case, the structure remains amorphous up to 900 °C. At 1050 °C grain boundaries and voids are visible. In this case, a gradient in zinc concentration is observed, indicating that it starts to evaporate from the top surface, leaving a deficient structure.
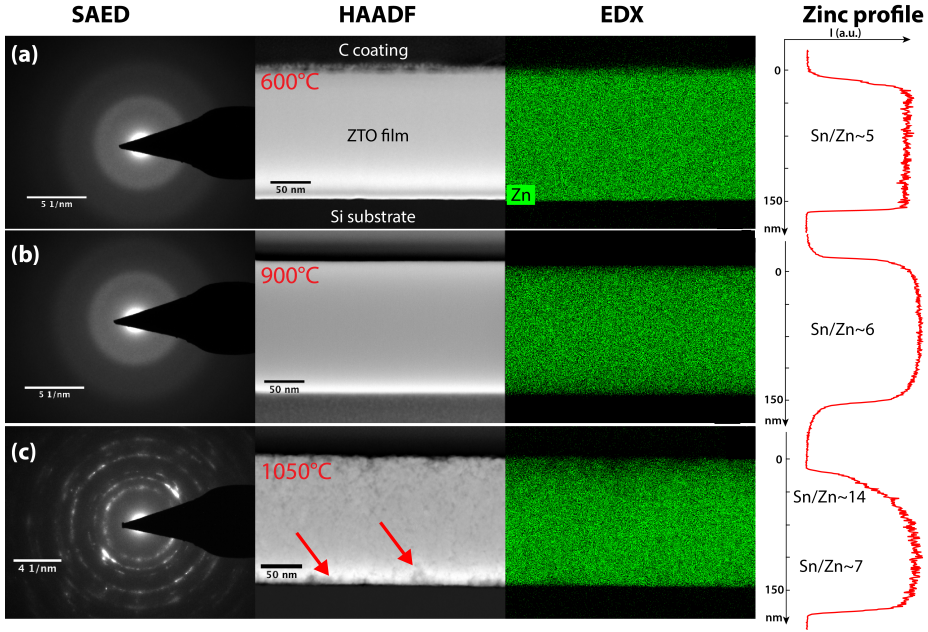
lized structure is not homogeneous, instead, grain boundaries are immediately formed after crystallization. Voids are also created across the samples once the zinc starts to evaporate. The non-homogeneous crystalline structure and the presence of grain boundaries usually have a big impact in the charge transport, acting as scattering centers [144] and charge trapping sites [149]. Other groups [134] also predicted a crucial role for the grain boundaries in decreasing the conductivity because of the accumulation of free carriers and creation of double Schottky barriers. Indeed, as reported in the literature review, having a close packed structure, such as the crystalline one, should facilitate the charge carriers transport. The passivation of oxygen deficiencies can be therefore ascribed as the main cause of drop in the ZTO electrical properties.

The same TEM and EDX analysis were conducted with the samples that underwent vacuum annealing. Figure 4.17 summarizes the results. STEM images, diffraction patterns and EDX maps of vacuum annealed samples confirm, as seen during the *in situ* XRD analysis, that crystallization happens at a higher

temperature in an oxygen deficient atmosphere. At $600\,^{\circ}\text{C}$ the film is still amorphous and homogeneous, with a calculated ratio between tin and zinc of ~ 5. As temperature reaches $1050\,^{\circ}\text{C}$, HAADF image shows a clear change in the ZTO structure, where voids are present near the top and bottom surface, towards the silicon substrate. The calculated ratio of tin to zinc shows that for the highest temperature, less zinc is found towards the upper surface, the ratio calculated in the upper part only was ~ 14, confirming that the element evaporates from the top surface, whereas the ratio calculated taking into account the lower and middle part of the cross section was ~ 7. The line profile are much more homogeneous with respect to before, probably due to the fact that less oxygen comes in from the environment and the formation of stoichiometric tin dioxide is delayed together with the evaporation of zinc. Moreover, zinc is retained to higher temperatures into the amorphous matrix, while, when the material crystallizes, the zinc starts to evaporate.

Despite its evaporation at high temperature, the structural and electrical analysis of ZTO and tin dioxide combined together confirmed that the presence of a small percentage of zinc in the tin dioxide amorphous matrix is responsible for a stabilization of the TCO upon thermal treatments. This fact is clearly shown by both conductivities of ZTO and tin dioxide with respect of the annealing temperature. Other groups [150] [151] [152] also reported that for ZTO and other TCOs, zinc plays a fundamental role in keeping the material stable under heating; *ab initio* calculations were conducted [153] on this topic predicting stable ZTO phases with respect to Zn-O bond lengths, temperature and pressure (such as Zn_2SnO_4 and $ZnSnO_3$). From the analysis of the lattice parameters presented previously, it can be concluded that despite the evaporation of zinc from the already crystalline SnO_2 structure, the lattice parameters length is mostly unchanged. This can be an indication of the fact that, notwithstanding the zinc evaporation, there is no re-organization of the crystalline structure, suggesting that zinc might be dispersed in the structure as an interstitial defect instead of substitutional on a tin site. Figure 4.18 depicts the possible arrangement of tin dioxide structure when a zinc atom is inserted as substitutional or interstitial defect. In order to introduce tensile stress into a crystalline structure, the alien atom has to be bigger than the substituted one, so that it is able to stretch the neighbor atomic bonds. In the case of zinc, as reported above, its ionic radius is smaller with respect to the ones of tin and oxygen, which might be an explanation for the constant trend of the lattice parameters during heat treatment. This could also be the main reason why no change is observed in lattice parameters when the zinc is almost completely evaporated from the tin oxide crystal.
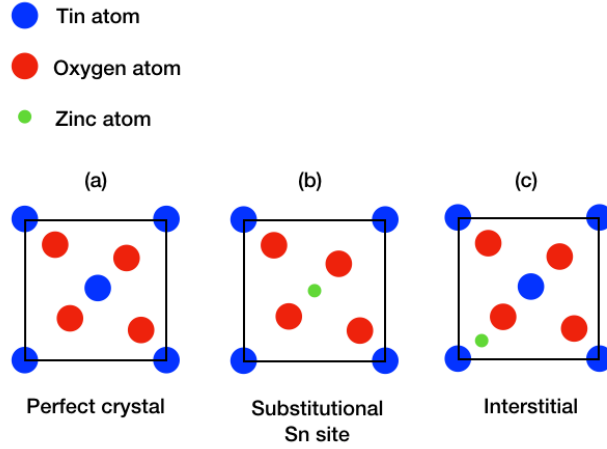
Figure 4.18: Scheme of an elementary cell of SnO_2 oriented in the [001] direction. In (a) the perfect crystal is shown, in (b) a zinc atom is inserted as a substitutional defect into a tin site. In (c) the zinc atom is represented as interstitial defect.

4.7   Conclusions

An in depth analysis of SnO_2 and ZTO was conducted in order to compare the two materials and to study the influence of zinc into the tin dioxide matrix. Both TCO follow similar trends with respect to electrical and structural properties. The drop in electrical conductivity happening after high temperature thermal treatments seems to be linked to an abrupt phase change from amorphous to crystalline. Nevertheless many studies report crystalline TCOs perfectly able to conduct electricity, indeed, we confirmed that the drop in conductivity in our case is due to a decrease in carrier concentration linked to the defects passivation, which are the source of carriers for both SnO_2 and ZTO. Carrier concentration and mobility present different trends depending on the annealing temperature. At low temperatures, structural relaxation might be responsible for the release of charge carriers in the CB, increasing both N and μ, while at medium to high temperatures, the oxygen intake passivates oxygen vacancies and removes sub-gap states, decreasing the number of free carriers in CB and increasing the mobility. Right before the crystallization threshold is reached, the ZTO becomes highly resistive due to a decrease in carrier concentration. PDS measurements helped to verify that the actual defect states located inside the band gap and created by the removal of oxygen from the structure, are completely eliminated after the annealing in an oxygen-rich atmosphere. Moreover, a deficient crystalline microstructure is highlighted by TEM analysis, the presence of grain boundaries and voids created by the evaporation of zinc at high

temperature make the ZTO thin films even more unsuitable for carrier transport. We unveiled that the addition of a small percentage of zinc introduced in the SnO_2 amorphous network is responsible for a delayed crystallization (by $\sim 250\,°C$) and therefore a delayed drop in electrical conductivity, making the ZTO particularly well adapted for high temperature applications. Theoretical values of crystalline SnO_2 unit cell were in agreement with experimental XRD measurements and that the experimental values stayed constant throughout the annealing. Also, specific crystal orientations such as the SnO_2 (200) in air and (101) in vacuum, where found to be more intense with respect to others, this behavior might dependent on the influence of oxygen during annealing. Annealing atmosphere has a crucial role in the electrical properties of the material. We found out that atmospheric oxygen is needed in order to form stoichiometric crystalline SnO_2 and therefore the crystallization occurs only when the correct amount of oxygen is provided to the material. Indeed, when annealed in vacuum, the crystalline phase of SnO_2 is formed $\sim 300\,°C$ after the same phase change in an oxygen-rich atmosphere, despite the stoichiometry of amorphous as-deposited ZTO seems to contain enough oxygen to form SnO_2. We proposed that oxygen already present in the structure, might not be directly available to be re-arranged into the crystalline SnO_2 because it might be bonded to hydrogen and forming H_2O molecules. TDS data confirmed that water is one of the species that comes out of the ZTO at high temperature. For the aforementioned features, especially the remarkable stability under thermal treatments, zinc tin oxide is a promising candidate for high temperature applications, such as monolithic perovskite/silicon-heterojunction tandem solar cells [154], gas sensors [73] and concentrating solar power plants [155] among others [156].

The role of defect and the possible influence of a structural relaxation on the electrical properties is presented in the next chapter.

CHAPTER 5

Defects analysis

5.1 Introduction

As introduced in Chapter 4, a deeper investigation on the mechanisms that govern the trends highlighted in the electrical properties of ZTO is needed in order to understand the material and to make a general model for this type of TCOs. The goal is to deeply understand the material evolution with temperature to make the link between the existing literature and the present experiments and possibly bridge the gap between the theoretical description of such materials and the practical results of experiments that will be presented. In order to pursue this objective, several experiments were put in place to track the defect presence and their evolution. In this chapter we make several hypothesis to describe the aforementioned behaviors and a final model is proposed and supported by the experimental results that are presented in the following sections.

As mentioned in the previous chapter, a first increase in both mobility and carrier concentration between room temperature and 300 °C is observed. The reason behind this increase is thought to be due to some sort of structural relaxation, completely invisible at the TEM and XRD analysis. Yeon *et al,*, Ide *et al.* and Wang *et al.* reported on the observation of such structural relaxation but its role on the electrical properties of TCOs is not always clear [122] [123] [157]. On the other hand, when the influence on the electrical conductivity of a structural

relaxation is indirectly proved (by the observation of carrier concentration), such relaxation is not directly observed experimentally. Moreover, in this range of temperatures, the ZTO is still in its amorphous phase, meaning that any reorganization of the structure is hardly visible using techniques that rely on the detection of some sort of structural order.

The change in electrical properties of ZTO in this range of temperatures (from room temperature to 300 °C), is attributed to a release into conduction band of electrons that were *trapped* in the vicinity of a point defect, regardless of the defect nature, being referred to as the dopant/defect activation. In this case, supplying a small amount of energy, by means of annealing, would help the structure to relax and release electrons in conduction band. To understand if there is a real structural relaxation, it was decided to study the ZTO using techniques such as Fluctuation Electron Microscopy (FEM) and Differential Scanning Calorimetry (DSC). These methods are described in the experimental part of this thesis. The first one is a transmission electron microscopy technique and the latter is a calorimetric technique. Both can be used for the detection of small structural changes of materials.

The carrier concentration and mobility show another trend (decrease in N and increase in μ), highlighted in the previous chapter, between 300 °C and 550 °C. We hypothesize that in this range of temperatures the atmospheric oxygen entering the film and passivating the oxygen vacancies is the dominating process causing the drop in carrier concentration and therefore the increase in mobility. Many authors already reported the link between the oxygen intake and the drop in electrical properties of TCOs, ascribing this phenomenon to the passivation of oxygen-related defects [133] [87] [158]. Furthermore, we showed in the previous chapter that oxygen thermal treatments allow its penetration in the material. Nevertheless, further analysis is needed in order to prove that it is actually oxygen vacancies that are passivated in this range of temperatures. Indeed, many authors propose a mixed presence of defects in such TCOs, in particular, together with oxygen vacancies, metal clusters might be responsible for the increased conductivity in indium-free and indium-based TCOs [159] [160]. In addition, many papers claim that hydrogen intentionally or unintentionally contained in the deposition chambers might act as a dopant for the TCO, increasing the carrier concentration in CB [18] [161] [162]. The goal here is therefore to investigate more on which type of defects are responsible for the observed electrical properties change in this range of temperatures. To achieve this goal, Electron Paramagnetic Resonance (EPR) was employed.

The third phenomenon is, as stated in the previous chapter, the crystallization event taking place abruptly, as confirmed by XRD and TEM. The link between crystallization and passivation of defects was extensively investigated in the previous chapter. The resulting structure is non-homogeneous and shows grain
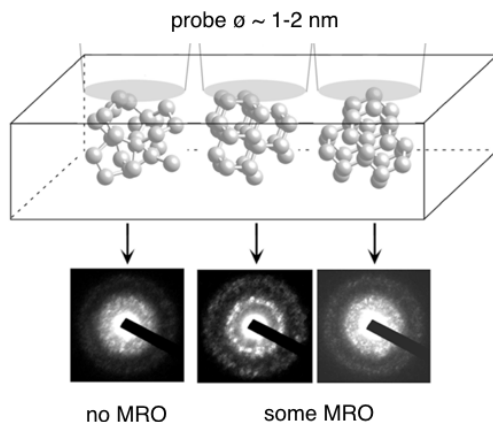
probe ø ~ 1-2 nm

no MRO   some MRO

Figure 5.1: Scheme of a nano-probe illuminating a small portion of a thin TEM lamella and producing different diffraction patterns based on the local arrangement of the material. Examples of DPs showing no medium range order (MRO) and with MRO are presented. For these experiments the average diameter of the probe is around 2 nm. The scheme is not in scale. (Image from [164])

boundaries and voids. EDX also demonstrated the evaporation of zinc, which appears not to have any influence on the electrical properties of the material, since the evaporation follows the ZTO drop in conductivity.

5.2 Fluctuation Electron Microscopy

To study more into detail the first range of temperatures and assess if any structural relaxation occurs upon annealing, fluctuation electron microscopy (FEM) experiments were carried out. These experiments were conducted by Dr. Jeangros at the Ernst Ruska-Centre for Microscopy and Spectroscopy facility in Jülich, Germany. This technique consists in recording hundreds of nano-beam diffraction patterns from small sample volumes ($\simeq 50 \, \mathrm{nm}^3$) by scanning the beam in a raster. The difference between them, if any, is then analyzed through the computation of a function called the normalized variance of the diffracted intensity. This function gives an indication of the magnitude of the fluctuations between one diffraction pattern and the other [163]. This technique is intended to look at medium range order within a material, meaning potential order at the > 5 Å length scale. Figure 5.1 visually summarizes these concepts. The TEM microscope used for these experiments was a probe-Cs corrected FEI TITAN
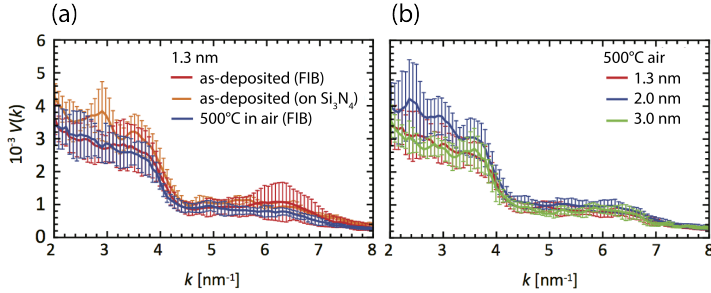
Figure 5.2: (a) Variance of the diffracted intensities of the samples after deposition (prepared either by FIB or by directly depositing ZTO onto Si_3N_4 thin supports) and after annealing at 500 °C in air. This data set was acquired using a probe size of 1.3 nm and a convergence semi-angle of 0.5 mrad. (b) Variable resolution variance data of the FIB-prepared sample annealed at 500 °C acquired using various probe sizes, ranging from 1.3 to 3 nm.

microscope operated at 300 kV. Different probe sizes were used during the experiment, namely 1.3 nm (convergence semi-angle of 0.5 mrad), 2 nm (0.3 mrad) and 3 nm (0.2 mrad). Up to 1200 individual nanobeam diffraction patterns were acquired per condition and groups of 100 patterns were acquired at different positions of the sample. A Mathematica code was written by Dr. Jeangros to analyze the FEM results and in particular to find the center of each nanobeam electron diffraction pattern, then to calculate the rotationally averaged diffraction intensity and finally to compute the normalized variance for groups of 100 nanobeam diffraction patterns. The mean signal of the 12 variance curves is then reported with one standard deviation to the mean error bars. When peaks appear in the normalized variance function, it is an indication of the fact that some medium range order is detected.

ZTO samples were prepared by standard Focused Ion Beam lift-out technique and thinned down to 35 nm for the as deposited sample and 45 nm for the annealed in air at 500 °C. Another thin ZTO film (40 nm) was directly deposited on top of 30 nm Si_3N_4 support in order to avoid any influence of the gallium bombardment from the FIB. Results are shown in Figure 5.2. The absence of well defined peaks indicates the absence of any medium range order, at least within the detection limit of the technique. The visible peaks shown in Figure 5.2 are negligible with respect to the peaks registered when some long range order is present within the structure (as shown in Figure 5.3 for comparison for samples annealed in vacuum). FEM indicates that the structure seems unchanged before and after annealing (but still before crystallization) and also that little to no influence of the preparation method is observed. The difference between the 900 °C curve in Figure 5.3 and the other ones is that in this last case the sample
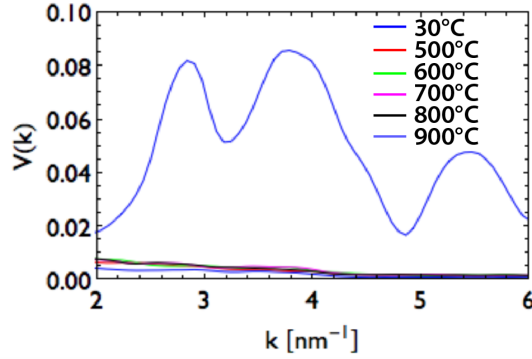
Figure 5.3: Variance of the diffracted intensities of the samples after annealing at $30\,°C$, $500\,°C$, $600\,°C$, $700\,°C$, $800\,°C$ (amorphous ZTO) and at $900\,°C$ (crystalline ZTO) in vacuum.

is crystalline and therefore the long range order in the structure is visible. This high temperature is due to the fact that the sample is annealed in the TEM, hence in high vacuum.

5.3 Differential Scanning Calorimetry

In order to investigate more into the very first range of temperatures where more charge carriers are released in the conduction band and to assess if any structural relaxation is actually happening, differential scanning calorimetry (DSC) was used. This technique is employed to study bulk samples and mainly to track the evolution of the structure with respect to the temperature. When the sample is heated, several phase transitions can take place. Furthermore, when the sample undergoes temperature cycles, the cooling part of the cycle gives information about whether such changes are reversible or not. While measuring the amount of heat released or absorbed, the transition temperatures and the enthalpies can be extracted for a more quantitative analysis. In our case it is sufficient to extract a semi-quantitative information, where the transition temperature is linked to the type of transformation happening in the material, namely, whether it is an endothermic or exothermic process [112] [165]. As described in the experimental part of this thesis, DSC is a technique meant to be used for bulk samples and not suitable for thin films. The strategy to increase the amount of thin-film material in order to meet the minimum requirement of having $1\,mg$ to $10\,mg$ of material, is described in the dedicated section (chapter 3).

Since the goal is to observe the structural relaxation when the material is still in its amorphous phase, an XRD single scan was acquired (Figure 5.4) to make sure that the multi-layer of ZTO deposited on top of a salt substrate was actually mainly amorphous. In this case a single crystal salt substrate was used to deposit the multi-ZTO layers and the XRD pattern is acquired before the lift-off procedure described in the experimental section. The main peaks
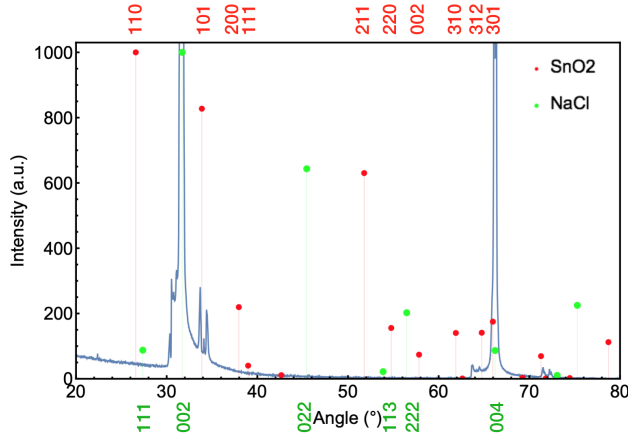

Figure 5.4: XRD pattern of a multiple layers sample of ZTO deposited on top of a salt single crystal substrate. The red and green lines are the theoretical reflections of tin dioxide and sodium chloride. The experimental pattern, in blue, exhibits two intense peaks associated to the salt substrate and one small peak that can be associated to the tin dioxide. Confirming that the material is mainly amorphous. Miller indexes of the main salt and tin dioxide reflections are also indicated.

are the ones associated to the salt substrate (green lines), as it can be seen in Figure 5.4 and little or no peaks are found to be coincident with the tin dioxide theoretical reflections (red lines). Few other peaks not associated with neither the salt substrate nor tin oxide are found around the salt-related peaks. The sharpness of these peaks is an indication of a signal that is a result of a non monochromated beam incident on a mono-crystal. In fact, the unidentified sharp peaks that are situated to the left of the two main salt peaks are due to the incident beam containing enough wavelengths to excite second and third order salt reflections. This effect is particularly pronounced when the sample is mono-crystalline. The other sharp peaks appearing around 34° are most probably related to the environment (substrate and chamber) where the sample is inserted. Indeed, these peaks cannot be related to the known SnO_2 reflections of ZTO because, as seen previously (Chapter 4) and also in Figure 5.8 our material presents broader and much less intense reflections. Sharp peaks are indeed characteristic of single crystals instead of poly-crystalline materials, as

in the case of SnO_2. The material is therefore mainly amorphous.

The main goal of DSC experiments was to anneal the ZTO samples to different temperatures and verify whether the same phase change that occurs in the XRD is also visible using this technique but especially to verify if any transition is seen in the range of temperatures included between RT and $500\,°C$, where a major change in electrical properties is observed. The first trial of experiments was conducted using standard conditions for DSC measurements with not optimized parameters to be compared with the ones used in XRD experiments., in order to have an overview of the material behavior.

Figure 5.5 shows three runs done using an argon flux during the measurements and a heating and cooling rate of $10\,°C\,min^{-1}$. These parameters are the standards for the typical DSC analysis and they were used to test if any signal could be detected. The amount of ZTO flakes inserted in the crucible was $5.5\,mg$. All the three runs were subsequently done using the exact sample that was therefore submitted to a heating step up to $600\,°C$ and cooled down, then the same sample was submitted again to the same treatment and finally, the sample was heated up to $800\,°C$ and cooled down. In the first run (red line), the double peak that
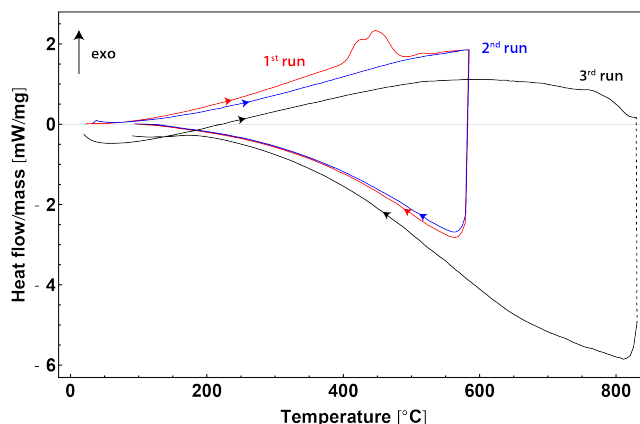
Figure 5.5: Three cycles of heating and cooling of $5.5\,mg$ of ZTO done with a constant argon flux and to $600\,°C$ for the first two and $800\,°C$ for the last one. The arrow to the left of the graph indicates that the exothermic processes point up. The second and third run show a "flat" trend, with no evident peaks showing any phase change or transformation. Observing hysteresis between the heating and cooling part of the curve means that the reactions that took place during the heating phase are irreversible. The dashed black line indicates that the machine lost track of the signal temporarily, during the third run. These runs were conducted with a heating rate of $10\,°C\,min^{-1}$.

can be seen at around $450\,°C$ is an exothermic reaction (as the arrow on the left

part of the graph indicates) and it can be associated to a phase change that is irreversible since the lower part of the curve (cooling part), does not show the same symmetry of the upper part. Since the only major phase transition in our material is the crystallization and in order to make sure that this double peak is associated to it, another run was conducted, using the exact same sample already submitted to the first run. The observed flat curve indicates that no other phase transformations happens in an already crystallized ZTO. A third run was conducted, again with the same sample, to make sure that nothing else would happen to the ZTO if heated to higher temperatures and to confirm that no other transitions were missed during the annealing at lower temperature. The third curve (in black) is indeed characterized by a flat behavior, confirming that the material was most likely already crystalline and no other major change occurred in the structure. The temperature at which the phase change, associated to crystallization (red curve), happened, is $\simeq 100\,°C$ lower with respect to the temperature at which crystallization was observed during *in situ* XRD annealing. This difference is thought to be due to the error associated to the temperature measurement. Indeed, the differences between the present measurement and the ones conducted in the XRD, are the annealing atmosphere and heating rate.

A higher heating rate should influence the phase transition temperatures in a way such that the same transition appears at a higher temperature if the heating rate is higher [166] [167] [168], which is the opposite in our case. Therefore, it is excluded that a higher heating rate could anticipate the phase transition temperature of ZTO. The crystallization detected at lower temperature with respect to what is observed in XRD experiments could be related to the argon flux. In fact, because of the position of the thermocouple inside the DSC, small differences between it and the crucible temperature could be registered, the crucible could be at a higher temperature than what is indicated in the instrument.

In the range between room temperature and $300\,°C$, no evidence of structural relaxation is registered. This could be due to the different parameters used in these trials, since small changes in the curve shape could not be appreciable with high heating rates. The annealing atmosphere could also be responsible for considerable differences in the shape of DSC curves due to its influence on the thermal processes to which ZTO is submitted.

In order to precisely link the DSC measurements with the XRD ones and connect the phase changes with the correct temperatures, the machine was set up with the exact same parameters used during the annealing in the XRD: the argon flux was removed and the heating rate was set at $5\,°C\,min^{-1}$. In addition and in order to remove any residue of carbon, issuing from the preparation method, the ZTO flakes were submitted to a plasma cleaning step. The goal
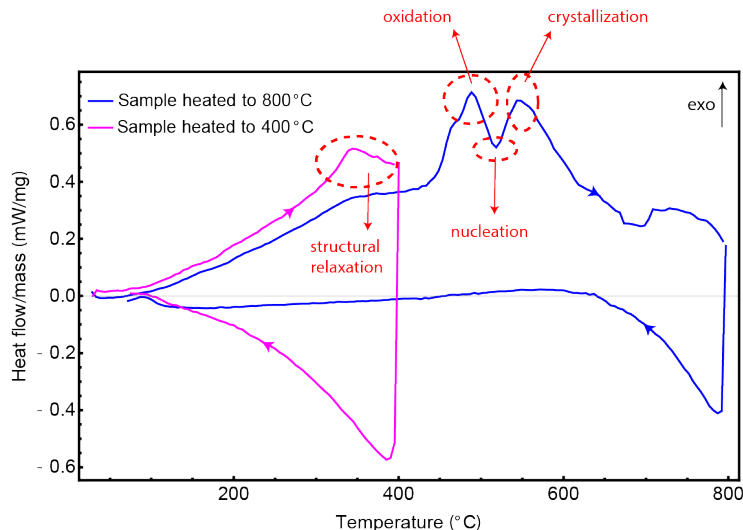
Figure 5.6: DSC curves of ZTO samples annealed in air to $800\,^\circ$C (blue) and $400\,^\circ$C (magenta), with a heating rate of $5\,^\circ$C min^{-1}. The blue curve presents a broad peak associated to the structural relaxation, followed by two peaks that can be ascribed to the oxidation of the material and the crystallization. In between the two peaks a valley is present and is thought to be related to a nucleation process. The magenta curve confirms that the structural relaxation is present even when repeating the experiment with a different sample. All the cycles show a non reversible character of the thermodynamic reactions, highlighted by the flat fashion of the cooling parts of the curves.

was to avoid any signal that might mask the main one, coming from the ZTO. Figure 5.6 shows two cycles done using two different ZTO samples. In blue is shown the sample heated to a maximum temperature of $800\,^\circ$C and cooled down to room temperature. The amount of ZTO flakes for this run was $8.3\,$mg. The curve presents several features. Two exothermic peaks are visible between $400\,^\circ$C and $600\,^\circ$C, with an endothermic valley between them. Included in the range of temperatures between $250\,^\circ$C and $400\,^\circ$C a broad shoulder is visible , whereas the cooling part of the curve appears completely flat, indication that all the reactions that took place are irreversible. To confirm that the broad peak was actually reproducible, another experiment was conducted, with $5\,$mg of ZTO and up to a temperature of $400\,^\circ$C, in order to probe only the interesting range of temperatures. The magenta curve in Figure 5.6 represents the results. The broad peak is again visible and in the same range of temperatures as before. This curve is again characterized by a flat trend in its cooling part. The hysteresis between the heating and cooling part always indicate irreversible thermodynamic reactions.

The broad peaks present in both the blue and magenta curves are thought to be due to a structural relaxation happening at a nanoscale within the material. Little to no references were found in literature regarding DSC analysis conducted onto thin film TCOs. Nevertheless, Roorda *et al.* [169] studied the structural relaxation of amorphous and crystalline silicon after helium bombardment, and even with the obvious differences, the DSC measurements can be compared to our results. Figure 5.7 shows the DSC graphs obtained by Roorda *et al.*. Both the crystalline and amorphous phase of silicon were analyzed in this graph. While the amorphous phase crystallizes around a temperature of $670\,°C$, the already crystalline phase doesn't show any peak. Both curves show a broad shoulder between $100\,°C$ and $500\,°C$ that was linked to a relaxation of the silicon structure. The reason why the structural relaxation is not represented by a sharp peak but rather a broad shoulder resides in the physical explanation of this process. A sharp peak in this type of analysis is a clear indication of a phenomenon characterized by a single activation energy and once this energy is reached, the process starts and ends relatively quickly. On the other hand, the structural relaxation in the mentioned study is linked to the removal of the ion beam induced damage, which is a process not associated to a single activation energy. Furthermore, the relaxation is most probably due to a combination of physically different processes, such as the relaxation of distortions in bond angles and release of stored energy in addition to the annihilation or conglomeration of defects (vacancies, dangling/floating bonds, interstitial defects). All the mentioned process are characterized by different activation energies, which would lead to a curve with broad shoulders instead of sharp peaks.

In our material, this structural relaxation can be caused by the annihilation of network defects of different nature, therefore not characterized by a single activation energy, giving a broad appearance to the peak.

One last comparison that can be made concerns the order of magnitude of the flow of released or absorbed heat by our material with respect to what is found in literature. In Figure 5.7 b is shown a zoom in of the structural relaxation curve obtained for amorphous and crystalline silicon. It can be noticed that the released flow of heat by the sample during the structural relaxation is comparable to what was found in our experiments (heat flow on the order of $0.2\,mW$). The peak associated to the structural relaxation in Figure 5.6 is absent in Figure 5.5. These measurements are indeed extremely sensitive to the shape and distribution of material inside the crucible. Thin films are not meant to be measured by standard DSC, since flakes floating inside the crucible might influence the heat distribution and therefore the recorded signal. In a separate work carried out by our group, it was demonstrated that the increase in electrical properties happens, in the range of temperatures included between room temperature and $300\,°C$, regardless of the annealing atmosphere [124], corroborating the hypothesis that only a thermodynamic process independent of the
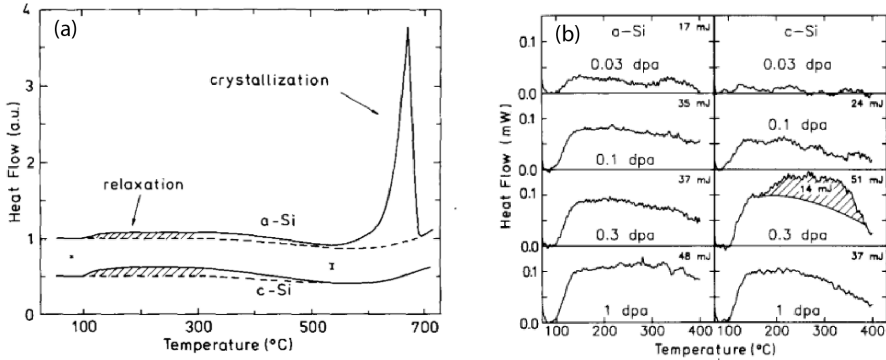
Figure 5.7: (a) DSC curves of helium bombarded crystalline and amorphous silicon. The amorphous silicon presents a sharp peak at $670\,°C$ representing the crystallization, that is not present in the already crystalline sample. The broad shoulder between $100\,°C$ and $500\,°C$ is associated to the structural relaxation of the samples during the annealing [169]. A zoom in (b) of the previous curves with the indication in y-axis of the order of magnitude of the heat flow released by the sample during the structural relaxation.

atmosphere, such as structural relaxation, could cause the mentioned changes in the electrical properties. Indeed, during the annealing with the argon gas injected into the chamber, the structural relaxation might appear under the form of the shoulder present between room temperature and $400\,°C$.

Despite the difficult comparison with existing literature, analogies can be extracted from Figure 5.6 and Figure 5.5: two peaks (exothermic processes) are spaced out by a valley (endothermic process). Considered the variations of electrical properties of ZTO and the relative temperature ranges, the first peak can be most likely associated to the oxidation of the material. Small variations of temperature can be ascribed to the fact that slight differences in the temperature detection can be present between different instruments such as DSC, XRD and the hot plate. Oxidation phenomena are exothermic processes where energy under the form of heat is released by the material [170] [171]. This oxidation was already described as the cause of the increase in mobility and decrease in carrier concentration between $350\,°C$ and $500\,°C$ because of oxygen vacancies passivation (Chapter 4). The valley observed between the two peaks at $520\,°C$ is assigned to the nucleation, which takes place immediately before the crystallization. Nucleation, in contrast with the previous reactions, is known to be an endothermic process [172], therefore represented with a valley in our convention. Such nucleation triggers the crystallization of the films.

As introduced before, the only change registered between air and argon annealing lies in the detection of the correct chamber temperature. Oxygen remains
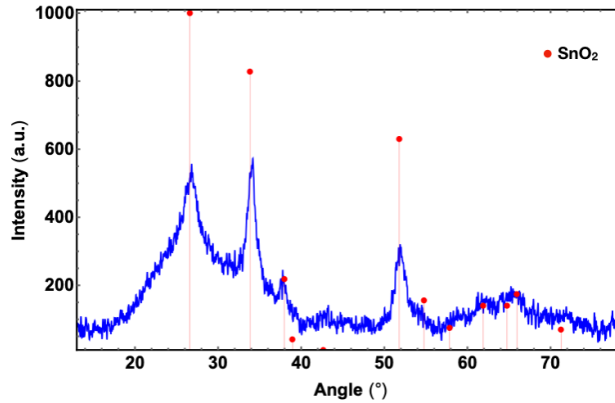
Figure 5.8: *Ex situ* XRD pattern obtained on the ZTO flakes after the DSC measurements. The main theoretical reflections of tin dioxide are present in the experimental pattern, confirming that the sample is crystalline.

trapped into the closed crucibles regardless the gas flowing in the external part of the chamber and is sufficient for the material to undergo the same transformations reported by *in situ* XRD conducted in air. As a proof, when the crucible containing the ZTO flakes is extracted from the DSC furnace, the flakes appears transparent rather than brown, which is the typical signal of an oxidized ZTO.

The last peak appearing on the heat flow curve around $550\,^{\circ}$C is associated with the crystallization of ZTO, which is an exothermic reaction [173] [174] [113].

In order to double check if the crystallization actually happened after the DSC cycles, *ex situ* XRD experiments were conducted after each DSC cycle. Figure 5.8 shows the XRD pattern obtained on the air annealed sample (represented in blue in Figure 5.6). Contrary to the XRD graph in Figure 5.4, the one in Figure 5.8 does have the main peaks associated to tin oxide, which confirms that the material is mainly crystalline.

5.4 Electron Paramagnetic Resonance

Once assessed that a re-arrangement of the ZTO amorphous structure is present when the sample is submitted to heat treatments, one last question to be answered is what type of defects are actually present in the film and are subjected to annihilation or passivation once the temperature raises and oxygen penetrates into the film. The removal of these defects, related to oxygen vacancies,

is thought to be the cause of the decrease of carrier concentration between 350 °C and 550 °C and the corresponding increase in mobility. In order to investigate more on the nature of these defects, electron paramagnetic resonance (EPR) experiments were conducted. This technique allows to probe paramagnetic defects if they are present in the sample, to identify and to quantify them. The magnetic field induces the splitting between the $-1/2$ and $+1/2$ spin states and the absorption of electron magnetic waves is recorded. This absorption leads to a transition between the spin population in the lower energy state to the upper state. A calculation is then conducted to extract the *g-value*, which is a fingerprint of the defect type.

In order to have a general overview of the samples behavior and detect paramagnetic defects, a large range of magnetic field was probed and the signal was recorded. Figure 5.9 exhibits the results issuing from this measurement for the
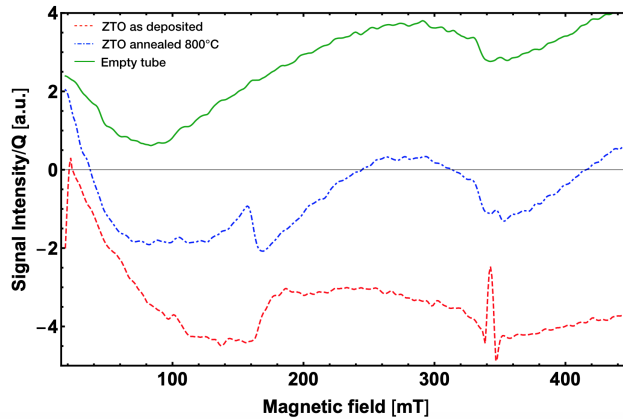

Figure 5.9: High range magnetic field measurements of as deposited ZTO (red dashed), annealed ZTO at 800 °C in air (blue dot-dashed line) and for comparison, the signal coming from an empty quartz tube (green) inserted in the resonator to understand which part of the signal was to ascribe to the tube itself. In the annealed sample, a signal is detected around 160 mT. The broad shoulder present between 160 mT and 340 mT can be related to either the background signal of the ESR900 Oxford quartz finger cryostat or the Bruker SHQ resonator. A signal is also registered around 343 mT in the as-deposited sample. The measurement conditions used for the majority of the acquisitions were the following: 38 dB of attenuation on 200 mW of fundamental microwave power, microwave frequency adjusted to 9.6 GHz, acquisition temperature 300 °C.

as-deposited sample and the annealed in air at 800 °C. The figure shows the first derivative of the absorption signal, which is used instead of the absorption peak because the structure of the signal is amplified and there is a much better

signal to noise ratio. At lower magnetic field, the annealed sample shows a signal (around 160 mT) that we expect to be related to contamination, giving the fact that this sample was annealed in the DSC chamber, and previously generously manipulated in order to obtain the ZTO flakes. In particular, this signal might be associated to iron-related defects [175] [176] [177] [178] (most probably coming from the oven used for the samples annealing). The as-deposited sample presents a similar onset around the same value of magnetic field, which again, can be associated to contamination. No other important signals were detected during these runs. The signal of an empty tube was also recorded in order to exclude any possible artifact from the actual measurements. Around 343 mT, a significantly intense signal is recorded. The magnetic field value corresponding to the one found in Figure 5.10 is linked to a defect which sits next to a tin atom in the ZTO matrix. In particular, the obtained g-values are similar to the ones found by Shi *et al.* [179] and attributed to oxygen vacancies. Oxygen vacancies can exist in three different charge states in an oxide: neutral V_O^0, singly ionized V_O^+ and doubly ionized V_O^{++}. Since EPR can only detect paramagnetic species, the defects illustrated in Figure 5.10 can only be related to the singly charged oxygen vacancies, since they have one unpaired electron. Popescu *et al.* [180] also reported similar g-values for singly ionized oxygen vacancies but they also showed EPR spectra presenting multiple peaks associated to Sn^{3+} centers, which are absent in our case. The measurements of the extended magnetic field range were performed with a large magnetic field modulation amplitude of 1 mT, which leads to overmodulation of narrow signals. This magnetic field range is therefore taken as a base to zoom-in and perform other measurements with smaller magnetic field steps, lower field modulation and more averages. This leads to better resolution and to better signal-to-noise ratio.

In order to verify if any difference in the concentration of defects was detected between a sample treated at high temperature, supposed to have very few defects and the as deposited one, thought to be rich in defects, a second trial of EPR experiments was conducted using the as-deposited sample and the one annealed at 800 °C in air. The result is shown in Figure 5.10, where the two measurements are superposed for comparison. These measurements are qualitative and contain no information about the precise number of defects because the specific mass of ZTO introduced into the quartz tube was difficult to weight in both cases. In the extended field range we observed that there is a signal for the as deposited sample close to $g = 2$. In order to identify the origin of this signal, simulations were performed (not shown here) and the following g values were extracted: $g_x = 2.00193$, $g_y = 2.00216$ and $g_z = 1.99734$. These values were obtained after a fitting of the red curve in Figure 5.10. As the figure shows, the g anistropy can be explained by different symmetries of the microscopic magnetic field distribution (*i.e.* the spin) of the paramagnetic species, or, in other words, by a distortion of a sphere like spin symmetry. This symmetry is dependent on the spin density distribution in the thin film structure and therefore also depen-
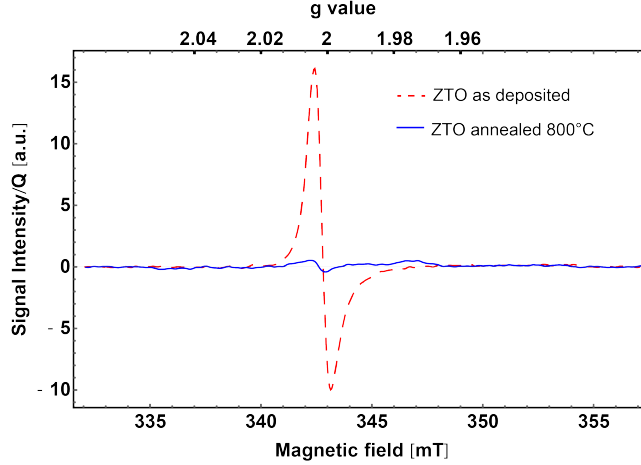
Figure 5.10: Qualitative EPR measurements of two ZTO samples, the as-deposited one (in red dashed) and the annealed at $800\,^{\circ}\mathrm{C}$ in air (in blue). The comparison shows that the as deposited sample has many more defects with respect to the annealed one.

dent on the electronic structure and arrangement of the atoms in the film. The derived g matrix can be described as axial, since g_x and g_y are similar meaning that there exists one distinct g-axis in the defect.

These values were obtained conducting a specific fitting of the red curve in this figure. Having three different values for g means that there is anisotropy in the coupling between the unpaired electron and the neighbor nuclei, which is visually explained in Figure 5.11. The different shapes in the upper part of the sketch in Figure 5.11 represent the symmetry of the total orientation between the external magnetic field and the magnetic fields of the molecule or crystal coupled with the spin momentum of the unpaired electron. In order to investigate more the characteristic g-values of a sample, more advanced EPR measurements would have to be carried out. Hence, here the focus is kept on the results obtained in Figure 5.10. From Figure 5.10 it is straightforward to assess that the as deposited sample is characterized by a more intense signal with respect to the annealed one, meaning that a larger concentration of defects is present in this sample, which confirms the hypothesis made when analyzing the electrical properties of the samples.

The goal of the EPR experiments was nevertheless to count the amount of defects present in the film and eventually compare these numbers to the measured electrical properties, keeping in mind that EPR is able to count just a small part of the defects present in the ZTO, the ones with one unpaired electron.
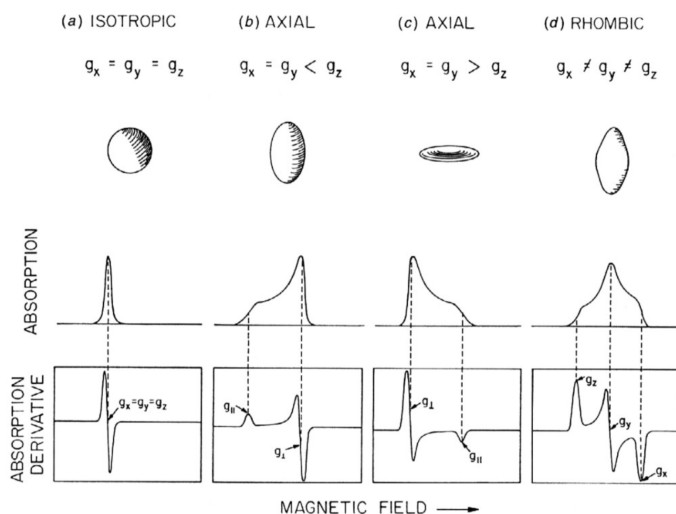
Figure 5.11: Several possible symmetries for the magnetic field associated to the molecule/crystal are shown in (a), (b), (c) and (d). According to the symmetry, the single components of g will assume certain values: the highest symmetry corresponds to three equal components $g_x = g_y = g_z$ whereas the shape with lowest symmetry corresponds to $g_x \neq g_y \neq g_z$. In the bottom part of the image the shape of the absorption peaks and their first derivatives are shown (sketch from E. Duin - Auburn University).

To investigate more quantitatively the amount of defects, a new series of experiments was set up. Instead of using the ZTO flakes prepared for the DSC analysis, the ZTO was deposited directly on top of dedicated quartz substrates, previously treated to remove any defect, and with dimension of $2\,\text{cm} \times 2\,\text{mm}$, that perfectly fit into the quartz tube that is inserted into the resonator. In order to increase the EPR signal and to tackle any thickness effect, two batches of samples were deposited with 150 nm and 300 nm-thick ZTO. The samples were annealed in air at different temperatures up to 800 °C to obtain a total of fifteen samples. Having two different thicknesses helped to better tune the equipment in order to have the highest possible signal. On the other hand, the ZTO being conductive when annealed at low temperatures, the effective tune of the resonator was disturbed by the electric field generated inside the sample so a trade-off between the presence of an intense signal and the high conductivity of the material had to be found. The derivative of EPR signals are presented in Figure 5.12. The main signal detected in Figure 5.12 is the one ascribed to the singly ionized oxygen vacancies appearing around 343 mT and associated to the g-values calculated before (Figure 5.10). It is interesting to notice that the signal intensity decreases when the annealing temperature increases, down to a
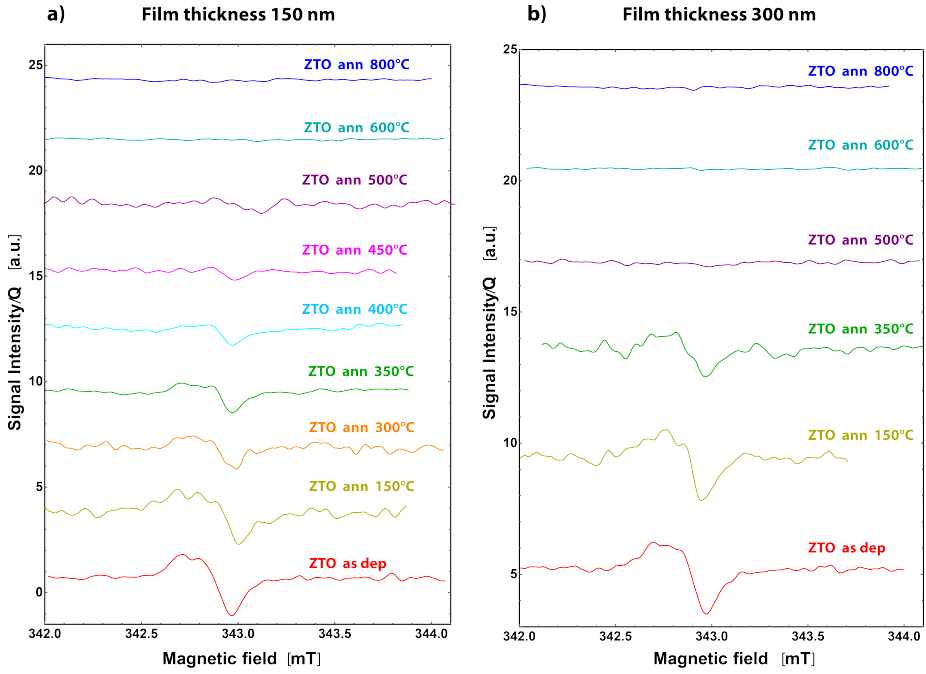
Figure 5.12: Signal intensity over quality factor with respect to the magnetic field of (a) 150 nm-thick ZTO samples and (b) 300 nm-thick samples. The magnetic field range was reduced even more in order to have more counts in the interesting interval. The key information is the relative intensity of each signal rather than the absolute value reported in the y-axis. The signal intensity is related to the amount of paramagnetic defects inside the sample. The higher the annealing temperature, the lower the concentration of defects in the material.

point where defect values are within the error range, at an annealing temperature between $450\,°\mathrm{C}$ and $500\,°\mathrm{C}$, which corresponds to the temperature where the large drop in electrical properties is observed.

The amount of defects detected during EPR experiments are absolute numbers, but if the volume of the sample is known, the amount of defects per unity of volume can be calculated and eventually linked to the carrier concentration obtained from the Hall effect measurements. The samples measured during the second batch of experiments were deposited on top of a substrates with the following dimensions: $2\,\mathrm{cm} \times 2\,\mathrm{mm}$, with a thickness of $150\,\mathrm{nm}$, giving a total volume of deposited ZTO of

$$V_{\mathrm{total}} = 600 \times 10^{-8}\,\mathrm{cm}^{-3}. \tag{5.1}$$

In the as-deposited sample, the amount of paramagnetic defects detected by EPR was $N = 4.14 \times 10^{12}$, corresponding to a defect density of:

$$\frac{N}{V_{\mathrm{total}}} = \frac{4.14 \cdot 10^{12}}{600 \cdot 10^{-8}} = 6.9 \cdot 10^{17}\mathrm{cm}^{-3}. \tag{5.2}$$

This defect concentration is represented in Figure 5.13 for each sample. The error on the EPR measurement is the limit of detection of the used equipment, estimated during the background subtraction procedure explained in chapter A and is equal to 10^{11} spins. Using the error propagation theory, it was estimated that the corresponding error on the determination of defect concentration is $\simeq 2 \times 10^{16}$ spins. The numbers reported in this graph are, therefore, not absolute values but they are re-modulated with respect to the ZTO volume on each sample, hence, they represent the concentration of paramagnetic defects in each ZTO sample with respect to the annealing temperature. The amount of defects present in the thick ZTO samples was expected to be doubled as the amount of defects present in the thin one. However, Figure 5.13 shows the opposite trend. This behavior might be due to the fact that paramagnetic defects are not dispersed in the whole sample volume, but rather in the surface. Further investigations are therefore needed in order to deeply analyze this effect.

If it is assumed that the numbers in Figure 5.13 represent the defects identified as singly ionized oxygen vacancies, these defects will be able to donate one electron each to the conduction band. From the analysis of the vast literature on defects in tin-based TCOs (see Chapter 2) it can be assumed that together with singly ionized oxygen vacancies, there is at least a similar amount of doubly ionized oxygen vacancies, not detected by EPR, that will also contribute to the conduction with both electrons, the total number of charge carriers per cubic centimeter would be

$$N_{\mathrm{total}} = N_{\mathrm{singly}} + N_{\mathrm{doubly}} \simeq 7 \cdot 10^{17} + 2 \cdot 7 \cdot 10^{17} \simeq 2 \cdot 10^{18}. \tag{5.3}$$
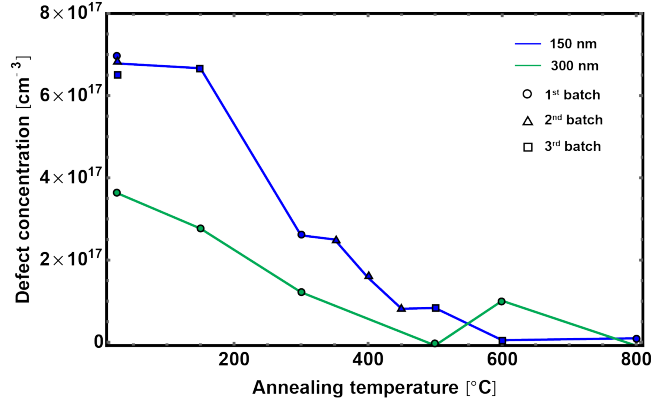
Figure 5.13: Concentration of paramagnetic defects with respect to the annealing temperature found in 150 nm and 300 nm-thick ZTO samples by EPR. The amount of defects continuously drops with the increase of annealing temperature. Discrepancies on the amount of defects between the 150 nm and 300 nm-thick ZTO samples might be due to a surface effect. Samples were deposited in three separate batches.

The results are consistent with the expected trend, for which the higher the annealing temperature, the lower the amount of defects present in the films. The reason being that the majority of defects can be associated to oxygen vacancies, as discussed previously, which are passivated during the air annealing up to a point where the material becomes stoichiometric and the crystallization occurs, with a consequent drop of the electrical properties. Indeed, the carrier concentration for the as deposited sample measured by Hall effect was around $6 \cdot 10^{19} \mathrm{cm}^{-3}$. The difference of one order of magnitude between the previous estimation and the experimental number could be due to the contribution of other defects linked for example to the presence of hydrogen within the film (proven by hydrogen forward scattering (HFS) experiments, not shown here) or metal clusters (already linked to the presence of a vacancy) that were predicted by DFT calculations [124] [181] [182]. The decrease in paramagnetic defects observed during EPR experiments does not follow the exact same trend observed in carrier concentration. Indeed, the amount of paramagnetic defects starts to decrease already at lower temperature, whereas the carrier concentration N, measured by Hall effect, increases first and then starts to decrease (from a temperature of $\simeq 300\,°\mathrm{C}$). This effect is thought to be due to the structural relaxation, which has the effect of release charge carriers in CB and that cannot be seen during EPR experiments. Indeed, the type of defects released by the readjustment of the structure are most probably not related to oxygen in any way, the proof being that the relaxation is observed in ZTO regardless the annealing atmosphere. Figure 5.14 represents the different trend for charge carriers N measured by Hall effect and paramagnetic defects measured by EPR. Except
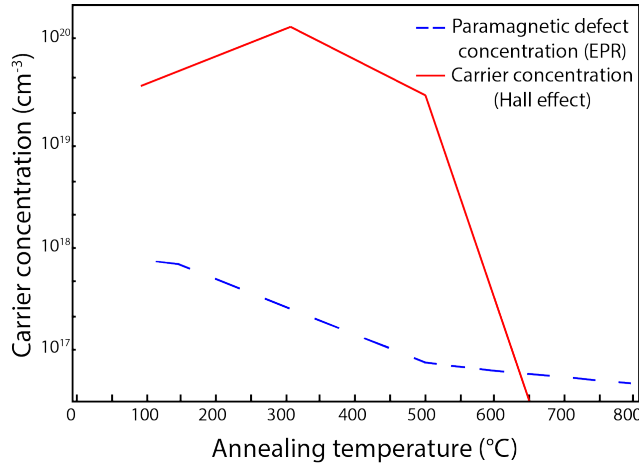
Figure 5.14: Concentration of paramagnetic defects with respect to the annealing temperature found in ZTO samples by EPR. The amount of defects continuously drops with the increase of annealing temperature, with almost no variation from the calculation conducted for thinner and thicker samples.

for the two order of magnitude between the values, already accounted for in the previous calculation, the numbers follow a similar trend: N increases from a starting value of $\simeq 6 \times 10^{19} \, \text{cm}^{-3}$ (room temperature) to $\simeq 10 \times 10^{19} \, \text{cm}^{-3}$ at $300 \, ^{\circ}\text{C}$, to then decrease to zero at a temperature of $650 \, ^{\circ}\text{C}$. On the other hand, in the amount of paramagnetic defects, thought to be linked to singly ionized oxygen vacancies, the increase between room temperature and $300 \, ^{\circ}\text{C}$ is not registered, since it decreases down to zero at a temperature of $800 \, ^{\circ}\text{C}$. The majority of defects in our ZTO is indeed related to oxygen vacancies (singly and doubly ionized), hence the following drop of carrier concentration follows the same trend in both EPR and Hall effect measurements. The mismatch on the temperature at which the defects are reduced to zero is due to the fact that EPR is a more sensitive technique than the Hall effect, so it allows to calculate the amount of defects up to smaller values. These values of N (between $650 \, ^{\circ}\text{C}$ and $800 \, ^{\circ}\text{C}$) are anyway not enough to ensure the conduction in our material.

These observations confirm that the reason why the ZTO conductivity drops is to be imputed to the lack of defects rather than to a phase change. Indeed, the transition from amorphous to crystalline structure occurs at a temperature where the conductivity drop is already reported and therefore independent from it. The crystallization is rather driven by the material becoming stoichiometric, since the defects are already passivated during the annealing. Grain boundaries and defects of the crystalline structure reported by TEM analysis in Chapter 4 have little to no influence on the carrier transport, since the concentration of

these carriers is already low at the crystallization temperature.

5.5   Conclusions on the defect analysis

As seen in this chapter and following the analysis started in the previous one, the combination of FEM, DSC and EPR shines a light on to the variation of electrical properties of ZTO and in particular these three combined techniques help to clarify why the electrical properties show three regimes.

In the first regime (from room temperature to 300 °C), FEM and DSC show that despite no change in MRO was detected, a re-organization of the ZTO amorphous structure causes a release of charge carriers in the conduction band. The small structural change are not detected by TEM or XRD (which confirm the amorphous state of the material) but the calorimetric analysis clearly highlighted an increase of the amount of heat exchanged between the ZTO and the environment, assessing the presence of a non-reversible thermodynamic reaction at low temperature (300 °C). The fact that the increased carrier concentration is detected regardless the annealing atmosphere is an indication that the released charges are not related to oxygen. Because of the practical difficulties encountered during DSC experiments, another route that could be followed to investigate more into the first range of temperatures might be to use a dedicated equipment for thin films such as the *nano-calorimetry*. The heating elements are conceived so that the sample can be deposited directly on them and instead of being inserted in a furnace, samples are heated by electrical resistances. Moreover, a greater freedom is guaranteed in terms of heating rates and maximum attainable temperature [183] [184] [185].

In the second regime (from 300 °C to 550 °C), DSC and EPR show that considerable change happen in the structure and stoichiometry of ZTO. An exothermic reaction, associated to the oxidation of the material confirms the trend highlighted by EPR, which assesses a constant decrease of paramagnetic defects associated to singly ionized oxygen vacancies. The amount of these defects, in this range of temperatures, reproduces well the numbers obtained by direct measurements such as Hall effect. The decrease of charge carriers is not reported when the annealing is conducted in vacuum, indication of the fact that oxygen is the responsible for the passivation of such defects.

In the third regime (from 550 °C on), EPR combined with XRD and TEM observation confirmed that the amount of charge carriers decreases in the ZTO slightly before the crystallization threshold is crossed. In fact, the drop of carrier density is considered to be the cause of the crystallization itself, since all the defects are removed from the ZTO matrix and the material is quasi-stoichiometric to be able to change phase and crystallize. The resulting crystalline material is therefore completely insulating. When the temperature increases ($\simeq 650$ °C) the zinc dispersed as an interstitial defects in the ZTO matrix starts to evaporate,

leaving a non-homogeneous structure. The schematic drawing of the aforementioned processes is shown in Figure 5.15. In the next chapter, an attempt of doping the ZTO will be presented, with the goal of increasing its conductivity in the range of temperatures presented before.
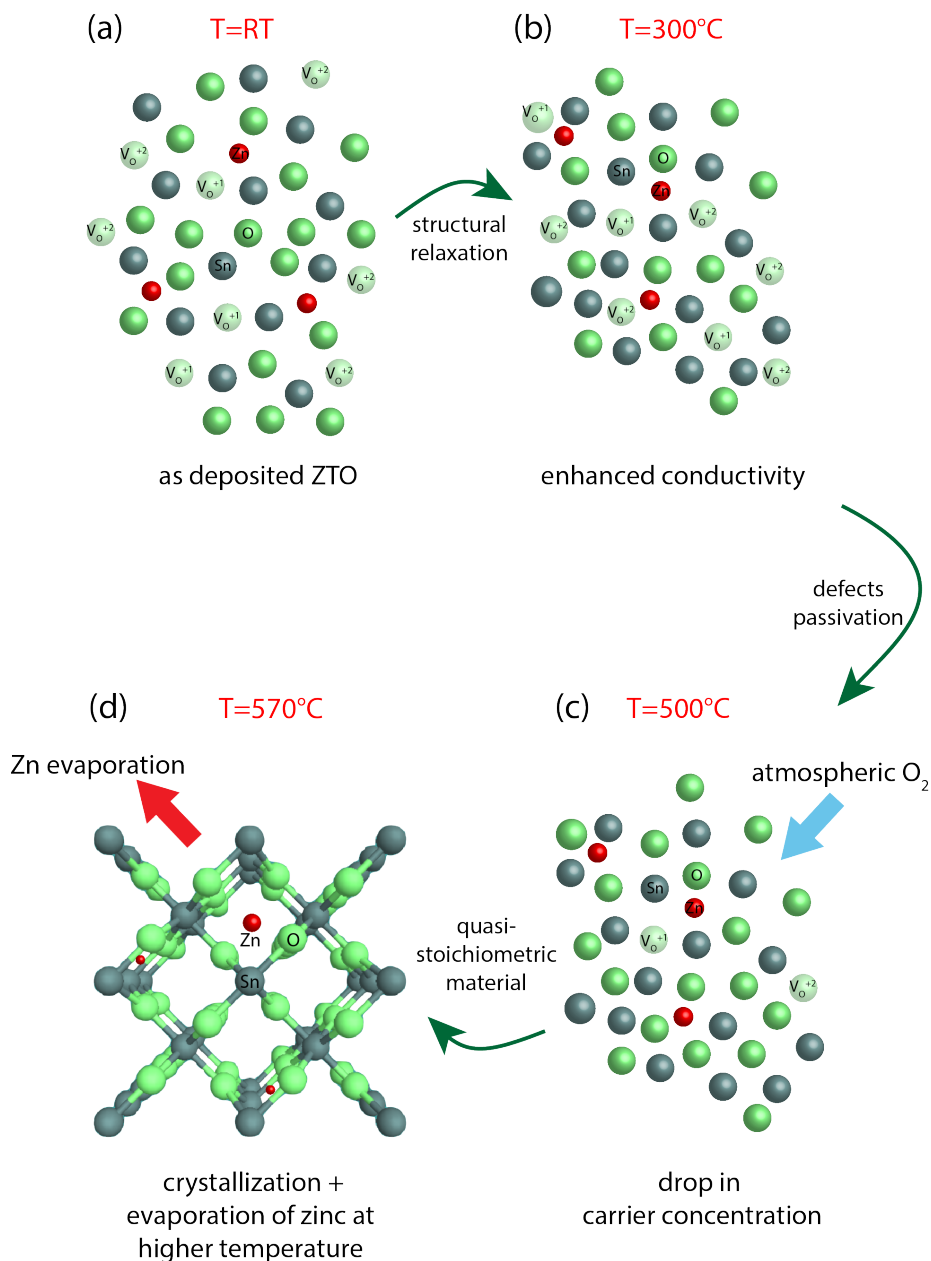
Figure 5.15: Schematic representation of transformation happening in the ZTO during annealing in air. These structural modifications give rise to the change observed in the electrical and optical properties. Structural relaxation (from (a) to (b)), oxygen passivation (c) and finally crystallization (d). The different atoms are not in scale.

Crystallization model of TCOs

6.1 Introduction

In this chapter an overview of the physical and chemical processes governing the crystallization and growth of tin-based TCOs will be given and in order to formulate a model, the comparison between tin-based and indium-based TCOs is taken into account. The differences in crystallization kinetics of tin and indium-based TCOs are first introduced and then, several hypothesis are formulated before presenting a model for the growth mechanism in both TCOs. The influence on the crystallization kinetics of annealing temperature, atmosphere, chemical composition and thickness of materials is investigated. The experimental results are discussed in comparison with the existing literature.

6.2 Indium-based TCOs

In order to compare the crystallization behavior of tin-based TCOs with industry standard TCOs, an indium-based material, zirconium-doped indium oxide, (In_2O_3:Zr - IZrO) was deposited in the Leybold Univex using the following parameters:

- RF magnetron sputtering

- room temperature on aluminoborosilicate glass

- target with 98/2 weight composition ratio of In_2O_3/ZrO_2

- power density of $0.95\,W\,cm^{-2}$

- mixed atmosphere of argon and oxygen with O_2 partial pressure variation between 0% and 0.4%

- base pressure of $1 \times 10^{-6}\,mbar$

The composition of as-deposited IZrO measured by RBS is $Zr_{0.01}In_{0.40}O_{0.59}$. Despite the existing literature [186] [187] [188] on zirconium-doped indium oxide, little was found with respect to its structural properties and their evolution with respect of parameters like the annealing temperature or film thickness. The electrical and optical properties of IZrO were studied along with its structural properties. Optoelectronic properties are proved to be superior with respect to the tin-based TCOs ones due to higher carrier concentration and mobility [189] [190] [55] [191]. Thanks to these enhanced optoelectronic properties, we were able to deposit thinner materials in order to decrease the amount of indium contained in each sample, since indium is among the less abundant elements in the earth crust. The variation of IZrO thickness allowed us to systematically study its structure, the amorphous-to-crystalline phase transition and finally helped us to formulate a general model for the growth mechanism and its evolution. Several samples of IZrO were deposited with different thicknesses namely 15 nm, 25 nm, 50 nm and 100 nm and some of them were submitted to heat treatments in different atmospheres, in particular, air, hydrogen and nitrogen atmosphere (the last two with a pressure of 0.5 mbar) for 30 minutes. The influence of the film thickness on the crystallization kinetics is first investigated. IZrO samples were directly deposited on top of TEM dedicated grids, so that the microscopy observation could be conducted without any preparation step in between. Despite being overall amorphous, STEM top views show several crystalline inclusions, confirmed by the respective diffraction pattern. In order to count them, a dedicated plug-in of the software ImageJ was used, which is based on the automatic recognition of features (segmentation) present in an image. The following procedure was adopted:

- the image type is modified into a binary one, so that black particles show against a white background;

- the image is screened by the particle size, which is manually entered and used as a input, together with the particle circularity;

- the software automatically recognizes all the particles in a certain area.

Figure 6.1 shows this process. Starting from a BF STEM image, an output where the counted particles are outlined is displayed, then, an areal density (μm^{-2}) of particles present in each image is given. A fundamental remark to the count of particles, using STEM BF images as a input for the segmentation procedure, is that because of how the image is formed, not all the crystalline seeds present in the film are visible in the bright field (or dark field) STEM image. This is due to the fact that only the crystallites that are oriented in zone axis or near zone axis diffract electrons and are therefore visible in the final image. However, all the crystalline particles that are randomly oriented with respect to the electron beam do not diffract and therefore result to be completely invisible. An example of this effect is visible in Figure 6.4 (c), where together with white and dark crystalline particles, light grey ones are visible, down to a point where it is difficult to distinguish if the contrast is linked to actual particles or to the background. From the values obtained after the segmentation, it can be concluded that the number of crystalline seeds increases with the material thickness, but if the thickness of each film is taken into account, an average volumetric density of 43 seeds/μm^3 is obtained for all films. As opposed to what was observed in tin-based TCOs, IZrO does not crystallize in a conical-shaped fashion up to the observed thicknesses (100 nm), but small crystalline seeds are dispersed in the amorphous matrix.

When annealed at 200 °C for 30 minutes, IZrO crystallizes with the trend shown in Figure 6.2. As highlighted by the figure, all the IZrO samples appear completely crystalline. Figure 6.2 (a) shows a contrast which is associated with bend contours present in the film when its thickness is lower than 20 nm. Similar behavior was found in literature [14]. The tensile stress is associated to coalescence between atomic scale islands that elongate towards each other in order to form crystalline agglomerates and fill in the space [192]. As soon as the thickness increases, crystalline grains appear in the images and the thicker the sample, the smaller the grain size. The diffraction pattern in Figure 6.2(f) was indexed, using the software JEMS, as the body-centered cubic structure (bixbyite-like structure) typical of indium oxide [90]. The grain size was calculated for all the samples using the method illustrated in Appendix and gave the results shown in Table 6.1.

Table 6.1: Grain size calculated for three different thicknesses of IZrO samples.

Thickness (nm)	Grain size $\pm\sigma$ (nm)
25	(473 ± 43)
50	(418 ± 50)
100	(320 ± 15)
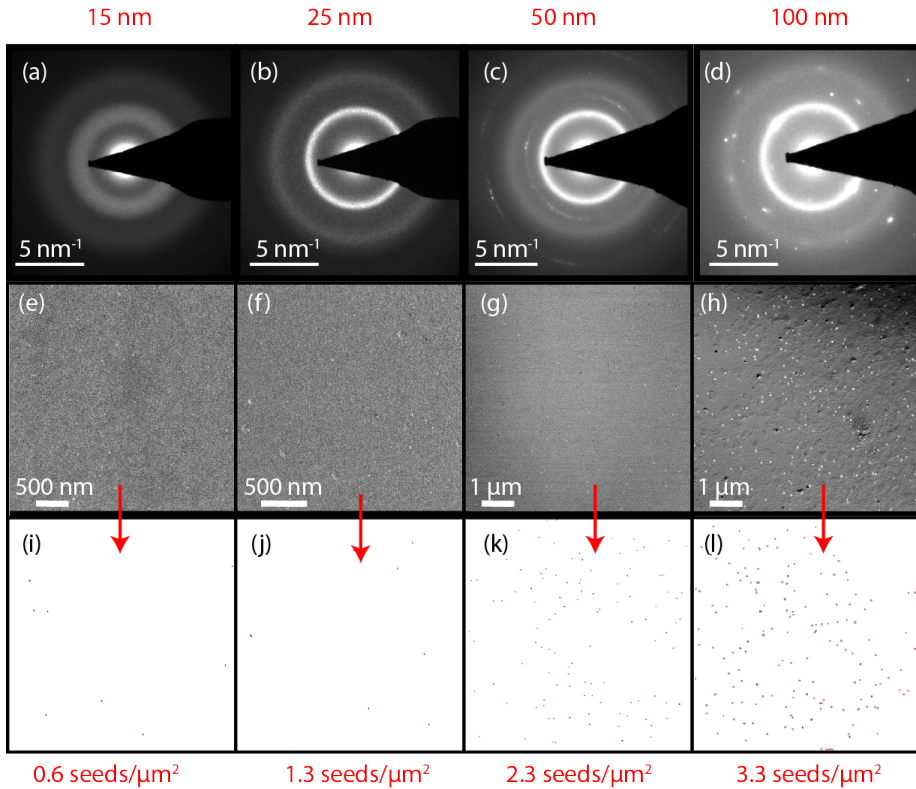
Figure 6.1: Four IZrO as-deposited films with different thicknesses. Diffraction patterns in (a), (b), (c) and (d) indicates that an increasing amount of crystalline seeds are present in the films when the thickness increases. Top view STEM BF images (e), (f), (g) and (h) showing the small crystalline seeds dispersed in an otherwise amorphous matrix and corresponding images containing the outlined particles (i), (j), (k), (l) issuing from the segmentation analysis. A surface density is then calculated and the results are given in the bottom part of the figure.
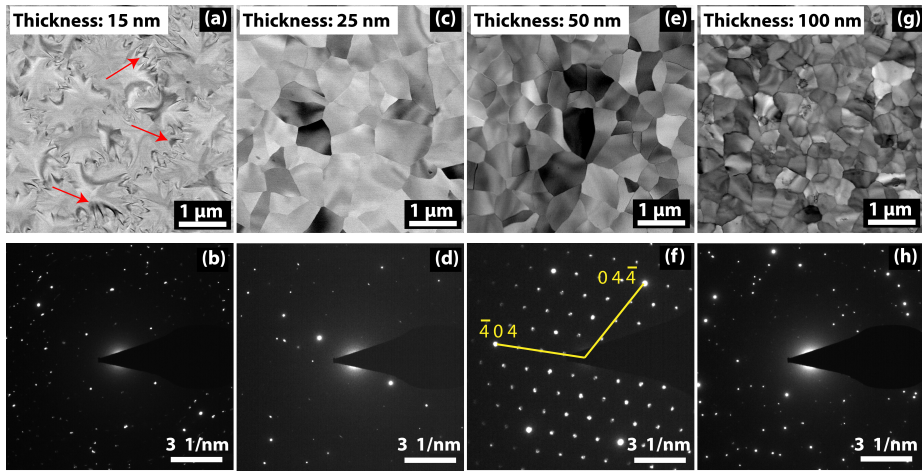
Figure 6.2: STEM BF top view of films of (a) 15 nm, (c) 25 nm, (e) 50 nm and (g) 100 nm thickness and selected area electron diffraction patterns respectively in (b), (d), (f) and (h). DP in (f) is obtained by selecting one single grain. 15 nm-thick films show a strained (bend contour indicated by red arrows) crystalline microstructure, while for thicker films, smaller crystallites are formed. The diffraction patterns were indexed with the software JEMS and all revealed a body-centered cubic structure (bixbyite-like structure [90]). An average crystallite sizes of 473 nm, 418 nm and 320 nm are found for 25 nm, 50 nm and 100 nm-thick films, respectively. All the samples are air annealed (200 °C for 30 minutes).

Figure 6.3: Areal density of crystalline seeds (blue) and crystalline grains (red) with respect to the film thickness. The calculation was conducted starting from the top views shown in Figures 6.1 and 6.2. Th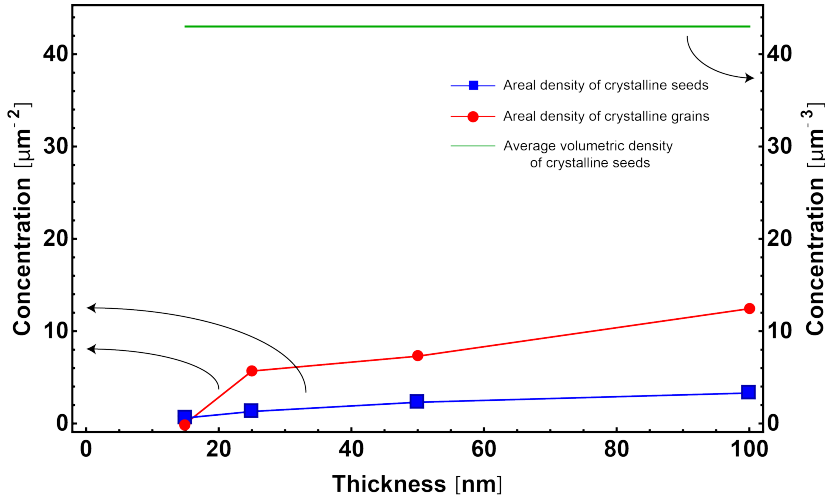e comparison is done with the calculated value of volumetric density (green), which is independent from the material thickness.

Compared to ZTO and SnO_2, IZrO crystallizes at much lower temperature during a post deposition annealing. The reason for this behavior is likely linked to the presence of crystalline seeds already in the as-deposited IZrO layers, as highlighted in Figure 6.1. These act as nucleation seeds that trigger the crystallization of the films. The fact that to a thicker sample is associated a smaller grain size depends on the presence of a higher concentration of crystalline seeds that develop to crystalline grains simultaneously and therefore compete in the space filling [193] [192]. From the previous observations it can be concluded that for what concerns the air annealing, IZrO appears to be crystalline with a grain size that decreases with increasing thickness of the sample. The number of grains per μm^2 was calculated for every top view in Figure 6.2 starting from the results of the average grain size and dividing the area of each grain for the total area of the image ($49\,\mu m^2$). The results (areal density of grains) are summarized in a graph (Figure 6.3) together with the areal density of crystalline seeds and the volumetric density of seeds calculated before. The number of crystalline grains is expected to be equal to the number of seeds, since the former originates from the latter. As explained previously, the variation between the density of crystalline seeds and crystalline grains is related to the image formation in a bright and dark field STEM configuration. The particles with high contrast are only a fraction of the total number of particles in the films. Moreover, the poor statistics of these calculation can also have an influence on the final numbers, nevertheless the observed trend is the same in both cases.
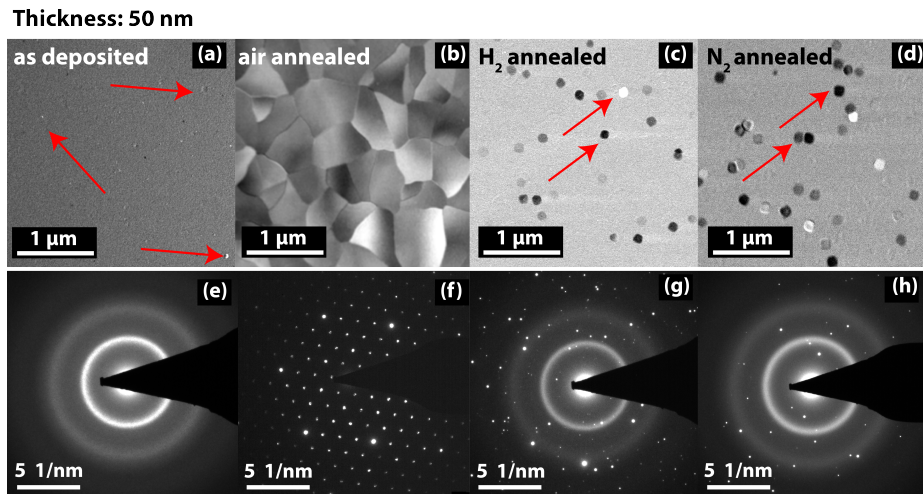
Thickness: 50 nm

Figure 6.4: STEM DF images of 50 nm-thick IZrO samples as-deposited (a), annealed in air (b), hydrogen (c) and nitrogen (d), for 30 minutes at 200 °C. Red arrows indicate the crystallites appearing in an otherwise amorphous structure and having different sizes based on the thermal treatment. The related diffraction patterns indicate an amorphous material (e), a completely crystalline one (f) and a material with an amorphous matrix in which are dispersed few crystallites (g) and (h).

As introduced before in the section, nitrogen and hydrogen annealing were conducted together with air annealing and the samples analyzed by TEM. Figure 6.4 displays the STEM images and related diffraction patterns of IZrO samples 50 nm-thick in the as-deposited state and annealed in air, hydrogen and nitrogen. Whereas air annealing completely transforms the material from amorphous to crystalline, hydrogen or nitrogen annealing are able to slightly increase the size of crystallites already present in the as-deposited sample. These results retrace the ones obtained for tin-based TCOs, were the annealing in an oxygen-rich atmosphere promotes the adsorption of oxygen from the environment, passivating the defects, which, in turn, stimulates the formation of stoichiometric SnO_2 and therefore the crystallization. In the present case a slower In_2O_3 crystallization is observed in the absence of O_2. As for ZTO, the films interact with the oxygen from the atmosphere, likely forming a more stoichiometric phase with less point defects. Interestingly, an oxygen-rich atmosphere not only promotes the formation of the first seeds (as observed for ZTO) but also promotes grain growth (IZrO). Moreover, little to no difference is observed when the annealing is conducted in nitrogen or hydrogen, since the grain size and shape appear to be the same. Nevertheless a systematic count of the number of crystallites dispersed in the structure was made in order to verify if any difference was present between different atmosphere annealing and the number of small grains was found to be
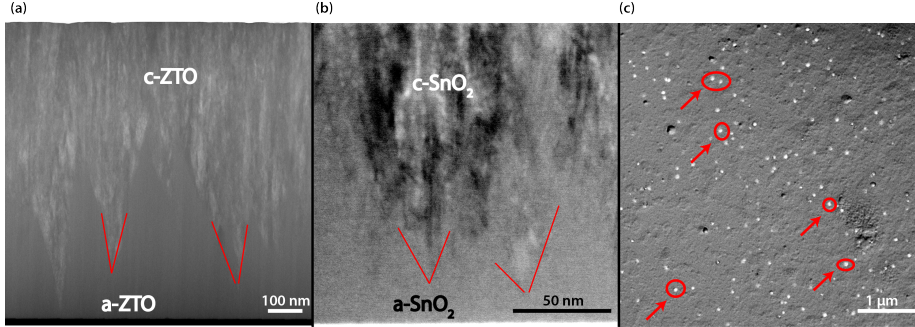
Figure 6.5: (a) TEM DF cross-section image of an as-deposited 1 μm-thick ZTO sample with the amorphous phase on the bottom of the sample and the crystallized one on top of it. (b) STEM BF cross-section image of as-deposited 150 nm-thick SnO$_2$ showing the conical crystals similar to the ones in (a). (c) STEM BF top view of an as-deposited 100 nm-thick IZrO sample showing crystalline seeds (red arrows) embedded in an amorphous matrix.

equivalent to the number of crystalline seeds already present in the as-deposited samples.

6.3 Discussion

The results on zirconium doped indium oxide illustrated in the previous section are compared in this section to the results already discussed in Chapter 4 on pure tin oxide and zinc tin oxide, in order to propose a growth model for the two materials. The first parameter being analyzed is the crystallization kinetics of both IZrO and ZTO/SnO$_2$ with respect to the material thickness. Figure 6.5 shows two cross-sections and one top view of a thick ZTO (1 μm), 150 nm-thick SnO$_2$ and 100 nm-thick IZrO. While ZTO and SnO$_2$ crystallize with the appearance of conical-shaped grains, IZrO presents crystalline seeds dispersed in an amorphous matrix.

The kinetic states of adatoms at the sample surface strongly influences its final structure. Venables *et al.* described the physical processes responsible for the crystal growth in thin films [194] [195]. Scheme in Figure 6.6 summarizes several mechanisms that can take place during deposition. Each of the mechanisms depicted in Figure 6.6 is characterized by a specific energy, such as the diffusion energy (E_d), re-evaporation energy (E_a) and the binding energy between atoms, which controls the nucleation (E_i). The thermodynamic system needs to be in a non equilibrium kinetic state in order to achieve a phase transformation. More
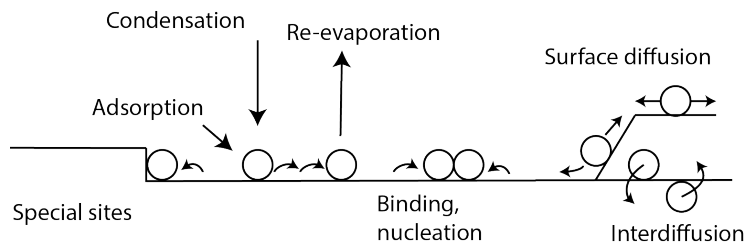
Figure 6.6: Schematic representation of processes taking place during film growth (adapted from [194])

generally, the phase transition phenomenon can be explained with Ostwald's rule of stages, which predicts the evolution of film growth to advance through a set of phases from the meta-stable to the more stable ones, as Birkholz *et al.* [196] proved for thin silicon films deposited by chemical vapor deposition. Moreover, it is proven that Ostwald's rule of stages minimizes the production of entropy [197]. Nevertheless, it is not the more stable state that is initially created during a reaction, but the one being characterized by a free energy value similar to the original state. For a deposition method that does not imply any liquid solutions, the mechanisms governing the amorphous-to-crystalline transition are the *kinetic limitation*, the *interfacial mixing* and the *thermodynamic stability* [198].

Several studies identify different parameters as the cause for the amorphous-to-crystalline transition, Buchholz *et al.* [90] presented a series of experiments where the deposition temperature was varied and the studied TCO changed from amorphous to crystalline with the temperature increase. A similarity is found in the growth behavior of tin-based TCOs and amorphous silicon [117]. When a certain thickness threshold is crossed, the crystalline phase tends to grow faster than the amorphous one. In Chapter 4 the speed of growth of the crystalline phase in ZTO and SnO_2 was calculated and it was confirmed to be larger than the amorphous phase growth speed. Teplin *et al.* confirmed that the variety of relative growth speeds between amorphous and poly-crystalline phases is related to the deposition parameters and type of substrate. Figure 6.7 shows the scheme representing different growing phases in the case of amorphous substrate. Depending on where on the graph the deposition is situated, the amorphous phase is preferred over the crystalline one and vice versa. In the case of amorphous substrate, as soon as the nucleation rate increases, new crystalline seeds are embedded in the amorphous matrix and are transformed into poly crystalline cones as soon as the relative growth rate increases. Whereas for a fixed nucleation rate, if the crystalline phase grows at higher speed with respect to the amorphous one, poly-crystalline cones start to appear. The formation of conical shaped crystals is generally associated to growth kinetics at the surface
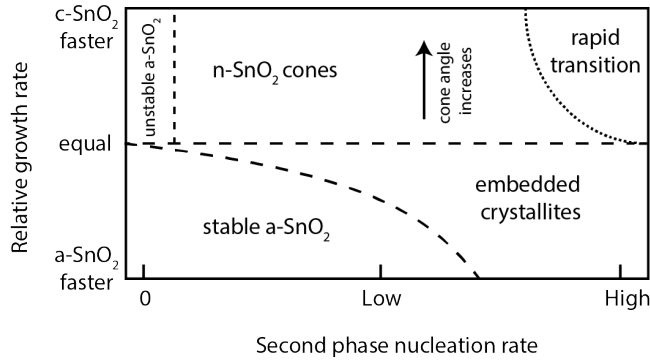
Figure 6.7: Scheme of deposition phase space on amorphous substrate, showing the growth rate with respect to the probability of nucleation for the second phase appearing in the material. The dashed lines separate different growth regimes. Adapted image from [117].

of the material during deposition [199] [200] rather than being a bulk-related process. For both ZTO and IZrO, the first meta-stable phase that appears is the amorphous one. Starting from a certain thickness, probably linked to film constraints and deposition parameters, a nucleation seed is formed. However, whereas in ZTO (and SnO_2) the crystalline phase appears immediately after the nucleation, in IZrO the crystalline nuclei remain embedded in the amorphous matrix. The growth speed related to the amorphous or crystalline phase is influenced by several parameters, such as the plasma power in the deposition chamber, substrate temperature or the partial pressure of the deposition gasses.

Tsai *et al.* hypothesized that hydrogen has a fundamental role in the growth mechanisms of amorphous and polycrystalline silicon [201]. In particular, hydrogen might etch the growth surface and promote the formation of crystalline seeds over amorphous silicon. Indeed, hydrogen is found to etch amorphous silicon five to ten times faster with respect to micro-crystalline silicon [202]. Evidences of the presence of hydrogen desorbing from ZTO samples were found during TDS experiments (see Chapter 4). ZTO and SnO_2 grow following the same crystallization mechanisms as for silicon. The threshold thickness is different for the two materials and in particular $t \geq 40$ nm for SnO_2 whereas $t \geq 150$ nm for ZTO. Since the chemical concentration of the targets in the deposition chamber is in one case stoichiometric SnO_2 and in the other $Zn_{0.0049}Sn_{0.299}O_{0.652}$, the only possible re-arrangement of the amorphous phase in a crystalline one is by forming SnO_2 crystalline seeds, as confirmed by XRD experiments. The presence of zinc delays the formation of SnO_2 crystals in the ZTO matrix and therefore it postpones the crystallization of the material with respect to pure SnO_2.
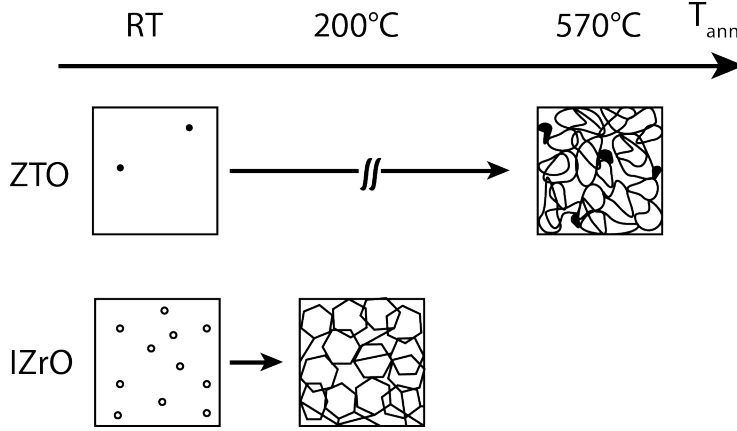
Figure 6.8: Evolution with respect to air annealing temperature of ZTO and IZrO. Because of the presence of crystalline seeds at room temperature, crystallization requires lower temperatures in the case of IZrO. Voids in ZTO structure are represented in pitch black.

On the other hand, Koida *et al.* assessed how the introduction of water into the deposition chamber prevents crystal growth [203]. The reason is ascribed to the formation of In-OH bonds, which impedes the formation of In-O-In bonds.

With respect to the annealing temperature, in Chapter 4 it was proven, from the XRD data that ZTO (and SnO_2) requires more energy (higher annealing temperature) in order to crystallize, whereas IZrO needs less energy (lower annealing temperature) to transition from its amorphous to the crystalline phase. Figure 6.8 shows a schematic representation of the two cases. The reason for this energy difference is to be ascribed to the higher concentration of crystalline seeds in IZrO than in ZTO. Indeed, it is energetically more expensive to create critical size seeds than to grow already existing ones [204]. The energy nucleation barrier, E_n, is higher in ZTO than in IZrO and is not passed in the case of ZTO until the temperature reaches values around 600 °C. Khawam *et al.* [205] described how a single step nucleation can be expressed by different laws depending on the nucleation rate K_N: the higher the nucleation rate, the faster the phase change process. In the case of IZrO, a linear trend seems to be the most appropriate way to describe the formation of new crystalline seeds (Figure 6.3). On the other hand, ZTO and SnO_2 are characterized by an abrupt crystallization, as seen from XRD analysis, therefore an exponential law is more appropriate. The phase change in ZTO and SnO_2 is limited by the nucleation. Once the the nucleation energy barrier is crossed in ZTO and SnO_2, the grain growth is abrupt. This phenomenon is also abrupt in the case of IZrO, but the energy required for the grain growth is lower than in the case of tin-based TCOs,

since the nucleation already happened. Figure A.8 summarizes the crystallization process for ZTO and IZrO. As already introduced, in the case of ZTO the crystallization is a nucleation controlled process. Indeed, since the formation rate of crystalline seeds during deposition is low due to the material chemistry and deposition atmosphere, a high annealing temperature is required in order to overcome the energy barrier required for the first nuclei to form. Once these nuclei are formed, the material is abruptly submitted to a phase change. Many authors [206] [207] [208] have highlighted how the grain size evolution follows the Ostwald's ripening with increasing annealing temperature, *i.e.* bigger grains tend to incorporate smaller ones in order to minimize the free surface and interface energies [192]. In the case of ZTO and SnO_2, as highlighted by XRD experiments, grains continue to grow at the expense of the amorphous phase. When the temperature increases ($\simeq 700\,°C$), ZTO starts to decompose and zinc evaporates from the film, leaving a deficient structure.

IZrO, on the other hand, presents a constant nucleation rate, which depends on the deposition conditions and most likely to the ability of hydrogen (present in the deposition chamber) to form In-OH bonds and preventing the formation of In-O-In ones. When submitted to annealings, a lower temperature with respect to ZTO is required in order to fully crystallize IZrO. This is due to the fact that growing already existing seeds into crystalline grains costs less energy than creating new seeds. Indeed Koida *et al.* [191] reported that in hydrogen doped indium oxide despite high annealing temperatures (in vacuum, in the specific case), no new crystalline nuclei appeared in the film. In the same study, high resolution TEM observation of the grain boundaries highlighted sharp interfaces, which indicates that the grain boundaries are perpendicular to the sample surface. These observation is in accordance with our results on IZrO. In our case, the crystal size appears to be independent from the annealing temperature (at least up to 200 °C) and only depends on the number of seeds already present in the as-deposited state. Annealing experiments to high temperatures are needed in order to draw a conclusion on IZrO, nevertheless, Koida *et al.* [203] found that for IO:H films, the grain size continue to increase as the annealing temperature exceeds 150 °C.

One last parameter that strongly influence both the nucleation in ZTO and the grain growth in IZrO, is the oxygen concentration in the annealing atmosphere. As confirmed by XRD air and vacuum annealings on ZTO (Chapter 4) and by a similar experiments on In_2O_3:H conducted by Koida *et al.* [191], when the annealing atmosphere is oxygen-rich, the phase change is promoted and happens faster (at lower temperatures) with respect to when the same experiment is conducted in vacuum. The reason is likely to be linked to the fact that as-deposited materials are oxygen deficient because of the presence of oxygen vacancies, hence, in order to form a final stoichiometric crystalline material, oxygen has to enter into the structure.

Electrical and optical properties of IZrO were investigated as well and for the annealed samples, the conductivity decreases from $4200 \, \mathrm{S \, cm^{-1}}$ for the 100 nm-thick sample down to $400 \, \mathrm{S \, cm^{-1}}$ for the 15 nm-thick one, the latter exhibits the typical glass transparency, while keeping a mobility of $50 \, \mathrm{cm \, V^{-2} \, s^{-1}}$ and a carrier concentration of $5 \times 10^{19} \, \mathrm{cm^{-3}}$. Therefore this material allows to use less indium with respect to the standard indium-based materials while it ensures high transparency and electrical conductivity [Thesis of Esteban Rucavado].

6.4   Conclusion

In this chapter the crystallization mechanisms in tin based and indium based TCOs was described with respect to material thickness and annealing temperature. The material chemistry and deposition atmosphere are crucial parameters that decide what kind of reactions take place during growth. A combination of TEM, XRD and theoretical studies were used in order to propose a model. The different chemistry and stoichiometry of TCOs act as limiting factor for the material growth. Indeed, tin-based TCOs are deposited mainly amorphous because of the high energy barrier linked to the nucleation of the material. When a certain thickness is reached, the material crystallizes in conical-shaped grains with random orientation. This phenomenon is linked to the fact that the crystalline phase is more stable than the amorphous one and tends to have higher growth speeds. When the material is submitted to high temperature treatments, The nucleation energy barrier is crossed and the crystallization is abrupt with no preferential orientation. The grain growth proceeds up to when the amorphous fraction of the material completely disappears.

In zirconium doped indium oxide, a constant nucleation is observed instead, due to the presence of hydrogen in the deposition chambers, which prevents the formation of In-O-In bonds. Therefore the formation of conical shaped grains is not observed up to the analyzed thicknesses. When submitted to thermal treatments, a temperature of $200 \, \mathrm{°C}$ is sufficient to trigger the phase change. The grain size is found to only depend on the number of crystalline seeds already present in the material in its as-deposited state. Annealings at higher temperatures are needed in order to assess if the grains obey to the Ostwald's ripening type of growth.
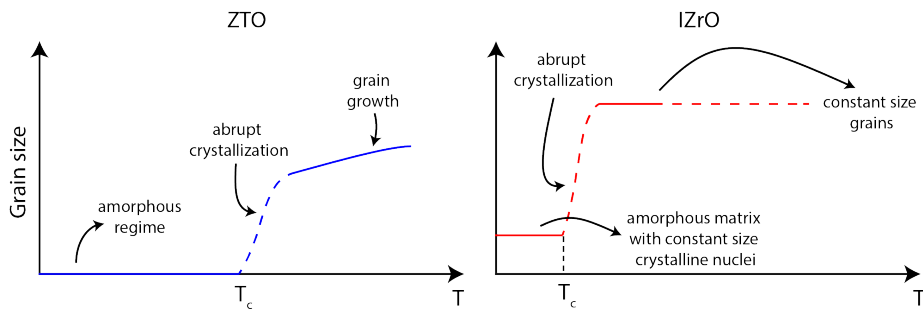
Figure 6.9: Scheme of the crystallization process in ZTO and IZrO. In ZTO crystallization is abrupt and takes place from an overall amorphous material. A high temperature is needed in order to overcome the nucleation energy barrier, which, once crossed, translates in the material phase change. In IZrO, since critical crystalline seeds are present in the as-deposited structure, a lower temperature is sufficient in order to start the grain growth. Solid lines represent the experimentally observed parts of the reaction, whereas dashed lines represent hypothesis based on the previous and following steps observations.

CHAPTER 7

Conclusions and Outlook

In this project, the opto-electronic and microstructural properties of tin-based TCOs were investigated in depth, in order to understand the physical mechanisms that lead to the observed properties of this class of materials. The urgency for indium-free materials is due to the future projections on the availability and always raising price of indium. In particular, the high demand of photovoltaic-related materials, flat screens, OLEDs and electronics are among the causes that make indium more and more scarce. This justifies the need to substitute indium-based with other materials, which can assure the same performances at a lower price and using earth abundant elements. The focus of this work was put on tin-based TCOs and their electrical stability upon thermal treatments was investigated. Many applications require a high temperature operation of these materials, that do not have to be degraded by these treatments. A combination of several techniques, such as TEM, XRD, EPR and many more, was used to decouple the physical effects determining the material behavior in each temperature regime for ZTO and SnO_2. The study of electrical mobility and carrier concentration with respect to air annealing temperature revealed three different regimes for ZTO electrical properties. Between room temperature and 300 °C, the increase in both μ and N (observed even in hydrogen and nitrogen annealing) was ascribed to a structural relaxation of the amorphous matrix with the consequent release in conduction band of free carriers originated in point defects of the structure. This structural relaxation was confirmed by differential scanning calorimetry and the data compared to the existing literature. Never-

theless, since standard DSC was used for the analysis of thin films, in order for the results to be highly reproducible, nano-DSC should be used, this being a more suitable technique for samples having a mass in the range of micrograms. Moreover, the surface effect observed in Chapter 5 is to be further investigated. In the second temperature regime (between $300\,°C$ and $500\,°C$), the observed decrease in N and increase in μ were associated to the passivation of oxygen vacancies, which are the main source of charge carriers in these types of materials, which then led to the final drop in N and the subsequent crystallization of the material ($570\,°C$). ZTO was submitted to electron paramagnetic resonance experiments in order to check the actual amount of paramagnetic defects in the material and to better understand their origin. Indeed, it was confirmed that the defects are related to oxygen vacancies and that their concentration decreases before the crystallization threshold is crossed. Once the ZTO crystallizes, XRD confirmed that a rutile phase of a completely insulating SnO_2 is formed and as soon as the temperature is increased up to $1050\,°C$, zinc is almost completely evaporated from the samples (confirmed by EDX analysis). The role of zinc was investigated by submitting and analyzing SnO_2 samples to the same annealing ZTO was submitted to. Pure tin oxide was found to crystallize $\simeq300\,°C$ lower with respect to ZTO. Many studies assessed that even a small addition of zinc to tin-based or indium-based TCOs are able to shift the crystallization threshold towards higher temperatures, probably because of some local stress induced in the unit cell because of the presence of zinc atoms. Our XRD analysis revealed a unit cell with one of the rutile lattice constants completely in agreement with the literature values and the other one 5% smaller than the theoretical value.

Because of the drop in electrical conductivity at the crystallization temperature, a doping strategy was studied in order to promote the creation of free-carriers and possibly recover the conductivity drop at high temperature. Using DFT calculations conducted by a partner group in Basel as a basis, two elements were selected as dopants: iodine and bromine. The exploratory experiments gave promising results especially when the starting material was deposited at room temperature. Unfortunately spin coated iodine and bromine revealed themselves to be highly volatile so that the chemical quantification via EDX was challenging and the quantities too low to conclude that any doping actually happened. Therefore as future perspective, adding these dopants in the ZTO matrix via co-sputtering, before any thermal treatment or spectroscopic analysis, is to be envisaged. On the other hand, the addition of silicon via co-sputtering in the ZTO matrix allowed to obtain the best possible ZTO without submitting it to high temperature treatments, since silicon oxide acts as passivating agent for the defects present in the ZTO. This addition results in a more transparent material.

Finally, by using an indium-based material as a benchmark, the crystallization mechanism of ZTO and SnO_2 was discussed. While ZTO and SnO_2 are found to

crystallize when a threshold thickness is reached, IZrO does not follow the same trend. This difference can be due to several parameters such as the material chemistry and deposition atmosphere. Hydrogen, in particular might etch the amorphous phase of IZrO and therefore promote the formation of critical size crystalline seeds. On the other hand, because of the re-organization of surface atoms and their low mobility, conical shaped crystal cannot develop. Annealing temperature also influences the crystallization in a way that it gives the sufficient amount of energy to the material in order for it to let the crystalline seeds grow, in the case of IZrO, and to overcome the nucleation barrier in the case of ZTO and SnO_2. Once the crystalline grains are formed, in the case of ZTO they continue to grow while the remaining amorphous portion of the films decreases, while in the case of IZrO, the grain size remains constant up to the investigated temperatures.

APPENDIX A

Appendix

A.1   Introduction

The appendix aims at giving more details about the accessory techniques that were used during the experimental analysis of TCOs that either did not give satisfactory results, and in this case the reason is investigated, or helped to understand process and phenomena that led to the results described in previous chapters. In particular, four subjects are addressed, Appendix A.2 describes the approach that was followed to deepen the knowledge regarding the oxidation states of zinc tin oxide using x-ray photoemission spectroscopy (XPS), in Appendix A.3 is the detailed explanation on how the number of paramagnetic defects was extracted from the EPR measurements; Appendix A.4 describes how the number of grains in indium zirconium oxide is calculated and finally, Appendix A.5 presents a detailed EDX analysis conducted for iodine and bromine doped ZTO samples.

A.2   X-ray photoemission spectroscopy

In chapter 4 the electrical properties of ZTO were presented and three regimes for mobility and carrier concentration were highlighted with respect to the air

annealing temperature. In order to understand if the change in electrical properties is due to the change in the oxidation state of ZTO, X-ray photoemission spectroscopy (XPS) was performed. From the analysis of XPS spectra, one is able to access the information about the local environment of an atomic species. The goal here is to understand in which oxidation state the oxygen, tin and zinc are within several ZTO samples treated differently and to determine if any link between the oxidation state and the electrical properties of the material can be made. In particular the main interest is in understanding if the chemical state of these species changes before and after crystallization, where a big change in the electrical properties is observed. It is known from the analysis of the state-of-the-art on tin-based TCOs that, for example, SnO is a known form of non-conductive tin oxide, therefore, XPS analysis is useful, among others, to perform a screening on the conductive structures of tin oxide. The same approach was used to study the oxidation state of oxygen, in order to understand if any difference in local bonding is found and if these differences can be linked to oxygen vacancies, or oxygen linked to tin as SnO, oxygen linked to tin as SnO_2, or oxygen linked to zinc as ZnO. This is the reason why in order to fit the curves, a combination of gaussians, described further in the code, [209] [210] was used. Theoretically, all of these oxidation states can be present at once in our material. Oxidation state is useful to identify which are the nearest neighbors of an atomic species, so given the theoretical binding energy of a species, small shifts, so-called chemical shifts, from this theoretical energy, will provide the chemical state information [211].

A.2.1 Experimental details and data treatment

X-ray photoemission spectroscopy is a quantitative spectroscopic technique that allows the measurement of the chemical and electronic state of elements in a compound. The working principle of this technique is based on the detection of electrons ejected from the material and the measurement of their kinetic energy (binding energy). The material is irradiated with x-rays, this radiation has a non-zero probability to eject an electron by photoelectric effect if its energy is bigger than the electron binding energy plus the work function of the material (since the electron has to reach the vacuum energy level). The energy of ejected electrons is measured and therefore the binding energy can be calculated as follows

$$E_{\text{binding}} = E_{\text{photon}} - (E_{\text{kinetic}} + \phi) \qquad (A.1)$$

where E_{binding} is the binding energy of the electron, E_{kinetic} is the electron energy as measured by the instrument and ϕ is the work function, which is dependent on both the spectrometer and the material. XPS is a surface sensitive technique that can measure chemical compositions at the parts per thousand range and it requires the sample to be inserted in a high vacuum chamber in

order to be measured ($P \simeq 10^{-8}$ mbar). If the binding energy of a particular atom is known, constant shifts from this energy can be associated to a different local environment of the atom and therefore give information about its chemical state. The core binding energies are determined by the electrostatic interactions between the electron and the nucleus and can be reduced by the shielding effect of the nuclear charge from other electrons in the cloud. Since it is a surface technique, depth profiles were studied. In order to analyze the material in all its depth, an ion milling is needed to sputter away the first layers of the sample. In our case argon ions were used for the sputtering with a pace of 12 nm of sputtered material per minute. One spectrum per each depth is registered and the measurement was stopped when the substrate (silicon wafer) was hit. XPS measurements were carried out using a PHI VersaProbe II scanning XPS microprobe (Physical Instruments AG, Germany) in the Molecular and Hybrid Materials Characterization Center (MHMC) at EPFL and with the help of the scientific collaborator Pierre Mettraux. The analysis were performed using a monochromatic Al Kα X-ray source of 24.8 W power with a beam size of 100 μm. Seven samples were analyzed: the as-deposited together with air annealed at 300 °C, 500 °C, 550 °C, 650 °C and vacuum annealed at 900 °C and 1050 °C. All the samples were annealed *in situ* in the XRD. Instead of using the standard software (PHI Multipak software) to do the curve fitting, a Mathematica notebook was specifically written and the main steps are described below:

- plotting the spectra (binding energies) of the different edges;

- re-alignment of the peaks in case some shifts happen during the experiments. This is done by pre-aligning the carbon 1s binding energy to its theoretical value and therefore re-aligning all the peaks accordingly;

- subtraction of the background and normalization of the curves;

- the oxygen 1s edge, tin $3_{d_{3/2}}$ and $3_{d_{5/2}}$ edges and zinc $2_{p_{1/2}}$ and $2_{p_{3/2}}$ edges are considered in the fitting;

- after a first test with different fitting models, a non-linear model was chosen, with a combination of gaussians, each gaussian being centered at a specific binding energy representing one oxidation state;

- the goodness of the fitting is extracted using standard parameters such as the R squared value;

- the results are plotted in graphs.

As mentioned in the description of the code, three different types of fitting were tried during the data treatment, with the goal of progressively improve the output. In particular, a single gaussian was first chosen in order to test

the goodness of the fitting. The second model, involving a linear combination of two to three gaussians was then chosen. The third model was a nonlinear combination of gaussians. For this last fitting the parameters were left free to change within a certain range or fixed. The theoretical binding energies of the investigated elements were chosen within the NIST database. It is worth to mention here that some sort of overlap between different oxidation states does exist in literature, this leads to the difficult task of deciding if a binding energy corresponds to one oxidation state or another. A typical example can be made looking at the binding energies of tin when it is linked to oxygen: the corresponding energy for SnO are between 486 eV and 486.9 eV; the energies for SnO_2 are between 486.5 eV and 486.9 eV. So there is a clear overlap between them. In the following section the main results are described.

A.2.2   Results and discussion

As a first attempt, a single gaussian was used to describe the experimental curves obtained from the XPS analysis and to understand how good this description is. In particular a model with a gaussian curve was introduced

$$f\left(x\right) = \frac{e^{-\frac{(x-a)^2}{2b^2}}}{\sqrt{2\pi}b} \tag{A.2}$$

and parameters which were free to assume any value. Where a is the expected value and b^2 the variance. The result is shown for the oxygen binding energy in Figure A.1(a). It is clearly visible that this model does not represent well the experimental points, therefore, a combination of two gaussian was used, with the additional constraint that the expected values have to vary within the ranges found in the NIST database (Figure A.1(b)). The result curve describes well the experimental points, therefore, in order to discover the amount of oxygen linked to tin as SnO and SnO_2, a calculation was carried out using the area under each curve. The output is plotted in Figure A.2. When a nonlinear model with an additional background subtraction is applied to the experimental data (Figure A.1(c)), the results appear to be fundamentally different from those treated with the linear model. In the case of the tin edge fitting, three gaussians were inserted in the model: one representing tin linked to oxygen as SnO_2, a second to represent tin linked to oxygen as SnO and the third one for metallic tin, since tin atom clusters are expected from theoretical simulations. Figure A.3 shows the result extracted from the nonlinear fitting for the case of tin. It is interesting to compare the behavior of the oxygen edge obtained with the first fitting method and the last one. Figure A.4 shows the percentage of oxygen linked to tin as SnO_2 and SnO obtained with the nonlinear model. These results are fundamentally different from the ones shown in Figure A.2. Indeed, the fitting of XPS tin edges is particularly difficult because of the overlap in
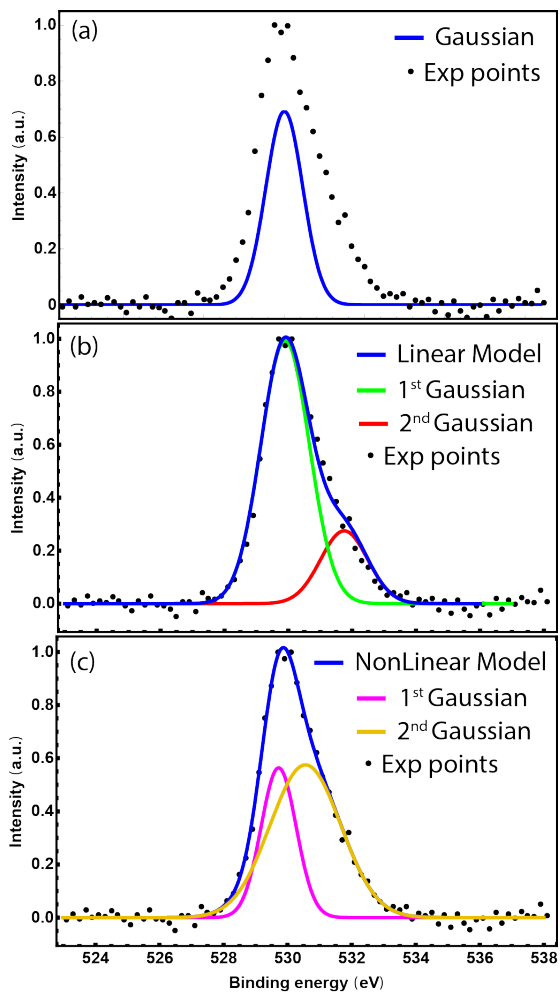
Figure A.1: Experimental points and fitting curve using (a) a single gaussian for the oxygen $1s$ edge binding energy, (b) a linear combination and (c) a non linear combination of two gaussian.
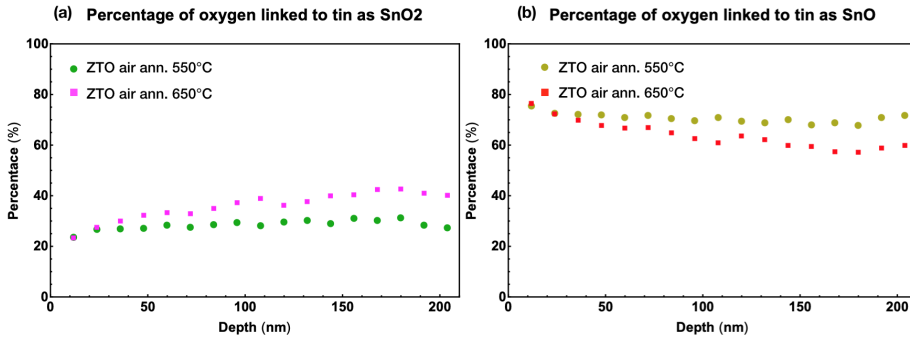
Figure A.2: Percentage of oxygen linked to tin as SnO_2 (a) and SnO (b) for ZTO samples annealed in air, before and after crystallization, using the linear model. From this figure it seems that the amount of oxygen linked to tin as SnO in ZTO is higher than the concentration of SnO_2 either before and after crystallization.

Figure A.3: Percentage of tin present in the ZTO as metallic tin (a), tin linked to oxygen as SnO (b) and tin linked to oxygen as SnO_2 (c). These calculation was done using a nonlinear model. No important change is registered before and after crystallization.
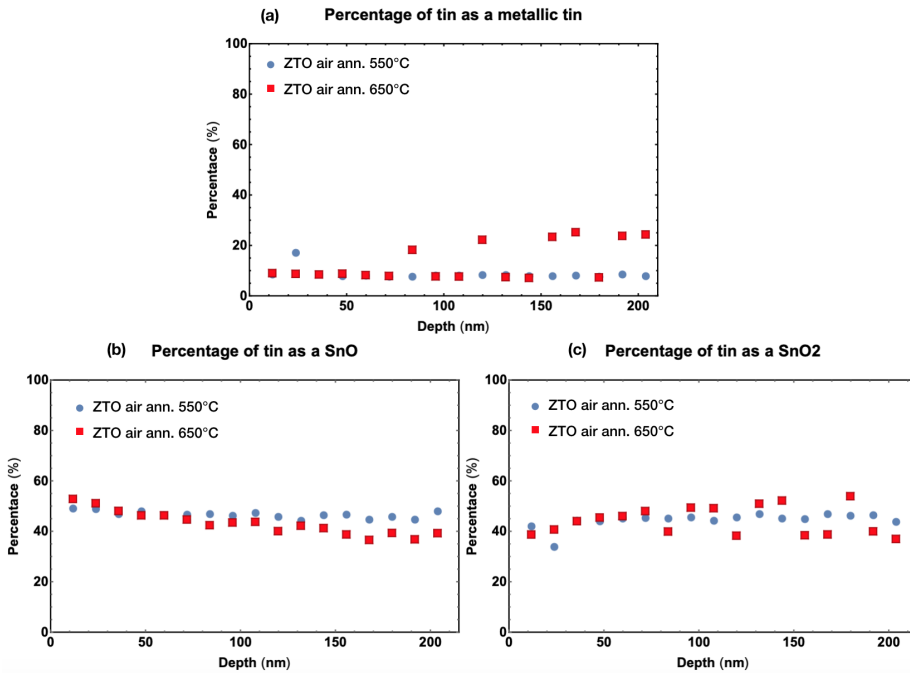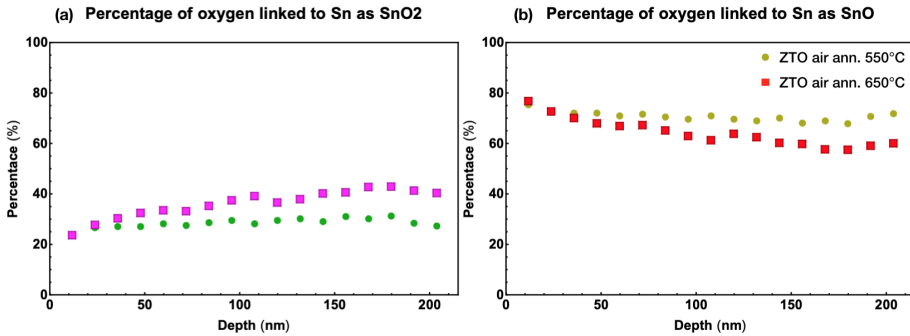
Figure A.4: Percentage of tin linked to oxygen as SnO_2 (a) and tin linked to oxygen as SnO (b) before and after crystallization in air. Calculation done using the nonlinear model. Contrary to figure A.2, no important variation is found before and after crystallization.

binding energy between SnO_2 and SnO. The results are extremely dependent on the fitting method and especially on the fitting parameters, so that a small variation of a and b values alter completely the final result, even when the goodness of the fitting was calculated and reached high values. Moreover, from XRD and EDX analysis, no SnO phases, nor metal clustering were identified.

Conclusion on XPS analysis As seen from the previous analysis, the content of different tin and zinc phases are strongly dependent on what type of model is chosen and more importantly on the parameter values. Three different types of fitting have been tried during this data treatment, in particular, a single gaussian was first chosen in order to test the goodness of the fitting, not leading to a good fit of experimental data, then a second model, involving a linear combination of two or three gaussians was used. The fitting represents well the experimental curves but leads to rather surprising results. The third model was a nonlinear combination of gaussians. For this last fitting the parameters were left free to change within a certain range or fixed. The results were totally dependent on the choice of these parameters. The NIST database suggests that the binding energy related to a particular oxidation state is not unique but it rather oscillates in a range of values. The difficult problem to overcome is that these ranges usually overlap, making the distinction between one oxidation state and another, in the majority of the cases, really difficult. XRD experiments were used as a comparison for the previous results. The dominant phase resulted to be SnO_2 with no evidence of SnO presence nor ZnO related phases. This confirms that analyzing XPS data is a difficult task because of the overlap between binding energies and therefore not reliable to distinguish SnO_2

from SnO. Nevertheless, this investigation helped to put the XPS literature on tin oxide in perspective.

A.3   Spin count procedure in Electron Paramagnetic Resonance

In order to extract the exact numbers of spins from the EPR spectrum, the following procedure was applied. As highlighted in the theoretical part dedicated to this technique (Chapter 3), a first tuning procedure to adjust the microwave frequency is needed. Figure A.5 (a) shows a graphical representation of this procedure applied in the case of the 150 nm-thick, as-deposited sample. The
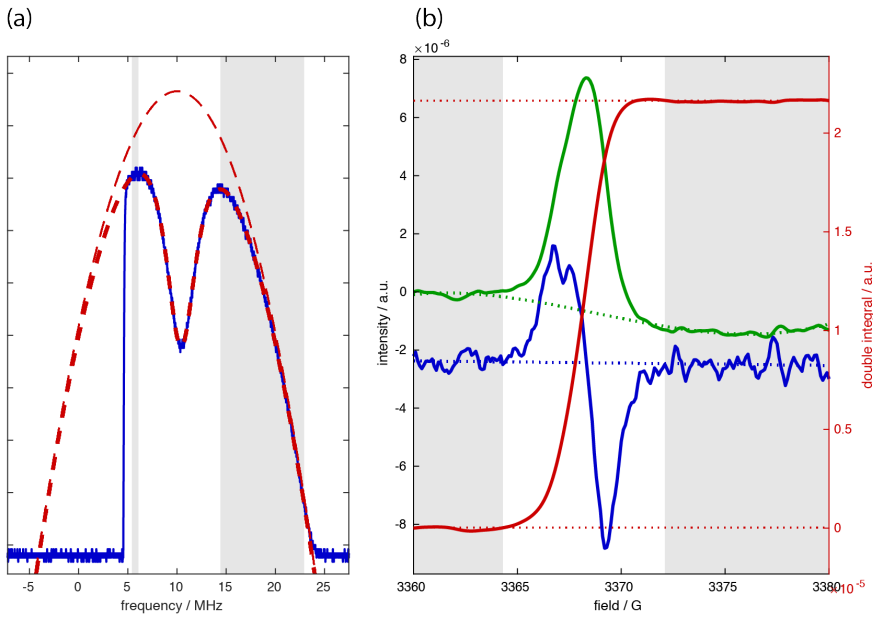
Figure A.5: (a) fine tuning of the microwave frequency around 9.6 GHz showing the theoretical shape of the microwave power with no absorption (red dashed) and the actual one (blue), where the dip represents the absorbed frequency by the resonator. (b) first integral (green) and second integral (red) of the EPR signal (blue). The second integral is the quantity needed to extract an actual spin count.

resonance frequency for the used equipment when the sample is inserted into the resonator is around 9.6 GHz. The graph in figure A.5 (a) shows the procedure to center the actual microwave frequency to the resonance one. The x-axis, showing the frequency expressed in megahertz, signifies that it is a fine tuning and that the actual frequency is swept across a range of $\simeq$ 30 MHz, *i.e.* the real frequency can be expressed as $\nu =$ 9.6 GHz $\pm$ 15 MHz. The red dashed curve represents the shape that the microwave source (Klystron) should have without

any absorption, whereas the blue one is the real shape of the microwave energy with the resonator absorption (dip). This curve should be symmetric, as the red dashed line indicates, but it presents a sharp vertical edge to its left. This is due to the fact the the Klystron has a threshold energy. By determining the full width at half maximum (FWHM) of the dip, the bandwidth can be calculated and therefore the quality factor Q of the loaded resonator can be calculated. Q is indeed obtained by dividing the main frequency by the width of the dip. Since the presence of the sample can influence and modify the resonance frequency, for all the measurements shown in this work, the spectra were normalized to 9.6 GHz, *i.e.*, if the frequency is found to be equal to 9.4 GHz, the spectrum is divided by 9.4 GHz and multiplied for 9.6 GHz in order align all the spectra at the same resonant magnetic field.

The graph in Figure A.5(b) represents the actual calculation of the double integral, which is fundamental to then extract the actual spin count though the formula already mentioned in chapter 3 and reminded here:

$$N = \frac{I}{C_f \left(\sqrt{P_m} B_{\text{mod}} Q n_B S \left(S + 1 \right) \right)} \tag{A.3}$$

where I is the double integral, C_f the calibration factor, P_m the microwave power, B_{mod} the field modulation strength, n_B the Boltzmann population difference for a spin state equilibrium at a certain temperature and microwave frequency, Q the quality factor of the cavity and $S = 1/2$ for a doublet state [115] [116]. The blue curve in Figure A.5(b) is the derivative of the actual microwave absorption signal, which is measured because of the magnetic field modulation in cwEPR. The green curve is its first integral and the red one is its second integral, which represents the area under the green curve. The second integral is indeed the quantity I that needs to be plugged in the aforementioned formula. The calibration factor (or transfer factor) C_f is the factor that allows to translate the double integral quantity in the actual number of spins. The temperature at which the measurement is conducted is taken into account by n_B, the Boltzmann population difference between the ground state and the first excited state. The field modulation strength B_{mod} in our case was equal to 100 μT.

The grey regions highlighted in Figure A.5(b) are the ones chosen to fit the background of the plot. Generally, the background is fitted using a polinomial function of the third order and it depends on the data points in this region. The choice of the background depends on the signal-to-noise ratio of the measurement itself and on the knowledge about the signal shape. A noisy acquisition makes a proper selection of the background more complicated to ensure that just signal and not background is taken into account. The toolbox used for the spincounting and developed by Dr. Engelhard can be found here: `https://github.com/lcts/spincounting`. One could further increase the ac-

cumulation time and increase the signal to noise ratio but this would increase tremendously the acquisition time. In our case the error is estimated to be around $\pm 10^{11}$ spins.
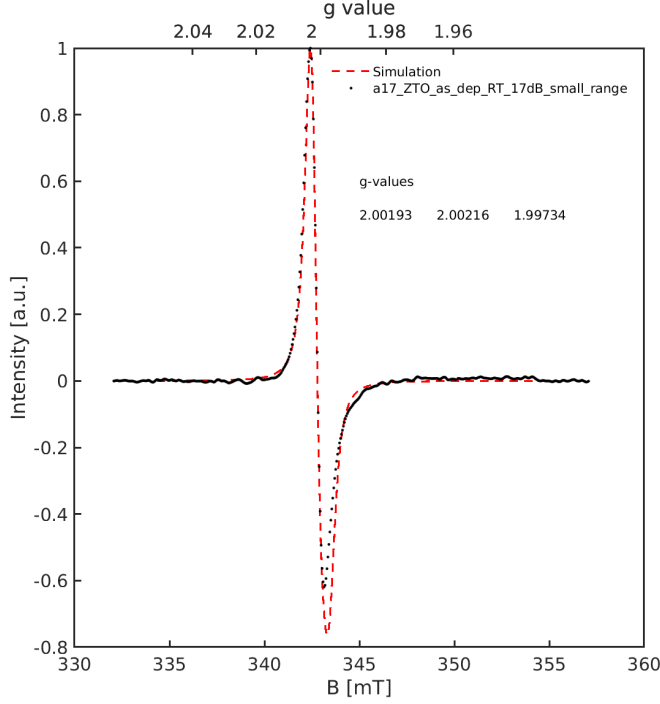
Figure A.6: EPR signal and relative fitting that allows to extract the g-value for a particular defect.

Figure A.6 plots the actual EPR signal for the as-deposited sample 150 nm-thick and the related simulation conducted in order to extract the g-value. The simulations are performed to allocate the signal to defects in ZTO. This can be done by knowing their EPR fingerprint, i.e. the g-values. The magnetic field axis was determined by a Bruker NMR-Gaussmeter and was calibrated by a Nitrogen encapsulated in $C_6 0$ reference sample with a very well known g-value. The simulation was performed by using the easyspin [212] toolbox for Matlab. The fact that the curve is non-symmetric indicates that the g-value can be split in its three different components: g_x, g_y and g_z. The simulation suggest a nearly axial g-matrix with the principle values of 2.0015, 2.0002, 1.9999.

A.4 Counts of IZrO grains from TEM to view images

The grain size for annealed IZrO samples in Chapter 6 was calculated using the following formula

$$L = \frac{L_0}{N} \tag{A.4}$$

where L is the average grain size, L_0 is the length of the lines traced across the investigated area and N is the number of grains that one of these lines crosses (Figure A.7). The error was calculated by taking the standard deviation and the results are shown in Table A.1.

Table A.1: Grain size calculated for three different thicknesses of IZrO samples.

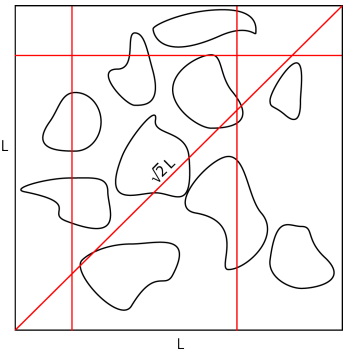| Thickness (nm)	Grain size $\pm\sigma$ (nm)
25	(473 ± 43)
50	(418 ± 50)
100	(320 ± 15)

Figure A.7: Schematic representation of the grain size calculation method.

A.5 Energy Dispersive X-ray Spectroscopy on iodine and bromine doped ZTO samples

In order to chemically quantify the samples analyzed in Chapter **??**, several EDX spectra were acquired on different sample positions and quantified using the K lines of each element. In particular, the samples described in this sections are the ZTO in sandwich configuration spin coated with SnI_2 and $SnBr_2$, both in their as deposited and annealed states. The scheme in Figure A.8 represents the positions were the spectra were extracted. For each of the four samples,
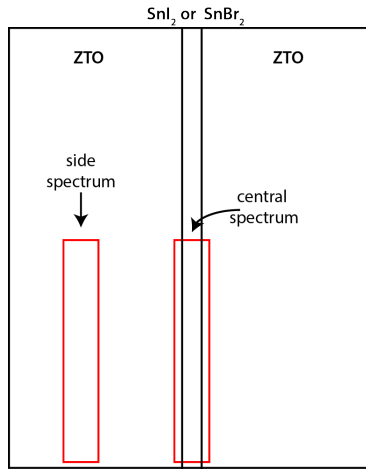

Figure A.8: For every sample (four in total) two spectra were acquired, one in the central section of the sample and one on its left side, into the ZTO layer. The region of interest are highlighted by the red frames.

the side and central spectra are presented, moreover, in order to zoom into the interesting regions, not all the energies are presented but only the meaningful ones for iodine and bromine. The goal of these graphs is to show if any signal related to iodine or bromine is registered during the acquisition. Iodine doped samples, as deposited and annealed at 500 °C are presented in Figure A.9 and A.10 respectively. Bromine doped samples, as deposited and annealed at 500 °C are presented in Figure A.11 and A.12 respectively. Figure A.9 (a) and (c) clearly show the overlap between the theoretical lines of tin and iodine in the first range of energies. Moreover, almost no difference is detected between the spectra to the left (a) and (b) and the ones to the right (c) and (d), as if no difference in the concentration of iodine was detected in the central and side part of the sample. A larger concentration of iodine would be expected in the central part of the sample with respect to the side. The concentration for both the center and side of the sample is: $I = 1\,at\%$, $Sn = 53\,at\%$, $O = 37\,at\%$, $Zn = 9\,at\%$
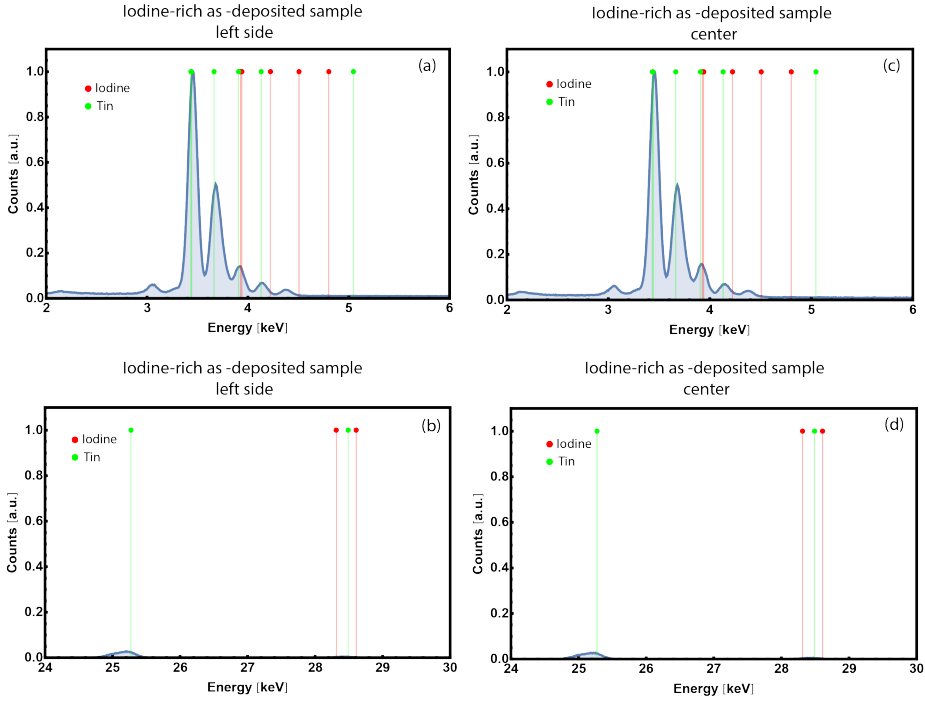
Figure A.9: Spectrum taken on the left side (a) and (b) of the iodine rich sample in its as-deposited state for energies between $2\,\mathrm{keV}$ and $6\,\mathrm{keV}$ (a) and $24\,\mathrm{keV}$ and $30\,\mathrm{keV}$ (b). Spectrum from the central region of the sandwich (c) and (d) for the same energy range as before. Theoretical energies related to the X-ray lines of tin and iodine are superposed.

with a relative error of 3σ equal to $3\sigma_I = 18\%$, $3\sigma_{Sn} = 9\%$, $3\sigma_O = 10\%$ and $3\sigma_{Zn} = 10\%$. These phenomena are the reason why the detection of iodine is extremely difficult for this sample.

As for the as-deposited sample, also for the annealed one, presented in Figure A.10 the overlap between tin and iodine EDX lines is likely to be the cause of a overestimated quantification of the latter. The quantification in this case is found to be equal to: $I = 3\,at\%$, $Sn = 42\,at\%$, $O = 48\,at\%$, $Zn = 7\,at\%$ with a relative error of 3σ equal to $3\sigma_I = 3\%$, $3\sigma_{Sn} = 9\%$, $3\sigma_O = 2\%$ and $3\sigma_{Zn} = 1\%$.

For the as deposited sample in Figure A.11, no evidence of bromine is found. This is probably due to a problem during the spin coating step.

Figure A.12 shows evidence of bromine in the central part of the sample and a residue in the left side. The quantification from the central part gives $Br =$

Figure A.10: Spectrum taken on the left side (a) and (b) of the iodine rich sample in its annealed state for energies between $2\,\mathrm{keV}$ and $6\,\mathrm{keV}$ (a) and $24\,\mathrm{keV}$ and $30\,\mathrm{keV}$ (b). Spectrum from the central region of the sandwich (c) and (d) for the same energy range as before. Theoretical energies related to the X-ray lines of tin and iodine are superposed.

$6\,at\%$, $Sn = 48\,at\%$, $O = 36\,at\%$, $Zn = 10\,at\%$ with a relative error of 3σ equal to $3\sigma_{Br} = 11\%$, $3\sigma_{Sn} = 9\%$, $3\sigma_O = 10\%$ and $3\sigma_{Zn} = 10\%$. In the side part: $Br = 2\,at\%$, $Sn = 51\,at\%$, $O = 38\,at\%$, $Zn = 9\,at\%$ with a relative error of 3σ equal to $3\sigma_{Br} = 11\%$, $3\sigma_{Sn} = 9\%$, $3\sigma_O = 10\%$ and $3\sigma_{Zn} = 10\%$.

Figure A.11: Spectrum taken on the left side (a) and (b) of the bromine rich sample in its as-deposited state for energies between $0\,\text{keV}$ and $2\,\text{keV}$ (a) and $11\,\text{keV}$ and $13\,\text{keV}$ (b). Spectrum from the central region of the sandwich (c) and (d) for the same energy range as before. Theoretical energies related to the X-ray lines of bromine are superposed.
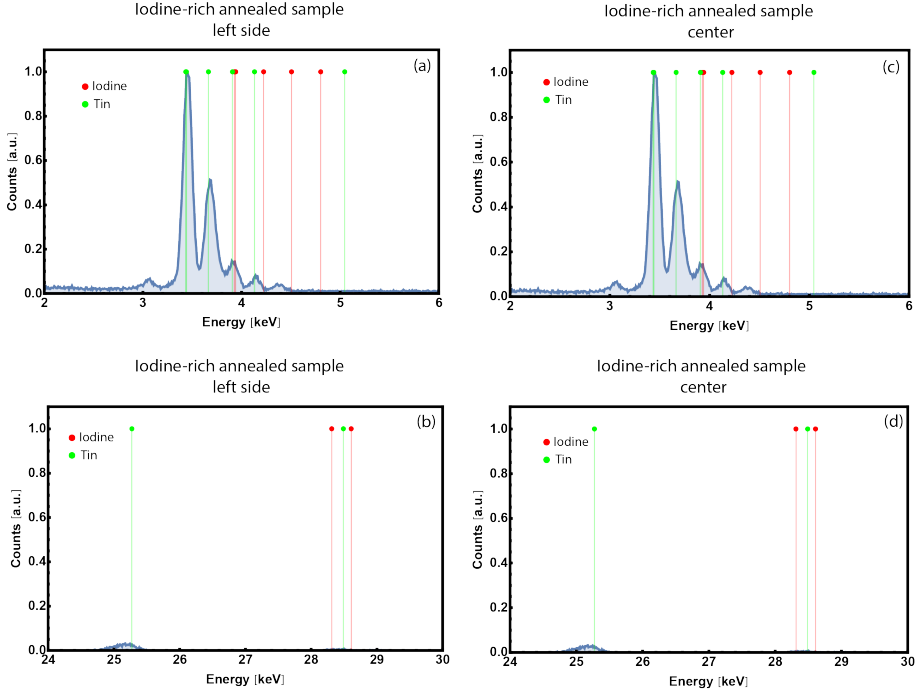
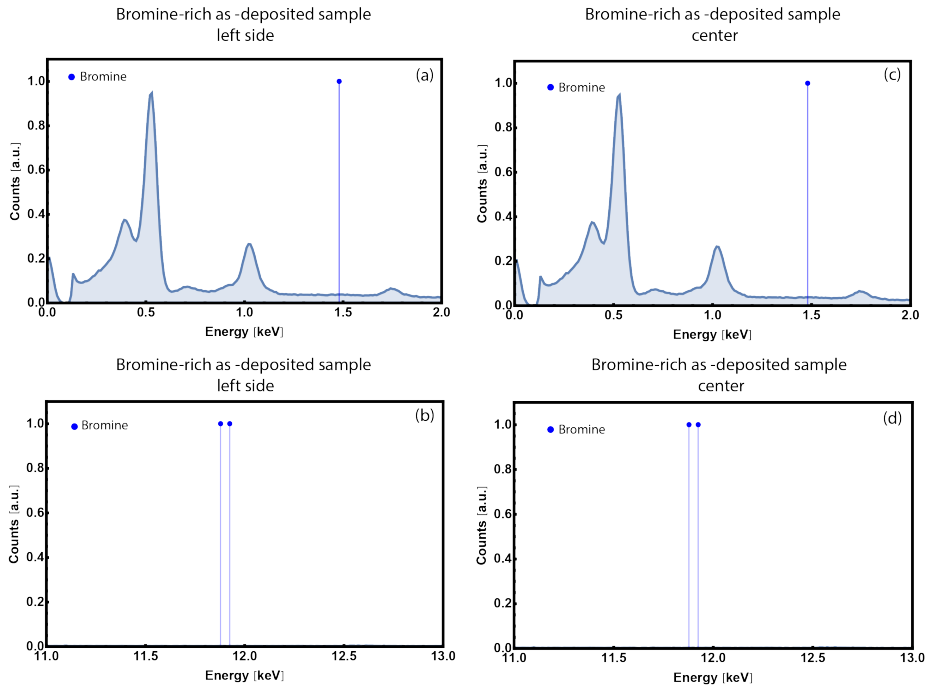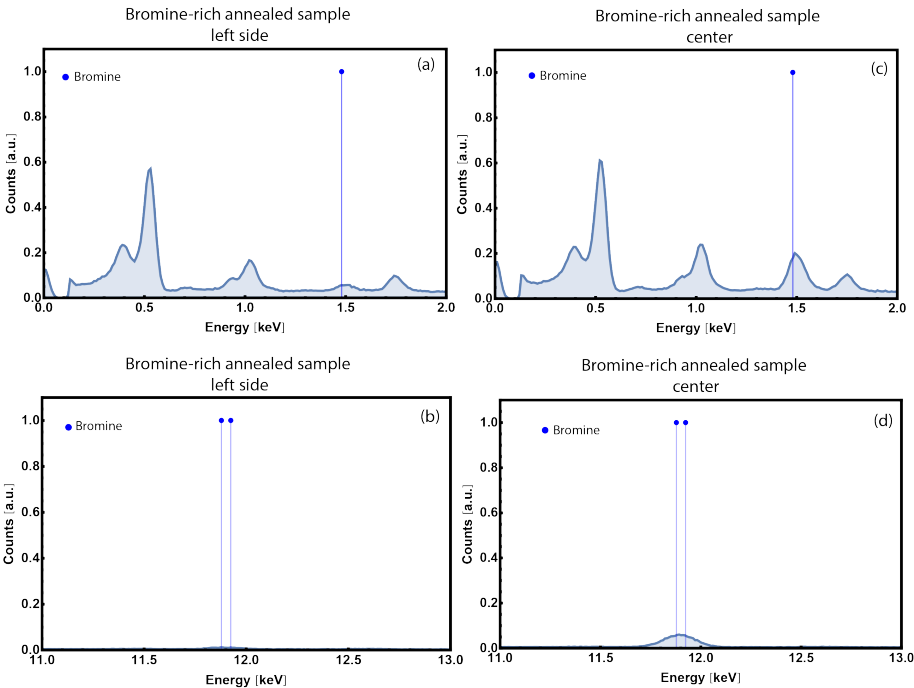**Figure A.12:** Spectrum taken on the left side (a) and (b) of the bromine rich sample in its annealed state for energies between $0\,\mathrm{keV}$ and $2\,\mathrm{keV}$ (a) and $11\,\mathrm{keV}$ and $13\,\mathrm{keV}$ (b). Spectrum from the central region of the sandwich (c) and (d) for the same energy range as before. Theoretical energies related to the X-ray lines of bromine are superposed.

Bibliography

[1] D. S. Ginley and C. Bright, "Transparent Conducting Oxides," *MRS Bulletin*, pp. 15–18, 2000.

[2] H. Hosono, "Recent progress in transparent oxide semiconductors: Materials and device application," *Thin Solid Films*, vol. 515, pp. 6000–6014, 2007.

[3] K. Ellmer, "Past achievements and future challenges in the development of optically transparent electrodes," *Nature Photonics*, vol. 6, no. December, pp. 808–816, 2012.

[4] C. G. Granqvist, "Transparent conductors for solar energy and energy efficiency: a broad-brush picture," *International Journal of Nanotechnology*, vol. 6, no. 9, p. 785, 2009.

[5] P. D. C. King and T. D. Veal, "Conductivity in transparent oxide semiconductors.," *Journal of physics. Condensed matter : an Institute of Physics journal*, vol. 23, no. 33, p. 334214, 2011.

[6] S. Calnan and a. N. Tiwari, "High mobility transparent conducting oxides for thin film solar cells," *Thin Solid Films*, vol. 518, no. 7, pp. 1839–1849, 2010.

[7] *Handbook of Transparent Conductors*. 2011.

[8] S. D. Wolf, A. Descoeudres, Z. C. Holman, and C. Ballif, "High-efficiency Silicon Heterojunction Solar Cells : A Review," vol. 2, pp. 7–24, 2012.

[9] J. Ràfols-ribé, P.-a. Will, C. Hänisch, M. Gonzalez-silveira, S. Lenk, J. Rodríguez-viejo, and S. Reineke, "High-performance organic light-emitting diodes comprising ultrastable glass layers," no. May, pp. 1–10, 2018.

[10] M. Batzill and U. Diebold, "The surface and materials science of tin oxide," vol. 79, pp. 47–154, 2005.

[11] E. L. Runnerstrom, A. Llorde, S. D. Lounis, and D. J. Milliron, "traditional materials and NIR-selective," pp. 5–7, 2014.

[12] H. Hosono and K. Ueda, *Handbook of Electronic and Photonic Materials*. Springer, 2017.

[13] T. C. Yeh, Q. Zhu, D. B. Buchholz, a. B. Martinson, R. P. H. Chang, and T. O. Mason, "Amorphous transparent conducting oxides in context: Work function survey, trends, and facile modification," *Applied Surface Science*, vol. 330, pp. 405–410, 2015.

[14] T. Koida, Y. Ueno, and H. Shibata, "In 2 O 3 -Based Transparent Conducting Oxide Films with High Electron Mobility Fabricated at Low Process Temperatures," *physica status solidi (a)*, vol. 215, p. 1700506, apr 2018.

[15] J. Yu, J. Bian, W. Duan, Y. Liu, J. Shi, F. Meng, and Z. Liu, "Tungsten doped indium oxide film: Ready for bifacial copper metallization of silicon heterojunction solar cell," *Solar Energy Materials and Solar Cells*, vol. 144, pp. 359–363, 2016.

[16] M. V. Frischbier, H. F. Wardenga, M. Weidner, O. Bierwagen, J. Jia, Y. Shigesato, and A. Klein, "Influence of dopant species and concentration on grain boundary scattering in degenerately doped In2O3 thin films," *Thin Solid Films*, vol. 614, pp. 62–68, 2015.

[17] S. Dixon, D. Scanlon, C. Carmalt, and I. Parkin, "n-Type doped transparent conducting binary oxides: an overview," *J. Mater. Chem. C*, vol. 419, no. 2, pp. 462–465, 2016.

[18] B. Macco, H. C. Knoops, and W. M. Kessels, "Electron scattering and doping mechanisms in solid phase crystallized In2O3:H prepared by atomic layer deposition," *ACS Applied Materials & Interfaces*, 2015.

[19] R. Clanget, "Ionized impurity scattering in degenerate In2O3," *Applied Physics*, vol. 2, no. 5, pp. 247–256, 1973.

[20] J. Steinhauser, S. Faÿ, N. Oliveira, E. Vallat-Sauvain, and C. Ballif, "Transition between grain boundary and intragrain scattering transport mechanisms in boron-doped zinc oxide thin films," *Applied Physics Letters*, vol. 90, no. 14, pp. 2–4, 2007.

[21] D. L. Young, T. J. Coutts, V. I. Kaydanov, A. S. Gilmore, and W. P. Mulligan, "Direct measurement of density of states effective mass and scattering parameter in transparent conducting oxides using second-order transport phenomena," *Journal of Vacuum Science & Technology A: Vacuum, Surfaces, and Films*, vol. 18, no. 6, p. 2978, 2000.

[22] A. Stadler, "Transparent Conducting Oxides—An Up-To-Date Overview," *Materials*, vol. 5, no. 12, pp. 661–683, 2012.

[23] S. Dixon, D. Scanlon, C. Carmalt, and I. Parkin, "n-Type doped transparent conducting binary oxides: an overview," *J. Mater. Chem. C*, vol. 419, no. 2, pp. 462–465, 2016.

[24] R. G. Gordon, "Criteria for Choosing Transparent Conductors," *MRS Bulletin*, vol. 25, no. 08, pp. 52–57, 2000.

[25] T. Minami, "Transparent conducting oxide semiconductors for transparent electrodes," *Semiconductor Science and Technology*, vol. 20, pp. S35–S44, 2005.

[26] M. Frenzel, C. Mikolajczak, M. A. Reuter, and J. Gutzmer, "Quantifying the relative availability of high-tech by-product metals – The cases of gallium , germanium and indium," *Resources Policy*, vol. 52, no. October 2016, pp. 327–335, 2017.

[27] European Commission, "Report on critical raw materials for the EU, Report of the Ad hoc Working Group on defining critical raw materials," no. May, p. 41, 2014.

[28] M. Lokanc, R. Eggert, and M. Redlinger, "The Availability of Indium: The Present, Medium Term, and Long Term," *National Renewable Energy Laboratory*, vol. October, no. October, pp. 1–90, 2015.

[29] R. L. Moss, E. Tzimas, H. Kara, P. Willis, and J. Kooroshy, *Critical Metals in Strategic Energy Technologies*. 2011.

[30] S. Das and V. Jayaraman, "SnO2: A comprehensive review on structures and gas sensors," *Progress in Materials Science*, vol. 66, pp. 112–255, 2014.

[31] K. C. Mishra, K. H. Johnson, and P. C. Schmidt, "Electronic structure of antimony-doped tin oxide," *Physical Review B*, vol. 51, no. 20, pp. 13972–13976, 1995.

[32] A. Fuchs, H. J. Schimper, A. Klein, and W. Jaegermann, "Photoemission studies on undoped SnO 2 buffer layers for CdTe thin film solar cells," *Energy Procedia*, vol. 10, pp. 149–154, 2011.

[33] A. M. Ganose and D. O. Scanlon, "Band gap and work function tailoring of SnO2for improved transparent conducting ability in photovoltaics," *Journal of Materials Chemistry C*, vol. 4, no. 7, pp. 1467–1475, 2016.

[34] K. B. Sundaram and G. K. Bhagavat, "Optical absorption studies on tin oxide films," *Journal of Physics D: Applied Physics*, vol. 14, no. 5, pp. 921–925, 2000.

[35] G. Sanon, R. Rup, and A. Mansingh, "Band-gap narrowing and band structure in degenerate tin oxide (SnO2) films," *Physical Review B*, vol. 44, no. 11, pp. 5672–5680, 1991.

[36] M. Feneberg, C. Lidig, K. Lange, M. E. White, M. Y. Tsai, J. S. Speck, O. Bierwagen, and R. Goldhahn, "Anisotropy of the electron effective mass in rutile SnO2 determined by infrared ellipsometry," *Physica Status Solidi (A) Applications and Materials Science*, vol. 211, no. 1, pp. 82–86, 2014.

[37] T. Takizawa, T. Sakurai, P. T. Films, T. Yamazaki, U. Mizutani, Y. Iwama, T. Hayashi, and H. Tsukamoto, "Related content Vapor Reaction Growth of SnO 2 Single Crystals and Their Properties," 1965.

[38] K. J. Button, C. G. Fonstad, and W. Dreybrodt, "Determination of the electron masses in stannic oxide by submillimeter cyclotron resonance," *Physical Review B*, vol. 4, no. 12, pp. 4539–4542, 1971.

[39] A. T. Lino, P. D. Borges, L. M. Scolfaro, S. C. Rodrigues, and E. F. Da Silva, "Optical properties and carrier effective masses of rutile SnO2 as obtained from full relativistic ab initio calculations," *AIP Conference Proceedings*, vol. 893, no. 2007, pp. 259–260, 2007.

[40] M. Ahrlich, O. Sergeev, M. Juilfs, A. Neumüller, M. Vehse, and C. Agert, "Improved Light Management in Silicon Heterojunction Solar Cells by Application of a ZnO Nanorod Antireflective Layer," *Energy Procedia*, vol. 92, pp. 284–290, 2016.

[41] T. M. Hammad, "Electrical and optical properties of multilayer sol gel ZnO coatings," *Int. J. Mod. Phys. B*, vol. 20, no. 23, pp. 3357–3364, 2006.

[42] P. F. Carcia, R. S. McLean, M. D. Groner, A. A. Dameron, and S. M. George, "Gas diffusion ultrabarriers on polymer substrates using Al2O3 atomic layer deposition and SiN plasma-enhanced chemical vapor deposition," *Journal of Applied Physics*, vol. 106, no. 2, 2009.

[43] S. Faÿ, U. Kroll, C. Bucher, E. Vallat-Sauvain, and A. Shah, "Low pressure chemical vapour deposition of ZnO layers for thin-film solar cells: Temperature-induced morphological changes," *Solar Energy Materials and Solar Cells*, vol. 86, no. 3, pp. 385–397, 2005.

[44] I. Volintiru, M. Creatore, B. J. Kniknie, C. I. M. A. Spee, and M. C. M. Van De Sanden, "Evolution of the electrical and structural properties during the growth of Al doped ZnO films by remote plasma-enhanced metalorganic chemical vapor deposition," *Journal of Applied Physics*, vol. 102, no. 4, 2007.

[45] N. Naghavi, D. Abou-Ras, N. Allsop, N. Barreau, S. Bücheler, A. Ennaoui, C. H. Fischer, C. Guillen, D. Hariskos, J. Herrero, R. Klenk, K. Kushiya, D. Lincot, R. Menner, T. Nakada, C. Platzer-Björkman, S. Spiering, A. N. Tiwari, and T. Törndahl, "Buffer layers and transparent conducting oxides for chalcopyrite Cu(In,Ga)(S,Se)2based thin film photovoltaics: Present status and current developments," *Progress in Photovoltaics: Research and Applications*, vol. 18, no. 6, pp. 411–433, 2010.

[46] Z.-Y. Ye, H.-L. Lu, Y. Geng, Y.-Z. Gu, Z.-Y. Xie, Y. Zhang, Q.-Q. Sun, S.-J. Ding, and D. W. Zhang, "Structural, electrical, and optical properties of Ti-doped ZnO films fabricated by atomic layer deposition," *Nanoscale Research Letters*, vol. 8, no. 1, p. 108, 2013.

[47] T. Y. Agura H., "Transparent conducting ZnO thin films prepared at room temperature by PLD method," *IEEJ Transactions on Electronics, Information and Systems*, vol. 126, no. 11, pp. 1268–1276, 2006.

[48] A. Suzuki, M. Nakamura, R. Michihata, T. Aoki, T. Matsushita, and M. Okuda, "Ultrathin Al-doped transparent conducting zinc oxide films fabricated by pulsed laser deposition," *Thin Solid Films*, vol. 517, no. 4, pp. 1478–1481, 2008.

[49] Y. Zhu, R. J. Mendelsberg, S. H. N. Lim, J. Zhu, J. Han, and A. Anders, "Improved structural and electrical properties of thin ZnO:Al films by dc filtered cathodic arc deposition," *Journal of Materials Research*, vol. 27, no. 5, pp. 857–862, 2012.

[50] J. H. Kuang and H. L. Chien, "The effect of film thickness on mechanical properties of TiN thin films," *Advanced Science Letters*, vol. 4, no. 11-12, pp. 3570–3575, 2011.

[51] M. Kon, P. K. Song, Y. Shigesato, P. Frach, S. Ohno, and K. Suzuki, "Impedance control of reactive sputtering process in mid-frequency mode with dual cathodes to deposit Al-doped ZnO films," *Japanese Journal of Applied Physics, Part 1: Regular Papers and Short Notes and Review Papers*, vol. 42, no. 1, pp. 263–269, 2003.

[52] T. Minami, S. Suzuki, and T. Miyata, "Transparent conducting impurity-co-doped ZnO:Al thin films prepared by magnetron sputtering," *Thin Solid Films*, vol. 398-399, pp. 53–58, 2001.

[53] T. Minami, H. Sato, T. Sonoda, H. Nanto, and S. Takata, "Influence of substrate and target temperatures on properties of transparent and conductive doped ZnO thin films prepared by r.f. magnetron sputtering," *Thin Solid Films*, vol. 171, no. 2, pp. 307–311, 1989.

[54] M. Berginski, J. Hüpkes, W. Reetz, B. Rech, and M. Wuttig, "Recent development on surface-textured ZnO:Al films prepared by sputtering for thin-film solar cell application," *Thin Solid Films*, vol. 516, no. 17, pp. 5836–5841, 2008.

[55] T. Koida, M. Kondo, K. Tsutsumi, A. Sakaguchi, M. Suzuki, and H. Fujiwara, "Hydrogen-doped In2O3 transparent conducting oxide films prepared by solid-phase crystallization method," *Journal of Applied Physics*, vol. 107, no. 3, 2010.

[56] S. Tohoda, D. Fujishima, A. Yano, A. Ogane, K. Matsuyama, Y. Nakamura, N. Tokuoka, H. Kanno, T. Kinoshita, H. Sakata, M. Taguchi, and E. Maruyama, "Future directions for higher efficiency HIT solar cells using a Thin Silicon Wafer Voc," *Journal of Non-Crystalline Solids*, vol. 358, no. 17, pp. 2219–2222, 2012.

[57] K. Chopra, S. Major, and D. Pandya, "Transparent Conductors- A status review," *Thin Solid Films*, vol. 102, pp. 1–46, 1983.

[58] Jarzebski Z.M and J. Marton, "Physical Properties of SnO2 Materials," *Journal of The Electrochemical Society*, no. 13, pp. 199–205, 1976.

[59] S. Samson and C. G. Fonstad, "Defect structure and electronic donor levels in stannic oxide crystals," *Journal of Applied Physics*, vol. 44, no. 10, pp. 4618–4621, 1973.

[60] Ç. Kılıç and A. Zunger, "Origins of coexistence of conductivity and transparency in SnO2," *Physical Review Letters*, vol. 88, no. 9, pp. 955011–955014, 2002.

[61] J. E. Medvedeva and A. J. Freeman, "Combining high conductivity with complete optical transparency: A band structure approach," *Europhysics Letters*, vol. 69, no. 4, pp. 583–587, 2005.

[62] H. C. M. Knoops, B. W. H. van de Loo, S. Smit, M. V. Ponomarev, J.-W. Weber, K. Sharma, W. M. M. Kessels, and M. Creatore, "Optical modeling of plasma-deposited ZnO films: Electron scattering at different length scales," *Journal of Vacuum Science & Technology A: Vacuum, Surfaces, and Films*, vol. 33, no. 2, p. 021509, 2015.

[63] S. Samson and C. G. Fonstad, "Defect structure and electronic donor levels in stannic oxide crystals," *Journal of Applied Physics*, vol. 44, no. 10, pp. 4618–4621, 1973.

[64] B. Stjerna, E. Olsson, and C. G. Granqvist, "Optical and electrical properties of radio frequency sputtered tin oxide films doped with oxygen vacancies, F, Sb, or Mo," *Journal of Applied Physics*, vol. 76, no. 6, pp. 3797–3817, 1994.

[65] E. Shanthi, V. Dutta, A. Banerjee, and K. L. Chopra, "Electrical and optical properties of undoped and antimony-doped tin oxide films," *Journal of Applied Physics*, vol. 51, no. 12, pp. 6243–6251, 1980.

[66] S. W. Lee, Y. W. Kim, and H. Chen, "Electrical properties of Ta-doped SnO2thin films prepared by the metal-organic chemical-vapor deposition method," *Applied Physics Letters*, vol. 78, no. 3, pp. 350–352, 2001.

[67] C. Agashe and S. S. Major, "Effect of F, Cl and Br doping on electrical properties of sprayed SnO2 films," *Journal of Materials Science Letters*, vol. 15, no. 6, pp. 497–499, 1996.

[68] Z. Ji, Z. He, Y. Song, K. Liu, and Z. Ye, "Fabrication and characterization of indium-doped p-type SnO2 thin films," *Journal of Crystal Growth*, vol. 259, no. 3, pp. 282–285, 2003.

[69] C. Chen, Z. Ji, C. Wang, L. Zhao, and Q. Zhou, "P-type tin-indium oxide films prepared by thermal oxidation of metallic InSn alloy films," *Materials Letters*, vol. 60, no. 25-26, pp. 3096–3099, 2006.

[70] T. Yang, J. Zhao, X. Li, X. Gao, C. Xue, Y. Wu, and R. Tai, "Preparation and characterization of p-type transparent conducting SnO thin films," *Materials Letters*, vol. 139, pp. 39–41, 2015.

[71] M. M. Bagheri-Mohagheghi and M. Shokooh-Saremi, "The influence of Al doping on the electrical, optical and structural properties of SnO2 transparent conducting films deposited by the spray pyrolysis technique," *Journal of Physics D: Applied Physics*, vol. 37, no. 8, pp. 1248–1253, 2004.

[72] C. Agashe, M. G. Takwale, V. G. Bhide, S. Mahamuni, and S. K. Kulkarni, "Effect of Sn incorporation on the growth mechanism of sprayed SnO2films," *Journal of Applied Physics*, vol. 70, no. 12, pp. 7382–7386, 1991.

[73] S. K. Song, J. S. Cho, W. K. Choi, H. J. Jung, D. Choi, J. Y. Lee, H. K. Baik, and S. K. Koh, "Structure and gas-sensing characteristics of undoped tin oxide thin films fabricated by ion-assisted deposition," *Sensors and Actuators, B: Chemical*, vol. 46, no. 1, pp. 42–49, 1998.

[74] H. S. Randhawa, M. D. Matthews, and R. F. Bunshah, "SnO2 films prepared by activated reactive evaporation," *Thin Solid Films*, vol. 83, no. 2, pp. 267–271, 1981.

[75] A. Carrol and L. Slack, "Effects of Additions to SnO2 Thin Films," *J. Electrochem. Soc.: Solid-State Science and Technology*, vol. 123, no. 12, pp. 1889–1893, 1976.

[76] V. Casey and M. I. Stephenson, "A study of undoped and molybdenum doped, polycrystalline, tin oxide thin films produced by a simple reactive evaporation technique," *Journal of Physics D: Applied Physics*, vol. 23, no. 9, pp. 1212–1215, 1990.

[77] T. Yang, X. Qin, H. H. Wang, Q. Jia, R. Yu, B. Wang, J. Wang, K. Ibrahim, X. Jiang, and Q. He, "Preparation and application in p-n homojunction diode of p-type transparent conducting Ga-doped SnO2thin films," *Thin Solid Films*, vol. 518, no. 19, pp. 5542–5545, 2010.

[78] A. Janotti and C. G. Van de Walle, "LDA + U and Hybrid Functional Calculations for Defects in ZnO, SnO2, and TiO2," *Advanced Calculations for Defects in Materials: Electronic Structure Methods*, vol. 804, no. 4, pp. 155–164, 2011.

[79] C. G. Fonstad and R. H. Rediker, "Electrical properties of high-quality stannic oxide crystals," *Journal of Applied Physics*, vol. 42, no. 7, pp. 2911–2918, 1971.

[80] M. Kojima, H. Kato, A. Imai, and A. Yoshida, "Electronic conduction of tin oxide thin films prepared by chemical vapor deposition," *Journal of Applied Physics*, vol. 64, no. 4, pp. 1902–1905, 1988.

[81] M. Grauzinyte, S. Goedecker, and J. A. Flores-Livas, "Computational screening of useful hole-electron dopants in SnO 2," *Chemistry of Materials*, p. acs.chemmater.7b03862, 2017.

[82] J. P. Perdew, M. Ernzerhof, K. Burke, J. P. Perdew, M. Ernzerhof, and K. Burke, "Rationale for mixing exact exchange with density functional approximations Rationale for mixing exact exchange with density functional approximations," vol. 9982, no. June 1998, 2006.

[83] B. Alterkop, N. Parkansky, S. Goldsmith, and R. L. Boxman, "Effect of air annealing on opto-electrical," 2003.

[84] Z. Chen, J. Lai, C. Shek, and H. Chen, "Production of amorphous tin oxide thin films and microstructural transformation induced by heat treatment," *Applied Physics A*, vol. 81, no. 5, pp. 1073–1076, 2005.

[85] S. S. Lekshmy, I. J. Berlin, L. V. Maneeshya, Anitha, and K. Joy, "Structural and optical characterisation of tin dioxide thin films by sol-gel dip coating technique," *IOP Conference Series: Materials Science and Engineering*, vol. 73, no. 1, pp. 6–10, 2015.

[86] H.-C. Shin, J. Dong, and M. Liu, "Porous Tin Oxides Prepared Using an Anodic Oxidation Process," *Advanced Materials*, vol. 16, no. 3, pp. 237–240, 2004.

[87] D. Jousse, C. Constantino, and I. Chambouleyron, "Highly conductive and transparent amorphous tin oxide," *Journal of Applied Physics*, vol. 54, no. 1, pp. 431–434, 1983.

[88] C. M. Wang, C. C. Huang, J. C. Kuo, D. R. Sahu, and J. L. Huang, "Effect of annealing temperature and oxygen flow in the properties of ion beam sputtered SnO_(2-x) thin films," *Materials*, vol. 8, no. 8, pp. 5289–5297, 2015.

[89] M. Hemissi and H. A. Adnani, "Influence of annealing time on structural and electrical properties of Sb doped SnO 2 films," *Revue des Energies Renouvelables*, vol. 10, pp. 273–279, 2007.

[90] D. B. Buchholz, Q. Ma, D. Alducin, A. Ponce, M. Jose-yacaman, R. Khanal, J. E. Medvedeva, and R. P. H. Chang, "The Structure and Properties of Amorphous Indium Oxide," 2014.

[91] O. Dinner, G. E. Shter, and G. S. Grader, "Solvothermal synthesis of indium-doped zinc oxide TCO films," *Journal of Sol-Gel Science and Technology*, vol. 81, no. 1, pp. 3–10, 2017.

[92] T. Minami, H. Sonohara, S. Takata, and H. Sato, "Highly Transparent and Conductive Zinc-Stannate Thin Films Prepared by RF Magnetron Sputtering," *Japanese Journal of Applied Physics*, vol. 33, pp. 1693–1696, 1994.

[93] T. Minami, T. Miyata, and T. Yamamoto, "Stability of transparent conducting oxide films for use at high temperatures," *Journal of Vacuum Science & Technology A: Vacuum, Surfaces, and Films*, vol. 17, no. 1999, p. 1822, 1999.

[94] M. P. Taylor, D. W. Readey, M. F. A. M. Van Hest, C. W. Teplin, J. L. Alleman, M. S. Dabney, L. M. Gedvilas, B. M. Keyes, B. To, J. D. Perkins, and D. S. Ginley, "The remarkable thermal stability of amorphous In-Zn-O transparent conductors," *Advanced Functional Materials*, vol. 18, no. 20, pp. 3169–3178, 2008.

[95] V. K. Jain, P. Kumar, D. Bhandari, and Y. K. Vijay, "Growth and characterization of transparent conducting nanostructured zinc indium oxide thin films," *Thin Solid Films*, vol. 519, no. 3, pp. 1082–1086, 2010.

[96] Q. Zhu, Q. Ma, D. B. Buchholz, R. P. H. Chang, M. J. Bedzyk, and T. O. Mason, "Structural and physical properties of transparent conducting, amorphous Zn-doped SnO2 films," *Journal of Applied Physics*, vol. 115, no. 3, 2014.

[97] J. H. Ko, I. H. Kim, D. Kim, K. S. Lee, T. S. Lee, J. H. Jeong, B. Cheong, Y. J. Baik, and W. M. Kim, "Effects of ZnO addition on electrical and structural properties of amorphous SnO2 thin films," *Thin Solid Films*, vol. 494, no. 1-2, pp. 42–46, 2006.

[98] U. K. Kim, S. H. Rha, J. H. Kim, Y. J. Chung, J. Jung, E. S. Hwang, J. Lee, T. J. Park, J.-H. Choi, and C. S. Hwang, "Study on the defects in metal–organic chemical vapor deposited zinc tin oxide thin films using negative bias illumination stability analysis," *Journal of Materials Chemistry C*, vol. 1, p. 6695, 2013.

[99] M. K. Jayaraj, K. J. Saji, K. Nomura, T. Kamiya, and H. Hosono, "Optical and electrical properties of amorphous zinc tin oxide thin films examined for thin film transistor application," *Journal of Vacuum Science & Technology B*, vol. 26, no. 2, pp. 495–501, 2008.

[100] K. J. Chen, F. Y. Hung, S. J. Chang, S. J. Young, Z. S. Hu, and S. P. Chang, "An investigation of the microstructure, optical and electrical properties of ZITO thin film using the sol-gel method," *Journal of Sol-Gel Science and Technology*, vol. 54, no. 3, pp. 347–354, 2010.

[101] D. M. Mattox, "Physical vapor deposition (PVD) processes," *Metal Finishing*, vol. 98, no. 1, pp. 410–423, 2000.

[102] S. Swann, "Magnetron sputtering," *Physics in Technology*, vol. 19, no. 2, pp. 67–75, 1988.

[103] Y. Taga and R. Takahasi, "Role of kinetic energy of sputtered particles in thin film formation," *Surface Science*, vol. 386, no. 1-3, pp. 231–240, 1997.

[104] M. Morales-Masis, F. Dauzou, Q. Jeangros, A. Dabirian, H. Lifka, R. Gierth, M. Ruske, D. Moet, A. Hessler-Wyser, and C. Ballif, "An Indium-Free Anode for Large-Area Flexible OLEDs: Defect-Free Transparent Conductive Zinc Tin Oxide," *Advanced Functional Materials*, pp. 1–9, 2015.

[105] A. C. Boccara, W. Jackson, N. M. Amer, and D. Fournier, "Sensitive photothermal deflection technique for measuring absorption in optically thin media," *Optics Letters*, vol. 5, no. 9, p. 377, 1980.

[106] W. B. Jackson and N. M. Amer, "Direct measurement of gap-state absorption in hydrogenated amorphous silicon by photothermal deflection spectroscopy," *Physical Review B*, vol. 25, pp. 5559–5522, 1982.

[107] P. A. Stadelmann, "EMS - a software package for electron diffraction analysis and HREM image simulation in materials science," *Ultramicroscopy*, vol. 21, no. 2, pp. 131–145, 1987.

[108] P. Scherrer, "Bestimmung der Grosse und der inneren Struktur von Kolloidteilchen mittels Rontgenstrahlen," *Nachrichten von der Gesellschaft der Wissenschaften zu Göttingen, Mathematisch-Physikalische Klasse*, vol. 2, pp. 98–100, 1918.

[109] P. Schlossmacher, D. Klenov, B. Freitag, and H. von Harrach, "Enhanced Detection Sensitivity with a New Windowless XEDS System for AEM Based on Silicon Drift Detector Technology," *Microscopy Today*, vol. 18, no. 04, pp. 14–20, 2010.

[110] A. van den Beukel and J. Sietsma, "The glass transition as a free volume related kinetic phenomenon," *Acta Metallurgica et Materialia*, vol. 38, no. 3, pp. 383–389, 1990.

[111] G. Koebrugge, J. Sietsma, and a. van den Beukel, "STRUCTURAL RELAXATION IN AMORPHOUS Pd40 NiaoP20," *Acta Metallurgica et Materialia*, vol. 40, no. 4, pp. 753–760, 1992.

[112] A. Slipenyuk and J. Eckert, "Correlation between enthalpy change and free volume reduction during structural relaxation of Zr55Cu30Al10Ni5 metallic glass," *Scripta Materialia*, vol. 50, no. 1, pp. 39–44, 2004.

[113] Q. Hu, X. R. Zeng, and M. W. Fu, "Characteristic free volumes of bulk metallic glasses: Measurement and their correlation with glass-forming ability," *Journal of Applied Physics*, vol. 109, no. 5, pp. 10–15, 2011.

[114] M. S. Chiriacò, M. Bianco, F. Amato, E. Primiceri, F. Ferrara, V. Arima, and G. Maruccio, "Fabrication of interconnected multilevel channels in a monolithic SU-8 structure using a LOR sacrificial layer," *Microelectronic Engineering*, vol. 164, pp. 30–35, 2016.

[115] P. Pingel, M. Arvind, L. Kölln, R. Steyrleuthner, F. Kraffert, J. Behrends, S. Janietz, and D. Neher, "P-Type Doping of Poly(3-hexylthiophene) with the Strong Lewis Acid Tris(pentafluorophenyl)borane," *Advanced Electronic Materials*, vol. 2, no. 10, 2016.

[116] P. Pingel, M. Arvind, L. Kölln, R. Steyrleuthner, F. Kraffert, J. Behrends, S. Janietz, and D. Neher, "P-Type Doping of Poly(3-hexylthiophene) with the Strong Lewis Acid Tris(pentafluorophenyl)borane," *Advanced Electronic Materials*, vol. 2, no. 10, 2016.

[117] C. W. Teplin, C. S. Jiang, P. Stradins, and H. M. Branz, "Cone kinetics model for two-phase film silicon deposition," *Applied Physics Letters*, vol. 92, no. 9, pp. 2006–2009, 2008.

[118] C. W. Teplin, E. Iwaniczko, B. To, H. Moutinho, P. Stradins, and H. M. Branz, "Breakdown physics of low-temperature silicon epitaxy grown from

silane radicals," *Physical Review B - Condensed Matter and Materials Physics*, vol. 74, no. 23, pp. 4–8, 2006.

[119] P. Zaumseil, "High-resolution characterization of the forbidden Si 200 and Si 222 reflections," *Journal of Applied Crystallography*, vol. 48, pp. 528–532, 2015.

[120] C. J. Ma and K. Sera, "The chemical nature of individual size-resolved raindrops and their residual particles collected during high atmospheric loading for PM2.5," *Asian Journal of Atmospheric Environment*, vol. 11, no. 3, pp. 176–183, 2017.

[121] F. Ma, H. B. Zheng, Y. J. Sun, D. Yang, K. W. Xu, P. K. Chu, F. Ma, H. B. Zheng, Y. J. Sun, D. Yang, K. W. Xu, and P. K. Chu, "Strain effect on lattice vibration , heat capacity , and thermal conductivity of graphene Strain effect on lattice vibration , heat capacity , and thermal conductivity of graphene," *Strain*, vol. 111904, no. May, pp. 0–4, 2015.

[122] H.-W. Yeon, S.-M. Lim, J.-K. Jung, H. Yoo, Y.-J. Lee, H.-Y. Kang, Y.-J. Park, M. Kim, and Y.-C. Joo, "Structural-relaxation-driven electron doping of amorphous oxide semiconductors by increasing the concentration of oxygen vacancies in shallow-donor states," *NPG Asia Materials*, vol. 8, no. 3, p. e250, 2016.

[123] K. Ide, K. Nomura, H. Hiramatsu, T. Kamiya, and H. Hosono, "Structural relaxation in amorphous oxide semiconductor, a-In-Ga-Zn-O," *Journal of Applied Physics*, vol. 111, no. 7, 2012.

[124] E. Rucavado, Q. Jeangros, D. F. Urban, J. Holovský, Z. Remes, M. Duchamp, F. Landucci, R. E. Dunin-borkowski, W. Körner, C. El-sässer, A. Hessler-wyser, M. Morales-masis, and C. Ballif, "Enhancing the optoelectronic properties of amorphous zinc tin oxide by subgap defect passivation : A theoretical and experimental demonstration," vol. 245204, pp. 1–10, 2017.

[125] Dhananjay, S.-S. Cheng, C.-Y. Yang, C.-W. Ou, Y.-C. Chuang, M. Chyi Wu, and C.-W. Chu, " Thin Film Transistors," *Journal of Physics D: Applied Physics*, vol. 41, no. 9, p. 092006, 2008.

[126] E. Bruhat, T. Desrues, B. Grange, H. Lignier, D. Blanc-Pélissier, and S. Dubois, "TCO contacts for high efficiency c-Si solar cells: Influence of different annealing steps on the Si substrates and TCO layers properties," *Energy Procedia*, vol. 124, pp. 829–833, 2017.

[127] W. Fortunato, D. Ginley, H. Hosono, and D. C. Plaine, "Transport Conducting Oxides for Photovoltaics," *MRS Bulletin*, vol. 32, no. March, pp. 242–247, 2007.

[128] B. Stjerna, C. G. Granqvist, A. Seidel, and L. H??ggstr??m, "Characterization of rf-sputtered SnOx thin films by electron microscopy, Hall-effect measurement, and M??ssbauer spectrometry," *Journal of Applied Physics*, vol. 68, no. 12, pp. 6241–6245, 1990.

[129] Y. Sato, J. Kiyohara, A. Hasegawa, T. Hattori, M. Ishida, N. Hamada, N. Oka, and Y. Shigesato, "Study on inverse spinel zinc stannate, Zn2SnO4, as transparent conductive films deposited by rf magnetron sputtering," *Thin Solid Films*, vol. 518, no. 4, pp. 1304–1308, 2009.

[130] J. Tauc, "Optical properties and electronic structure of amorphous Ge and Si," *Materials Research Bulletin*, vol. 3, no. 1, pp. 37–46, 1968.

[131] M. N. Mullings, C. Hagglund, J. T. Tanskanen, Y. Yee, S. Geyer, and S. F. Bent, "Thin film characterization of zinc tin oxide deposited by thermal atomic layer deposition," *Thin Solid Films*, vol. 556, pp. 186–194, 2014.

[132] D. L. Young, H. Moutinho, Y. Yan, and T. J. Coutts, "Growth and characterization of radio frequency magnetron sputter-deposited zinc stannate, Zn 2SnO 4, thin films," *Journal of Applied Physics*, vol. 92, no. 1, pp. 310–319, 2002.

[133] J. Socratous, K. K. Banger, Y. Vaynzof, A. Sadhanala, A. D. Brown, A. Sepe, U. Steiner, and H. Sirringhaus, "Electronic structure of low-temperature solution-processed amorphous metal oxide semiconductors for thin-film transistor applications," *Advanced Functional Materials*, vol. 25, no. 12, pp. 1873–1885, 2015.

[134] J. H. Ko, I. H. Kim, D. Kim, K. S. Lee, T. S. Lee, B. Cheong, and W. M. Kim, "Transparent and conducting Zn-Sn-O thin films prepared by combinatorial approach," *Applied Surface Science*, vol. 253, no. 18, pp. 7398–7403, 2007.

[135] S. P. Choudhury, N. Kumari, and A. Bhattacharjee, "Study of structural, electrical and optical properties of Ni-doped SnO2 for device application: experimental and theoretical approach," *Journal of Materials Science: Materials in Electronics*, vol. 28, no. 23, pp. 18003–18014, 2017.

[136] R. R. Kasar, N. G. Deshpande, Y. G. Gudage, J. C. Vyas, and R. Sharma, "Studies and correlation among the structural , optical and electrical parameters of spray-deposited tin oxide (SnO 2) thin films with different substrate temperatures," vol. 403, pp. 3724–3729, 2008.

[137] F. Grinblat, S. Ferrari, L. G. Pampillo, F. D. Saccone, D. Errandonea, D. Santamaria-perez, A. Segura, R. Vilaplana, and C. Popescu, "Compressibility and structural behavior of pure and Fe-doped SnO 2 nanocrystals," *Solid State Sciences*, vol. 64, pp. 91–98, 2017.

[138] D. Thomas, S. C. Vattappalam, S. Mathew, and S. Augustine, "Studies on effect of oxygen flow rate in textured grain growth of ZnO thin films," *IOP Conference Series: Materials Science and Engineering*, vol. 73, no. 1, 2015.

[139] M. Alaf, M. O. Guler, D. Gultekin, M. Uysal, A. Alp, and H. Akbulut, "Effect of oxygen partial pressure on the microstructural and physical properties on nanocrystalline tin oxide films grown by plasma oxidation after thermal deposition from pure Sn targets," *Vacuum*, vol. 83, no. 2, pp. 292–301, 2008.

[140] A. Martel, F. Caballero-Briones, P. Quintana, P. Bartolo-Pérez, and J. L. Peña, "X-ray study of tin oxide films obtained by reactive DC sputtering from a metallic tin target in pure oxygen plasma," *Surface and Coatings Technology*, vol. 201, no. 8, pp. 4659–4665, 2007.

[141] A. A. Yadav, E. U. Masumdar, A. V. Moholkar, M. Neumann-Spallart, K. Y. Rajpure, and C. H. Bhosale, "Electrical, structural and optical properties of SnO2:F thin films: Effect of the substrate temperature," *Journal of Alloys and Compounds*, vol. 488, no. 1, pp. 350–355, 2009.

[142] F. A. Akgul, C. Gumus, A. O. Er, A. H. Farha, G. Akgul, Y. Ufuktepe, and Z. Liu, "Structural and electronic properties of SnO2," *Journal of Alloys and Compounds*, vol. 579, pp. 50–56, 2013.

[143] V. Consonni, G. Rey, H. Roussel, B. Doisneau, E. Blanquet, and D. Bellet, "Preferential orientation of fluorine-doped SnO2thin films: The effects of growth temperature," *Acta Materialia*, vol. 61, no. 1, pp. 22–31, 2013.

[144] H. Zheng, L. Li, Z. Sun, S. Yu, and W. Luo, "Preferential orientation, microstructure and functional properties of SnO2:Sb thin film: The effects of post-growth annealing," *Applied Surface Science*, vol. 362, pp. 230–236, 2016.

[145] C. Körber, P. Ágoston, and A. Klein, "Surface and bulk properties of sputter deposited undoped and Sb-doped SnO2thin films," *Sensors and Actuators, B: Chemical*, vol. 139, no. 2, pp. 665–672, 2009.

[146] C. G. Granqvist, J. Herrero, and G. A. Niklasson, "Preferential Orientation and Surface Oxidation Control in Reactively Sputter Deposited Nanocrystalline SnO 2 : Sb Films : Electrochemical and Optical Results," *Journal of Solid State Science and Technology*, vol. 3, no. 11, pp. 2014–2016, 2014.

[147] G. W. Lorimer, "in the Transmission Electron Microscope ; a Review," *Mineralogical Magazine*, vol. 51, pp. 49–60, 1987.

[148] A. Weidenkaff, A. Steinfeld, A. Wokaun, P. O. Auer, B. Eichler, and A. Reller, "Direct solar thermal dissociation of zinc oxide: condensation and crystallization of zinc in the presence of oxygen," *Solar Energy*, vol. 65, no. 1, pp. 59–69, 1999.

[149] D. H. Zhang and H. L. Ma, "Scattering mechanisms of charge carriers in transparent conducting oxide films," *Applied Physics A Materials Science and Processing*, vol. 62, pp. 487–492, 1996.

[150] M. P. Taylor, D. W. Readey, M. F. A. M. Van Hest, C. W. Teplin, J. L. Alleman, M. S. Dabney, L. M. Gedvilas, B. M. Keyes, B. To, J. D. Perkins, and D. S. Ginley, "The remarkable thermal stability of amorphous In-Zn-O transparent conductors," *Advanced Functional Materials*, vol. 18, no. 20, pp. 3169–3178, 2008.

[151] H. Q. Chiang, J. F. Wager, R. L. Hoffman, J. Jeong, and D. A. Keszler, "High mobility transparent thin-film transistors with amorphous zinc tin oxide channel layer," *Applied Physics Letters*, vol. 86, no. 1, pp. 22–24, 2005.

[152] I. H. Kim, D. Y. Ku, J. H. Ko, D. Kim, K. S. Lee, J. H. Jeong, T. S. Lee, B. Cheong, Y. J. Baik, and W. M. Kim, "Improvement of the thermal and chemical stability of Al doped ZnO films," *Journal of Electroceramics*, vol. 17, no. 2-4, pp. 241–245, 2006.

[153] J. Lee, S.-C. Lee, C. S. Hwang, and J.-H. Choi, "Thermodynamic stability of various phases of zinc tin oxides from ab initio calculations," *Journal of Materials Chemistry C*, vol. 1, no. Il, p. 6364, 2013.

[154] S. Albrecht, M. Saliba, K. Jäger, L. Korte, A. Hagfeldt, M. Grätzel, and B. Rech, "Towards optical optimization of planar monolithic perovskite / silicon-heterojunction tandem solar cells," *Journal of Optics*, vol. 18, no. 6, pp. 1–10, 2016.

[155] M. Shimizu, M. Suzuki, F. Iguchi, and H. Yugami, "High-temperature solar selective absorbers using transparent conductive oxide coated metal," *Energy Procedia*, vol. 57, pp. 418–426, 2014.

[156] M. Allegrezza, M. Canino, M. Bellettato, and C. Summonte, "Transparent conducting oxides for high temperature processing," *Energy Procedia*, vol. 44, no. May 2013, pp. 23–31, 2014.

[157] H. B. Wang, F. Ma, Q. Q. Li, C. Z. Dong, D. Y. Ma, H. T. Wang, and K. W. Xu, "Synthesis and stress relaxation of ZnO/Al-doped ZnO core-shell nanowires," *Nanoscale*, vol. 5, no. 7, pp. 2857–2863, 2013.

[158] E. Rucavado, M. Grauzinyte, J. A. Flores-Livas, Q. Jeangros, F. Landucci, Y. Lee, T. Koida, S. Goedecker, A. Hessler-Wyser, C. Ballif, and M. Morales-Masis, "New Route for "cold-Passivation" of Defects in Tin-Based Oxides," *Journal of Physical Chemistry C*, vol. 122, no. 31, pp. 17612–17620, 2018.

[159] W. Korner, D. F. Urban, and C. Elsasser, "Generic origin of subgap states in transparent amorphous semiconductor oxides illustrated for the cases of In-Zn-O and In-Sn-O," *Physica Status Solidi (A) Applications and Materials Science*, vol. 1481, no. 7, pp. 1476–1481, 2015.

[160] W. Körner, D. F. Urban, and C. Elsässer, "Origin of subgap states in amorphous In-Ga-Zn-O," *Journal of Applied Physics*, vol. 114, no. 16, 2013.

[161] H. F. Wardenga, M. V. Frischbier, M. Morales-Masis, and A. Klein, "In situ hall effect monitoring of vacuum annealing of In2O3:H thin films," *Materials*, vol. 8, no. 2, pp. 561–574, 2015.

[162] T. Minami, *Transparent Conductive Oxides for Transparent Electrode Applications*, vol. 88. Elsevier Inc., 2013.

[163] P. M. Voyles and D. a. Muller, "Fluctuation microscopy in the STEM," *Ultramicroscopy*, vol. 93, no. 2, pp. 147–159, 2002.

[164] P. M. Voyles, J. M. Gibson, and M. M. Treacy, "Fluctuation microscopy: A probe of atomic correlations in disordered materials," *Journal of Electron Microscopy*, vol. 49, no. 2, pp. 259–266, 2000.

[165] E. S. Watson, M. J. O'Neill, J. Justin, and N. Brenner, "A Differential Scanning Calorimeter for Quantitative Differential Thermal Analysis.," *Analytical Chemistry*, vol. 36, no. June, pp. 1233–1238, 1964.

[166] G. Wang and I. R. Harrison, "Polymer melting: heating rate effects on DSC melting peaks," *Thermochimica Acta*, vol. 231, no. C, pp. 203–213, 1994.

[167] C. T. Moynihan, A. J. Easteal, J. Wilder, and J. Tucker, "Dependence of the glass transition temperature on heating and cooling rate," *Journal of Physical Chemistry*, vol. 78, no. 26, pp. 2673–2677, 1974.

[168] J. Lin, B. Mishra, J. J. Moore, and W. D. Sproul, "A study of the oxidation behavior of CrN and CrAlN thin films in air using DSC and TGA analyses," *Surface and Coatings Technology*, vol. 202, no. 14, pp. 3272–3283, 2008.

[169] S. Roorda, J. Custer, W. Sinke, J. Poate, D. Jacobson, A. Polman, and F. Spaepen, "Structural relaxation in amorphous silicon and the role of network defects," *Nuclear Instruments and Methods in Physics Research Section B: Beam Interactions with Materials and Atoms*, vol. 59-60, pp. 344–352, 1991.

[170] Y. Baba, S. Okada, and J. ichi Yamaki, "Thermal stability of LixCoO2 cathode for lithium ion battery," *Solid State Ionics*, vol. 148, no. 3-4, pp. 311–316, 2002.

[171] D. M. Fernandes, R. Silva, A. A. Hechenleitner, E. Radovanovic, M. A. Melo, and E. A. Pineda, "Synthesis and characterization of ZnO, CuO and a mixed Zn and Cu oxide," *Materials Chemistry and Physics*, vol. 115, no. 1, pp. 110–115, 2009.

[172] K. Vinokurov, J. E. MacDonald, and U. Banin, "Structures and mechanisms in the growth of hybrid Ru-Cu 2S nanoparticles: From cages to nanonets," *Chemistry of Materials*, vol. 24, no. 10, pp. 1822–1827, 2012.

[173] D. Brandová, R. Svoboda, and J. Málek, "Influence of particle size on crystallization and relaxation behavior of Ge20Se4Te76glass for infrared optics," *Journal of Non-Crystalline Solids*, vol. 433, pp. 75–81, 2016.

[174] T. J. Konno and R. Sinclair, "Metal-contact-induced crystallization of semiconductors," *Materials Science and Engineering A*, vol. 179-180, no. PART 1, pp. 426–432, 1994.

[175] D. Toloman, A. Popa, M. Stan, C. Socaci, A. R. Biris, G. Katona, F. Tudorache, I. Petrila, and F. Iacomi, "Applied Surface Science Reduced graphene oxide decorated with Fe doped SnO 2 nanoparticles for humidity sensor," *Applied Surface Science*, vol. 402, pp. 410–417, 2017.

[176] J. Dashdorj, M. E. Zvanut, and L. J. Stanley, "Iron-related defect levels in SrTiO3measured by photoelectron paramagnetic resonance spectroscopy," *Journal of Applied Physics*, vol. 107, no. 8, pp. 1–5, 2010.

[177] I. P. Bykov, L. P. Yurchenko, Y. A. Zagorodniy, V. V. Trachevsky, V. Dimza, K. Nejezchleb, L. Jastrabik, A. Dejneka, and I. Bykov, "The nature of the defect structure of solid solutions based on lead zirconate titanate (PZT): Evidence from EPR and NMR," *2013 Joint IEEE International Symposium on Applications of Ferroelectric and Workshop on Piezoresponse Force Microscopy, ISAF/PFM 2013*, pp. 197–200, 2013.

[178] M. E. Zvanut, S. Jeddy, E. Towett, G. M. Janowski, C. Brooks, and D. Schlom, "An annealing study of an oxygen vacancy related defect in SrTiO3 substrates," *Journal of Applied Physics*, vol. 104, no. 6, pp. 0–5, 2008.

[179] S. Shi, D. Gao, Q. Xu, Z. Yang, and D. Xue, "Singly-charged oxygen vacancy-induced ferromagnetism in mechanically milled SnO2powders," *RSC Advances*, vol. 4, no. 85, pp. 45467–45472, 2014.

[180] D. A. Popescu, J.-m. Herrmann, D. Chimie, U. Paris, D. Diderot, and A. April, "Nanosized tin dioxide : Spectroscopic (UV – VIS , NIR , EPR) and electrical conductivity studies," 2001.

[181] P. D. C. King, T. D. Veal, P. H. Jefferson, J. Zuniga-Perez, V. Munoz-Sanjose, and C. F. McConville, "Unification of the electrical behavior of defects, impurities, and surface states in semiconductors: Virtual gap states in CdO," *Physical Review B - Condensed Matter and Materials Physics*, vol. 79, no. 3, pp. 1–5, 2009.

[182] K. Nomura, T. Kamiya, and H. Hosono, "Effects of Diffusion of Hydrogen and Oxygen on Electrical Properties of Amorphous Oxide Semiconductor, In-Ga-Zn-O," *ECS Journal of Solid State Science and Technology*, vol. 2, no. 1, pp. P5–P8, 2012.

[183] K. Xiao, D. Lee, and J. J. Vlassak, "Kinetics of solid-gas reactions characterized by scanning AC nano-calorimetry with application to Zr oxidation," *Applied Physics Letters*, vol. 105, no. 17, pp. 0–5, 2014.

[184] K. Xiao and J. J. Vlassak, "Nucleation behavior of melted Bi films at cooling rates from 101 to 104 K/s studied by combining scanning AC and DC nano-calorimetry techniques," *Thermochimica Acta*, vol. 603, pp. 29–38, 2015.

[185] G.-D. Sim, Y. S. Choi, D. Lee, K. H. Oh, and J. J. Vlassak, "High tensile strength of sputter-deposited ZrB2 ceramic thin films measured up to 1016 K," *Acta Materialia*, vol. 113, pp. 32–40, 2016.

[186] A. You, M. A. Y. Be, and I. In, "Transparent conducting Zr-doped thin films for organic light-emitting diodes," vol. 1050, no. December 2000, pp. 1998–2001, 2006.

[187] A. You, M. A. Y. Be, and I. In, "High-mobility transparent conductive Zr-doped," vol. 082104, no. April 2006, pp. 2004–2007, 2007.

[188] L. J. Gadder, "Ionic and electronic conductivities of homogeneous and heterogeneous materials in the system Zr02-In203," vol. 75, no. 94, 1995.

[189] D. Ginley, H. Hosono, and D. C. Paine, eds., *Handbook of transparent conductors.* 2011.

[190] P. S. Using, X.-r. Diffraction, N. Yamada, I. Yasui, I. Oxide, T. Films, J. W. Bae, S. D. Park, P. K. Song, Y. Shigesato, O. Bierwagen, and T. Conductive, "Donor Compensation and Carrier-Transport Mechanisms

in Tin-doped In 2 O 3 Films Studied by Means of Conversion Electron 119 Sn Mössbauer Spectroscopy and Hall Effect Measurements," 2000.

[191] T. Koida, M. Kondo, K. Tsutsumi, A. Sakaguchi, M. Suzuki, and H. Fujiwara, "Hydrogen-doped In2O3 transparent conducting oxide films prepared by solid-phase crystallization method," *Journal of Applied Physics*, vol. 107, no. 3, 2010.

[192] R. Carel and C. V. Thompson, "GRAIN GROWTH AND TEXTURE EVOLUTION by GRAIN GROWTH AND TEXTURE EVOLUTION," 1995.

[193] C. V. Thompson and R. Carel, "Stress and grain growth in thin films," *J. Mech. Phys. Solids*, vol. 44, no. 5, pp. 657–673, 1996.

[194] J. A. Venables, G. D. T. Spiller, and M. Hanbucken, "Nucleation and growth of thin films," *Reports on Progress in Physics*, vol. 47, p. 399, 1984.

[195] G. Street, "Statistical mechanics of nucleation : a review," vol. 218, no. April, pp. 883–899, 2004.

[196] M. Birkholz, B. Selle, W. Fuhs, S. Christiansen, H. P. Strunk, and R. Reich, "Amorphous-crystalline phase transition during the growth of thin films: The case of microcrystalline silicon," vol. 64, pp. 1–9, 2001.

[197] R. A. Van Santen, "The Ostwald step rule," *Journal of Physical Chemistry*, vol. 88, no. 24, pp. 5768–5769, 1984.

[198] M. Hu, S. Noda, and H. Komiyama, "Amorphous-to-crystalline transition during the early stages of thin film growth of Cr on SiO 2," pp. 1–37.

[199] J. Robertson, "Thermodynamic model of nucleation and growth of plasma deposited microcrystalline silicon," vol. 731, no. April 2002, 2013.

[200] H. M. Silicon, T. Arai, H. Shirai, K. Nomoto, Y. Urano, F. P.-e. Chemical, and V. Deposition, "Related content Role of Hydrogen Plasma during Growth of Hydrogenated Microcrystalline Silicon : In Situ UV- Visible and Infrared Ellipsometry Study," 1994.

[201] C. C. Tsai, G. B. Anderson, R. Thompson, and B. Wacker, "R1," vol. 114, pp. 151–153, 1989.

[202] W. Freude, I. Hochfrequenztechnik, U. Karlsruhe, and W. Germany, "-n + l)," vol. 2, no. 18, pp. 1986–1987, 1987.

[203] T. Koida, H. Fujiwara, and M. Kondo, "Hydrogen-doped In 2 O 3 as High-mobility Transparent Conductive Oxide," 2007.

[204] A. T. W. Kempen, F. Sommer, E. J. Mittemeijer, M. Planck, and D. Stuttgart, "Determination and interpretation of isothermal and non-isothermal transformation kinetics ; the effective activation energies in terms of nucleation and growth," vol. 7, pp. 1321–1332, 2002.

[205] M. Fundamentals, "Solid-State Kinetic Models : Basics and Mathematical Fundamentals," pp. 17315–17328, 2006.

[206] C. V. Thompson, "Grain growth in thin films," 1990.

[207] G. Britain, P. Press, and M. Science, "Simulation of thin film grain structures–i. grain growth stagnation," vol. 38, no. 8, pp. 1455–1462, 1990.

[208] M. Avrami, "Kinetics of Phase Change. I - General Theory," *The Journal of Chemical Physics*, vol. 7, no. 12, p. 1103, 1939.

[209] M. Kwoka, L. Ottaviano, M. Passacantando, S. Santucci, G. Czempik, and J. Szuber, "XPS study of the surface chemistry of L-CVD SnO2 thin films after oxidation," *Thin Solid Films*, vol. 490, no. 1, pp. 36–42, 2005.

[210] V. K. Jain, P. Kumar, M. Kumar, P. Jain, D. Bhandari, and Y. K. Vijay, "Study of post annealing influence on structural, chemical and electrical properties of ZTO thin films," *Journal of Alloys and Compounds*, vol. 509, no. 8, pp. 3541–3546, 2011.

[211] J. M. Themlin, M. Chtaïb, L. Henrard, P. Lambin, J. Darville, and J. M. Gilles, "Characterization of tin oxides by x-ray-photoemission spectroscopy," *Physical Review B*, vol. 46, no. 4, pp. 2460–2466, 1992.

[212] S. Stoll and A. Schweiger, "EasySpin , a comprehensive software package for spectral simulation and analysis in EPR," vol. 178, pp. 42–55, 2006.

Federica Landucci

Route d'Oron 6
Lausanne, 1010 CH
✉ *federica.landucci@gmail.com*
in *Federica Landucci*
+41 764229142

▬ Experience

01/2015 – Present

PHD STUDENT IN PHYSICS
EPFL, Swiss Federal Institute of Technology of Lausanne, (CH)
- Thesis work on the *Development of new oxide materials for solar energy applications using low-cost, highly abundant and highly stable elements.*
- Co-author of 2 scientific papers in high-impact peer-reviewed journals.
- Established and managed a scientific collaboration with Harvard University.
- Supervisor of one master student for a semester project - experiment strategic planning, operational guidelines and results control.
- Grant for the European Microscopy Conference (Lyon) workshop - 2016.

09/2003 – 12/2014

HEAD OF TECHNICAL DEPARTMENT AND BOARD MEMBER
Landucci s.r.l. - Healthcare equipment and services, (IT)
- Led 4 people team, managed maintenance program at client's sites by planning and coordinating employees schedule and tasks resulting in increased operational efficiency.
- Developed and implemented a new supplier/final client management system - decreased latency time for services delivery to customers.
- Built new partnerships with vendors, improving profits up to 15%.
- Renovated the company website, improved features for easier access to online purchases.

02/2010 – Present

TEACHING ASSISTANT
- Teaching assistant in General Physics and Electron Microscopy for bachelor, master and PhD courses - more than 1000 students followed and examined (**Swiss Federal Institute of Technology of Lausanne**).
- Teaching assistant in General Physics and Applied Physics for electronic, biomedical, electric, chemical engineering faculties and medicine faculty (**University of Cagliari**).

▬ Education

10/2009 – 11/2013

MSc – Master of Science in Physics, University of Cagliari, (IT)
- Final mark: 110 /110 (ECTS A).

09/2010 – 08/2011

Ecole Polytechnique, Paris (FR)
- Erasmus Student
- Stage at LPICM - Laboratoire de Physique des Interfaces et Couches Minces.

10/2003 – 09/2009

BSc – Bachelor of Science in Physics, University of Cagliari (IT)
- Final mark: 106 /110 (ECTS B).

▬ Technical skills

Material synthesis RF Magnetron Sputtering

Sample preparation Mechanical polishing (tripod method), low energy ion milling, focused ion beam (FIB).

Charact. techniques Transmission electron microscopy (TEM), in traditional and high resolution modes (HRTEM), Energy-dispersive spectroscopy (EDX), Scanning electron microscopy (SEM), *in situ* and *ex situ* X-ray diffraction (XRD), X-ray photo-emission spectroscopy (XPS), Differential scanning calorimetry (DSC) and Electron spin resonance (EPR).

IT Electron microscopy-associated software such as Digital Micrograph, TIA, Esprit, Velox, Inca and Aztec as well as the programming language Mathematica.

Personal

Voluntary
- Active member of GEI (Gruppo Esponenti Italiani). Promoter of the association to young generations in the Swiss society by organizing social events and conferences. Established new relationships with the Young Executive Members of the Italian Chamber of Commerce in Switzerland.
- Active member of BfG (Blue for Green), spin off association of *Ingénieurs du monde* active in promoting sustainable and long-term agriculture in Madagascar and construction of potable water wells. Writing reports for institutional investors and supervision of on-site activities.

Passion
I'm passionate about baroque and neo-classical sculpture, organic architecture and contemporary art. I visit exhibitions and museums every time I can. I love organizing summer boat trips in the Mediterranean with family and friends. I'm currently reading about artificial intelligence and deep learning.

Languages
English (full professional proficiency), French (full professional proficiency), Italian (mother tongue).